Fluid to Rock Interactions During Deposition, Diagenesis, and Anthropogenic Activities: Application of Stable Barium Isotopes in the Appalachian Basin

by

Rebecca Miriam Matecha

B.A. Geoscience, Smith College, 2018

Submitted to the Graduate Faculty of the

Dietrich School of Arts and Sciences in partial fulfillment

of the requirements for the degree of

Doctor of Philosophy

University of Pittsburgh

2023

UNIVERSITY OF PITTSBURGH

DIETRICH SCHOOL OF ARTS AND SCIENCES

This dissertation was presented

by

Rebecca Miriam Matecha

It was defended on

March 14, 2023

and approved by

Eitan Shelef, Assistant Professor, Department of Geology and Environmental Science

William Harbert, Professor, Department of Geology and Environmental Science

J. Alexandra Hakala, Senior Fellow for Geologic and Environmental Systems, National Energy Technology Laboratory, Department of Energy

Dissertation Co-Director: Rosemary Capo, Associate Professor, Department of Geology and Environmental Science

Dissertation Co-Director: Brian Stewart, Associate Professor, Department of Geology and Environmental Science

Fluid to Rock Interactions During Deposition, Diagenesis, and Anthropogenic Activities: Application of Stable Barium Isotopes in the Appalachian Basin

Rebecca Miriam Matecha, PhD

University of Pittsburgh, 2023

The study of the interactions between aqueous fluids and geologic materials (rock, sediment, and soil) in both natural and anthropogenic systems is critical to understanding surface processes, development of geologic resources, diagenesis and lithification, and for predicting the fate and transport of environmental contaminants. In this dissertation I integrate field, experimental and petrographic studies with the use of stable barium (Ba) isotopes as a tool to investigate fluid-rock interactions in the Appalachian Basin.

Part 1 details development of an optimized method for the separation of Ba from major and isotopically interfering elements in a variety of geologic and hydrologic materials. Part 2 presents static autoclave and flow-through experiments with synthetic fracturing fluid conducted on Marcellus Shale core samples which indicated minimal Ba release from fluid−shale interactions but was consistent with barite precipitation, driven in part by release of sulfate from the shale, accompanied by a small amount of exchangeable Ba mobilization from shale surfaces. The results also indicate that the high-Ba concentrations in unconventional Marcellus Shale-produced waters are not a result of interaction of injected fluids with shale and/or drilling mud barite during hydraulic fracturing. Instead, they may indicate intrusion of high-Ba, high-δ^{138}Ba formation waters entering the well via subsurface fractures. Finally, Part 3 is focused on a study of barite ($BaSO_4$) and carbonate nodule development in the Upper Devonian Hanover Shale. The δ^{138}Ba values in co-occurring barite and carbonate suggests downward movement of the sulfate methane transition zone after carbonate nodule precipitation and subsequent barite precipitation. Complex

micromorphologic relationships between barite and carbonate and the variability in $\delta^{138}Ba$ between nodule horizons, and between carbonate nodules and their barite rims, suggest asynchronous and possibly episodic introduction of isotopically distinct Ba during deposition of the Hanover Shale. The range of $\delta^{138}Ba$ values suggest that Marcellus Shale formation waters could have diffused upwards with methane and been the source of Ba that led to the precipitation of barite.

Table of Contents

Preface xiv

1.0 Introduction 1

2.0 A Single Column Separation Method for Barium Isotope Analysis of Geologic and Hydrologic Materials with Complex Matrices 6

2.1 Introduction 6

2.2 Experimental Methods 8

2.2.1 Materials and Reagents 8

2.2.2 Samples for Ba Separation Experiments 9

2.2.3 Sample Dissolution/Ba Concentration Methods 10

2.2.4 Barium Double Spike 12

2.2.5 Cation Column Separation Procedure 13

2.2.6 Analysis of Column Calibration Cuts 14

2.2.7 Ba Isotope Mass Spectrometry Method 15

2.3 Results and Discussion 16

2.3.1 Optimal Separation of Barium 16

2.3.2 Verification from Ba Isotope Analysis 20

2.4 Conclusions 22

3.0 Experimental Investigation of Barium Sources and Fluid-Rock Interactions in Unconventional Marcellus Shale Wells Using Ba Isotopes 23

3.1 Introduction 23

3.2 Methods and Experimental 27

3.2.1 Rocks and Mineral Samples 27

3.2.2 Reagents and Fluid Compositions 27

3.2.3 Flow-Through Experiments 28

3.2.4 Static Autoclave Experiments 30

3.2.5 Benchtop HCl Leaching Experiments 31

3.2.6 Determination of Shale Exchangeable Ba 32

3.2.7 Elemental Analysis 32

3.2.8 Ba Separation and Isotope Analysis 33

3.3 Results and Discussion 34

3.3.1 Frac Fluid Batch Reactions 34

3.3.2 Flow-Through Experiments 38

3.4 Conclusions 45

4.0 Barium Isotope Characterization of Hanover Shale Carbonate and Barite Nodules and Implications for Post-Depositional Fluid Flow in the Appalachian Basin 47

4.1 Introduction 47

4.2 Background 49

4.2.1 Geologic Setting 49

4.2.2 Conceptual Model for Nodule Formation 50

4.2.3 Application of Ba Isotopes 51

4.3 Methods 52

4.3.1 Rock and Mineral Samples 52

4.3.2 Petrography 54

4.3.3 Sample Preparation and Dissolution 55

4.3.4 Elemental Analysis 56

4.3.5 Ba Separation and Isotope Analysis 56

4.4 Results 58

4.4.1 Nodule Morphology 58

4.4.2 Petrographic Analysis 60

4.4.3 Barium Isotope Analysis 61

4.4.3.1 Carbonate Nodules 62

4.4.3.2 Barite Nodules 64

4.4.3.3 Barite Rim on Carbonate Nodules 64

4.5 Discussion 65

4.5.1 Changes in Ba Input Reflected in Barite Nodules 65

4.5.2 Relationship Between Barite and Carbonate Nodules 67

4.5.3 Fluid (Ba) Sources During Diagenesis: 68

4.6 Conclusions: 69

Appendix A: Supplemental Materials for Chapter 2 71

Bibliography 77

List of Tables

Table 1: Limits of Detection (LOD) for all Isotopes Monitored in this Work by SF-ICP-MS 14

Table 2: La/Ba and Ce/Ba Ranges for Various Geologic and Hydrologic Materials 20

Table 3: Interference Correction and δ^{138}Ba Values for Selected Standards 21

Table 4: Composition of Synthetic Fracturing Fluid for Static Autoclave Experiments..... 29

Table 5: Barium Concentration and Isotope Data for Flow-Through and Static Autoclave Experiments..... 35

Table 6: Barium Concentrations and Isotope Compositions for Benchtop Drilling Mud and Barite Leaching Experiments 37

Table 7: Barite and carbonate sampling heights and locations. (Bridge coordinates 42.537720, -79.168471)..... 54

Table 8: Barium isotope and concentration data for barite and carbonate nodules. Barium concentrations were not measured in the barite samples, but stoichiometric barite contains 588,420 µg/g Ba. 62

List of Figures

Figure 1: Barium isotope value ranges for natural fluids and solids as well as fluids and solids from the Marcellus Shale. 2

Figure 2: Bio-Rad Poly-Prep® Chromatography Columns Used in Ba Separation Experiments 9

Figure 3: Column Matrix Separation for Major Elements and Ba 17

Figure 4: Separation of Ba from Isobaric Interferents La and Ce During Elution of 2N HNO_3. 18

Figure 5: Schematic designs of (a) the flow through experimental setup (modified from Xiong et. al. (2021) Copyright 2021 American Chemical Society) and (b) the static autoclave experiment setup. 30

Figure 6: Results of four closed-system static autoclave experiment. 36

Figure 7: Plots of flow-through results. 39

Figure 8: Comparison of molar Ba and sulfate of flow-through influent and effluent samples. 40

Figure 9: SEM images of post experiment barite pracipitated on (a) milled and (b) proppant cores. 42

Figure 10: Barium isotope variation of flow-through influent and effluent samples. 43

Figure 11: Plots of flow-through effluents with model result overlays. 44

Figure 12: (a) Mid to Upper Devonian Units of the Western NY Appalachian Basin after Lash (2015). The Hanover Shale overlies the Pipe Creek Shale and together they make up the Upper Devonian Java Formation. The Hanover Shale lies approximately 260

m above the Marcellus Shale. (Diagram is not to scale) (b) Map of the extent of Devonian shales in PA and NY. The Hanover Shale outcrop located in Silver Creek, NY is marked in red. 49

Figure 13: Conceptual model of fluid flow during diagenesis of the Hanover Shale. Modified from Lash (2015). 51

Figure 14: Walnut Creek outcrop of the Hanover Shale. 53

Figure 15: Barite sample morphologies. 59

Figure 16: Barite nodule photomicrographs. 60

Figure 17: Carbonate nodule photomicrographs 61

Figure 18: δ^{138}Ba (‰) values for carbonate and barite compared to height of the sampling horizon within the outcrop on the left. 63

Figure 19: Comparison of δ^{138}Ba (‰) values of carbonate nodules with Ba concentrations (in µg Ba per g of carbonate). 63

Figure 20: Comparison of δ^{138}Ba (‰) values for the center and rim of a barite nodule from the 50 cm barite nodule horizon. 64

Figure 21: Comparison of carbonate nodules and barite rim on carbonate nodules δ^{138}Ba (‰). Outcrop stratigraphy is shown on the left. Dashed green line shows overlap of barite rim uncertainty. 65

Figure 22: Diagram of the cross section view of the precipitation of the barite rim on carbonate nodules in shallow sediments at the SMTZ. 68

Figure 23: δ138Ba (‰) values for carbonate and barite compared to height of the sampling horizon within the outcrop on the left. δ138Ba (‰) ranges for seawater and Marcellus waters is shown above the plot. 69

Appendix Figure 1: Examples of column matrix separation for major elements, Ba, and isobaric interferents La and Ce for a volcanic silicate sample using the BIO-RAD Poly-Prep® gravity flow ion exchange columns described in the manuscript. 73

Appendix Figure 2: Examples of column matrix separation of Ba from isobaric interferents La and Ce for a produced water sample (a) and calcium carbonate sample (b) using the BIO-RAD Poly-Prep® gravity flow ion exchange columns described in the manuscript. 76

List of Appendix Tables

Appendix Table 1: Thermo Element® ICP-MS signal intensity (in counts per second) for a column calibration using 2.0 N HCl for the entire elution of a dissolved silicate volcanic rock. 71

Appendix Table 2: Thermo Element® ICP-MS signal intensity (in counts per second) for a column calibration using 2.5 N HCl for the entire elution of a dissolved silicate volcanic rock. 72

Appendix Table 3: Thermo Element® ICP-MS signal intensities (in counts per second) for a column calibration using 2.5 N HCl for the first 20 mL, and 3.0 N HNO_3 for the remaining elution of a produced water sample with 0.5 µg of La and Ce added. 74

Appendix Table 4: Thermo Element® ICP-MS signal intensities (in counts per second) for a column calibration using 2.5 N HCl for the first 20 mL, and 2.0 N HNO_3 for the remaining elution of dissolved freshwater mussel shell calcium carbonate. 75

Preface

Thank you Rosemary Capo and Brian Stewart for being amazing advisors and for your guidance and support throughout my PhD. Thank you committee members Ale Hakala, Bill Harbert, and Eitan Shelef for your support throughout my PhD. Thank you Kyle Whittinghill for your mentorship in teaching pedagogy. Thank you to my fellow graduate students, friends, and family for your support. Finally, thank you Tim (Phoc Vong) for always keeping me fed.

1.0 Introduction

The understanding of interactions between aqueous fluids and geologic solids (rock, sediment, and soil) in both natural and anthropogenic systems is widely applicable to topics such as weathering, energy resources, environmental geochemistry, and soil science [Ganor et al., 2009; Banner & Hanson, 1990]. Water-rock interactions in sedimentary systems typically involve the co-occurrence and interaction of dissolution, precipitation, leaching, and cation exchange reactions [Martini, 2002]. In the ocean, sediments interact with downward diffusing seawater and upward diffusing fluids from deeper sediments to precipitate minerals and sometimes nodules [Mullins et al., 1980; Griffith & Paytan, 2012]. In energy resource drilling, fluids leach exchangeable elements and deposit mineral scales [Ganor et al., 2009; Matecha et al., 2022; Renock et al., 2016; Phan et al., 2018].

The alkaline earth element barium (Ba, atomic no. 56) can play an important role in many of these systems and processes. There are two common mineral forms of Ba, barite ($BaSO_4$) which forms rapidly when Ba is exposed to sulfate, and witherite ($BaCO_3$). In the ocean Ba is used as a proxy for global biogeochemical cycling and in ocean sediments upward diffusing Ba rich fluids from underlying sediments can contribute to the precipitation of barite nodules [Bates et al., 2017; Hsieh & Henderson, 2017; Clark, 1987]. Barium is of particular interest in oil and gas production as produced waters and formation fluids can be unusually high in Ba (up to 10^4 ppm), which can lead to issues with waste disposal and reuse of produced waters in hydraulic fracturing [Rassenfoss, 2011]. Additionally, the high Ba concentrations can cause the precipitation of barite mineral scale in the wellbore and in fractures which limits well productivity and decreases wellbore integrity [Vetter, O. J. 1976; Jew et. al. 2017].

Recently, the application of stable Ba isotope analysis has become an important tool for understanding complex processes such as Ba cycling in the ocean, water to rock interactions in the subsurface, and preservation methods for various minerals [Bates et. al, 2017; Horner et. al., 2015; Cao et. al., 2016; Matecha et. al., 2022]. Barium has six stable isotopes, with ^{138}Ba being the most common at ~71% abundance, and can undergo mass dependent fractionation as a result of diffusion, ion exchange, and mineral precipitation. During the precipitation of barite from a fluid the lighter Ba isotopes are preferentially incorporated into the solid leading to isotopically heavier fluids [Von Allmen et. al., 2010; Bottcher et. al., 2012; Miyazaki et. al, 2014; Nan et al., 2015].

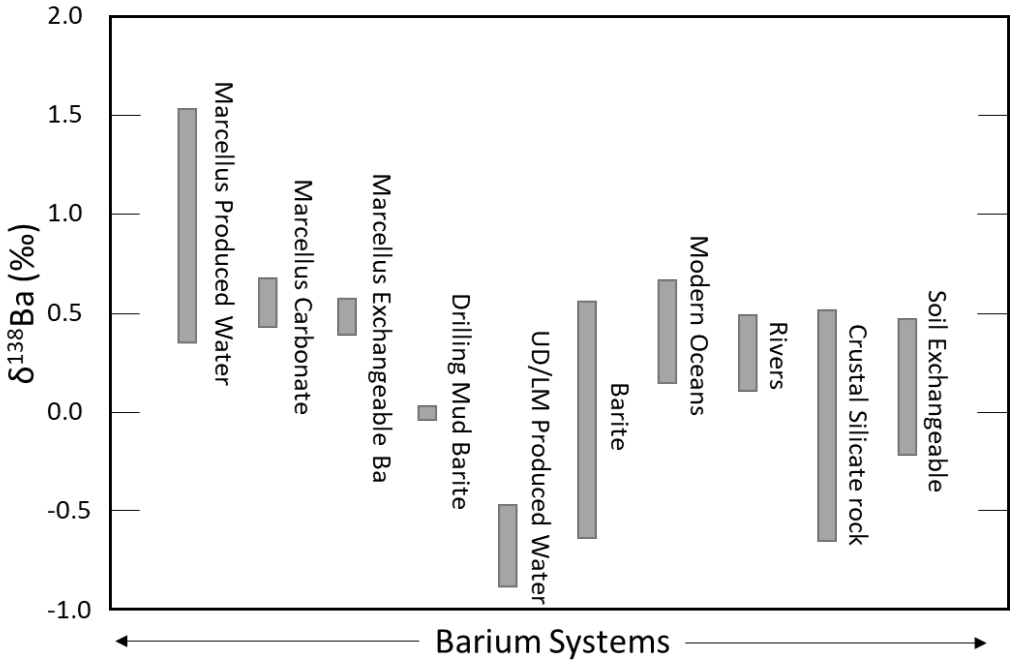

Figure 1: Barium isotope value ranges for natural fluids and solids as well as fluids and solids from the Marcellus Shale. UD/LM = Upper Devonian / Lower Mississippian. (Modified from Tieman et al., 2020)

Isotope fractionation of Ba leads to distinct Ba isotopic signatures which can be used to determine relationships between samples and as tracers (Figure 1) [Tieman et al., 2020]. Ocean and river water typically have values of +0.1 to +0.6 ‰, crustal silicate rocks range from -0.7 to+0.5 ‰, and soil exchangeable Ba falls in the middle ranging from -0.2 to +0.45 ‰. Marcellus

produced waters are some of the isotopically heaviest fluids measured to date, ranging from +0.4 to +1.5 ‰. In comparison, Upper Devonian to Lower Mississippian produced waters are isotopically very light, ranging from -0.8 to -0.5 ‰. This highlights the variability and potential use of barium isotopes as a tracer.

In the work reported in this dissertation, Ba isotope ratios were measured using a multi-collector inductively-coupled plasma mass spectrometer (MC-ICP-MS). I report these values using the notation δ^{138}Ba (‰), the permil difference between the $^{138}Ba/^{134}Ba$ ratio of the sample from the normalizing standard NIST 3104a:

$$\delta^{138}Ba = 10^3 \left[\frac{\left(^{138}Ba/^{134}Ba\right)_{sample}}{\left(^{138}Ba/^{134}Ba\right)_{standard}} - 1 \right]$$

Typical uncertainties of these measurements are ±0.05‰, and they are reported in the data tables of each chapter.

In Chapter 2 of this dissertation (published in Geochemical Transactions; Matecha et. al., 2021) I present an optimized method for the separation of Ba from major and isotopically interfering elements in a variety of geologic and hydrologic materials. The technique uses readily available materials and one single-use disposable column per sample, making this a rapid and effective method for the preparation of samples for Ba isotope analysis. In this method sample aliquots containing ~2µg Ba are spiked with a $^{135}Ba/^{137}Ba$ double spike and loaded into cation exchange columns filled with cation exchange resin. Major elements are removed through elution with 2.5 N HCl followed by collection of Ba through elution with 2.0 N HNO_3 while the interfering elements La and Ce remain in the columns. This method is applied in the studies presented in Chapter 3 and Chapter 4 of this dissertation. In addition to optimizing the Ba separation method, a method for the concentration of Ba in low-Ba seawater and dissolution of barite were optimized

through application of cation exchange using Na_2CO_3 to form witherite ($BaCO_3$), followed by dissolution of witherite in HCl to recover Ba.

Marcellus Shale produced waters have unusually high Ba concentrations, ranging up to 14,000 mg/L [Barbot et. al. 2013; Chapman et. al. 2012; Haluszczak et. al. 2013]. In Chapter 3 (published in Energy & Fuels; Matecha et. al., 2022) I present a series of experiments intended to simulate various stages of the hydraulic fracturing process in unconventional Marcellus Shale gas wells to constrain the source of Ba in Marcellus produced waters and to identify the controlling factors involved in barite precipitation and dissolution within these systems. Rather than Ba concentrations increasing with interaction of fluids with shale and/or drilling mud, Ba concentrations decreased due to barite precipitation. This is consistent with leaching of sulfate from the solids. Modeling of the flow-through experiments showed that shale exchangeable Ba was extracted in the first few days and influenced the $\delta^{138}Ba$ of the fluid but was depleted quickly, after which the $\delta^{138}Ba$ of the fluid reflected isotope fractionation from barite precipitation. Interaction of drilling mud with hydrochloric acid (HCl) led to less than 0.01% dissolution and $\delta^{138}Ba$ inconsistent with Marcellus produced waters. This all suggests that the source of Ba in the Marcellus Shale is not due to interaction of fluid and shale/drilling mud, but may be originating from in-situ formation fluids.

Formation and preservation of marine barite is complex, and while potential sources of Ba introduced into the sulfate methane transition zone (SMTZ) in shallow sediments and processes leading to subsequent barite precipitation have been proposed, barium isotope characterization and comparison with potential source fluids has not yet been explored. To address this, in Chapter 4 I present barium isotope, morphological, and petrographic analysis of barite and carbonate nodules from the Appalachian Basin Upper Devonian Hanover Shale exposed in upstate New York. The

δ^{138}Ba compositions of carbonate nodules, barite nodules, and barite rim on carbonate nodules falls within the range of δ^{138}Ba values for Marcellus formation fluids, which suggest that they are a possible source of Ba to the Hanover Shale during nodule formation. Variability in δ^{138}Ba between different horizons of both barite and carbonate, and between carbonate nodules and their barite rims, suggest that the introduction of Ba to the Hanover Shale was not a single event, but instead discrete events. This is further supported by the transition within barite nodules from small (100-500 μm diameter) euhedral barite crystals in the center to larger radial barite crystals on the rim.

Together this research works to improve the methods for Ba isotope analysis and the understanding of fluid-rock interactions during anthropogenic activities and during the deposition and diagenesis of sedimentary units.

2.0 A Single Column Separation Method for Barium Isotope Analysis of Geologic and Hydrologic Materials with Complex Matrices

2.1 Introduction

Barium (Ba) is a critical element of interest in studies of oceanic biogeochemical cycling and the diagenetic alteration of sediments [e.g., Church & Wolgemuth, 1972; Bacon & Edmond, 1972; Chan et al., 1976; Griffith & Paytan, 2012; Carter, Paytan, & Griffith, 2020], and the isotopic composition of Ba has been used to understand element cycling in marine, riverine, lacustrine and pedogenic environments [von Allmen et al., 2010; Horner et al.; Bullen & Chadwick, 2016; Cao et al., 2016; Bates et al., 2017; Hsieh & Henderson, 2017; Bridgestock et al., 2018; Hendry et al., 2018; Crockford et al., 2019; Gou et al., 2020; Gong et al., 2020]. More recently, Ba concentrations [Renock et al., 2016; Paukert Vankeuren et al., 2017; Jew et al., 2018] and its isotope signatures [Tieman et al., 2020] have been studied as indicators of Ba sources and mobility related to subsurface water-rock interactions and the fate and transport of contaminants in drilling mud, solid waste and produced waters related to hydraulic fracturing of oil and gas wells.

In order to obtain the Ba isotope composition of a sample via thermal ionization mass spectrometry (TIMS) or multi-collector inductively coupled plasma mass spectrometry (MC-ICPMS), the Ba must be separated from other elements in the sample. High levels of matrix elements will interfere with the ionization and transmission of Ba, and elements with directly overlapping isotopic masses (isobaric interferences, including Xe, La, and Ce) change the measured Ba isotope ratios unless they are removed prior to and/or corrected for during isotope ratio measurement [Andreasen et al., 2007; Barling & Weis, 2008; Nan et al., 2015; van Zuillen et

al., 2016; Zeng et al., 2019; Lin et al., 2020; Yu et al., 2020]. While Xe is only introduced during MC-ICPMS measurement from the atmosphere and Ar gas source, all other interferents (matrix major elements, La, and Ce) must be removed via chemical processing prior to analysis by TIMS or MC-ICPMS. For samples with high ratios of Ba to matrix and/or isobaric interferents (e.g., high-Ba formation waters or samples of barite, $BaSO_4$), the chemical separation of Ba is relatively straightforward [von Allmen et al., 2010; Crockford et al., 2019; Tieman et al., 2020; van Zuillen et al., 2016; Tian et al., 2019; Tian et al., 2020]. However, silicate rock samples can have high rare earth element (REE) to Ba ratios, necessitating robust procedures for removing La and Ce prior to analysis.

Various methods for the separation of Ba for isotopic analysis have been reported in detail. Miyazaki et al. (2014) described an elution method using 2.5 N hydrochloric acid (HCl) to separate matrix major elements followed by 1.5 N nitric acid (HNO_3) to enhance separation of Ba from REE in silicate rock samples. However, two major isotopes of Ba (^{136}Ba and ^{138}Ba) were excluded from the MC-ICPMS measurement protocol due to interferences from ^{138}La, ^{136}Ce, and ^{138}Ce [30]. Nan et al. (2015) used a similar elution method (3.0 N HCl followed by 4.0 N HNO_3), using two successive columns to fully remove interferents. Elution curves for La and Ce were not reported in this study. For separation of Ba from a range of silicate and carbonate rock types, Nan et al. (2018) and Zeng et al. (2019) reported using up to three column passes to fully separate Ba from the REE. Tian et al. (2019) described a method for separation of Ba from barite using 3 N HCl and 3 N HNO_3. Because barite consists of ~59% Ba by weight, matrix and isobaric interferences are negligible, and the Ba could be purified in a single step.

This paper describes sample preparation and ion exchange chromatography separation of Ba using a two-reagent elution in a single off-the-shelf column that is suitable for the isotopic

analysis of Ba in samples with complex matrices and a range of REE/Ba ratios that are encountered in geologic and environmental samples. In addition to barite and seawater, we demonstrate that the method is applicable to low-Ba silicates and carbonate rocks, river water, and high total dissolved solid (TDS) fluids containing organic compounds, such as oil and gas produced waters and other brines. The method uses readily available polypropylene disposable columns and cation exchange resin. We document that this method successfully separates Ba from matrix major elements, as well as La and Ce, in one step, thus necessitating minor to negligible correction for these isobaric interferences during measurement by MC-ICPMS.

2.2 Experimental Methods

2.2.1 Materials and Reagents

Experimental work was conducted at the University of Pittsburgh under clean lab conditions. Ultrapure 18.2 MΩ Milli-Q water (MQW) was used for acid dilutions and for washing solids. Teflon beakers and other sample vessels were acid washed, and most sensitive procedures (e.g., sample dissolution, spiking, evaporation, and column separations) were carried out in ULPA-filtered laminar flow hoods. Cation exchange resin (Bio-Rad AG® 50W-X8 200-400 mesh) was pre-cleaned with repeated, sequential applications of MQW, 2% HNO_3, and 6N HCl, which were added to the resin in a fluorinated ethylene propylene (FEP) bottle, shaken vigorously, and decanted after settling. Ultrapure (Fisher Optima™) HCl, HNO_3, hydrofluoric acid (HF) and hydrogen peroxide (H_2O_2) were used for sample dissolution and preparation, resin/column preparation, elution and organic matter removal. Ultrapure (J.T. Baker™ Ultrex™) sodium

carbonate (Na_2CO_3) was used for barite dissolution and seawater Ba precipitation. The Na_2CO_3 solution was further purified to remove Ba by using a modification of the method described by Foster et al. (2004); in this method, 1.15 M Na_2CO_3 solution is reacted with a 1.1 N calcium chloride solution ($CaCl_2$; Thermo Fisher Alfa Aesar™ 99.99% purity), which precipitates Ba along with calcium carbonate, and results in an approximately 1 M Na_2CO_3 solution with low Ba levels.

To prevent sample carryover, we used disposable polypropylene gravity flow ion exchange columns (Bio-Rad Poly-Prep® Chromatography Columns) and disposed of the column and the resin after each use. The columns have a 2 mL bed volume with a 10 mL reservoir and a porous 30 µm polyethylene bed support frit (Figure 2).

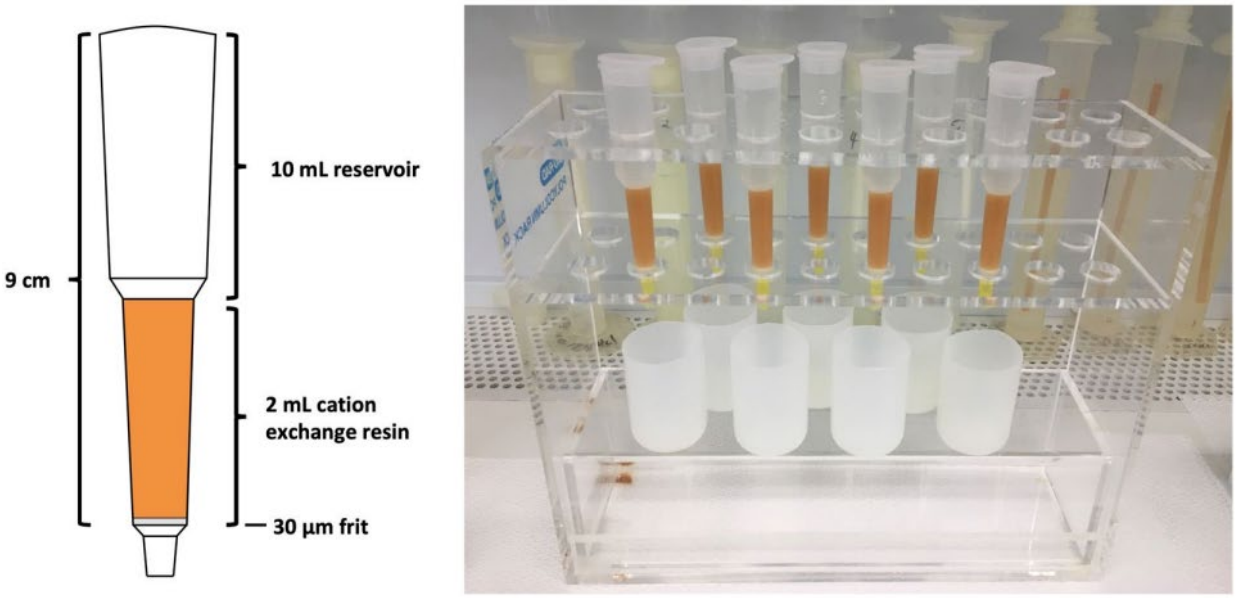

Figure 2: Bio-Rad Poly-Prep® Chromatography Columns Used in Ba Separation Experiments

2.2.2 Samples for Ba Separation Experiments

Verification of method applicability was conducted using natural materials and standards which reflect a range of matrices encountered in geologic and environmental samples. Silicate

rocks (shale, sandstones, igneous rocks) can be problematic for Ba isotopic analysis because of potentially high levels of REE interferents relative to Ba. Carbonate minerals such as limestone and marine shells have high Mg and Ca content, and some freshwater aragonite shells can have high REE relative to Ba [Merschel & Bau, 2015]. Oil and gas produced waters have high TDS, can contain hydrocarbons and other organic compounds, and can vary greatly in Ba content (0.25 to >10,000 ppm [Barbot et al., 2013; Ouyang et al., 2017]). For the experiments reported here, fluid samples included seawater (National Research Council Canada seawater reference material NASS-6 collected off the coast of Nova Scotia, Canada), surface water from the Ohio River in Pennsylvania, USA (OR-1204-1a), and produced waters from the Marcellus Formation in Greene County, Pennsylvania (M4TFA0518; also used as an internal lab Ba isotope standard). The carbonate sample (PA-LO-102714) was a freshwater mussel shell collected in western Pennsylvania. Silicate rock samples include volcanics from southern Alaska [Cole & Stewart, 2009], an organic-rich black shale (Marcellus Shale), and USGS standards BCR-2 basalt and AGV-1 andesite [Raczek et al., 2001]. Selected data for these samples are provided in Appendix Table 1.

2.2.3 Sample Dissolution/Ba Concentration Methods

The carbonate mussel shell was powdered and dissolved in 2.5 N HCl. The silicate rock samples were dissolved under clean lab conditions using HF and HNO_3 in a microwave digestion system (Milestone Ethos®). Following digestion at 200°C, the samples were treated with aqua regia and concentrated HNO_3 to remove fluorides.

Barite was dissolved following a method based on earlier work [Crockford et al., 2019; Tian et al., 2019; Breit et al., 1985; Horner et al., 2017]. In brief, powdered barite was reacted with

1 M purified Na_2CO_3 solution (1 mL/10 mg barite) at 95°C in a sealed Savillex® vial, leading to exchange of SO_4^{2-} with CO_3^{2-}. After centrifuging, the supernatant was discarded, and the reaction was repeated twice on the remaining residue for a total of 72 h, resulting in a precipitate of barium carbonate ($BaCO_3$). The precipitate was rinsed with MQW, evaporated to dryness, and the carbonate dissolved in 3N HNO_3. The sample was dried down, redissolved, and diluted to 2% HNO_3 for elemental analysis.

Because Ba is present at low concentrations (30-175 nM) in seawater [Church & Wolgemuth, 1972; Bacon & Edmond, 1972; Chan et al., 1976; Horner et al., 2015; Cao et al., 2016; Bates et al., 2017; Hsieh & Henderson, 2017], it must be concentrated prior to column separation in order to reduce the matrix load. Barium was extracted from seawater (NASS-6) using a method modified from Foster et al. (2004) and others [Horner et al., 2015; Bates et al., 2017; Hsieh & Henderson, 2017; Bridgestock et al., 2018]. An aliquot of seawater containing ~2 µg Ba (~200 mL) was spiked with a ^{137}Ba-^{135}Ba solution (see next section) so that isotope mass fractionation associated with all subsequent processing could be corrected for during measurement. The aliquot was reacted with sufficient 1 M Na_2CO_3 solution (purified to remove Ba) to result in precipitation of calcium carbonate, which scavenges Ba from solution. This occurs at a molar ratio of CO_3^{2-} to Ca^{2+} of approximately 6:1. Once saturation was reached, the reaction occurred nearly instantaneously, and the crystal-fluid mixture was then stirred for 5 minutes to ensure full removal of Ba. The sample was then decanted into 50 mL centrifuge tubes, rinsing any residue into the tubes using MQW, and centrifuged at 4000 rpm for 5 min. The supernatant was removed by pipette, preserving the precipitate (with most of the Ba) in the centrifuge tube. The precipitate was transferred to a Savillex vial using MQW and a vortex mixer as needed and evaporated to near dryness at 90°C. The carbonate precipitate was then dissolved in 4 N HCl,

evaporated to dryness, and redissolved in 0.5 mL 2.5 N HCl for cation column separation. This method can also be used for separation of Ba from other high TDS fluids and brines with a low Ba concentration and sufficient Ca for precipitation.

2.2.4 Barium Double Spike

A calibrated double Ba isotope spike was added to dissolved samples prior to loading of the columns and was used to correct for mass fractionation during MC-ICPMS analysis. Previous work [von Allmen et al., 2010; Horner et al., 2015; Bullen & Chadwick, 2016; Cao et al., 2016; Nan et al., 2015; van Zuillen et al., 2016; Miyazaki et al., 2014; Bottcher et al., 2012; Mavromatis et al., 2016; Pretet et al., 2016; van Zuillen, Muller et al., 2016] has shown that this can correct for mass fractionation during chemical processing, thus obviating the need for full (>99%) recovery of Ba from the column. In addition, use of a double spike reduces the effects of non-isobaric matrix interferents [van Zuillen et al., 2016]. Based on error analysis using the double spike tool of Rudge et al. (2009), the ^{137}Ba-^{135}Ba isotope pair was chosen because it optimizes the precise determination of ^{138}Ba/^{134}Ba, whether obtained by direct measurement or calculated based on the measured fractionation in the ^{138}Ba/^{136}Ba ratio. The double spike was made using ^{135}Ba- and ^{137}Ba-enriched carbonate salts from the National Isotope Development Center at Oak Ridge National Laboratory and calibrated by running mixtures of double spike and NIST 3104a. Further details of spike calibration can be found in the Supporting Information of Tieman et al. (2020).

2.2.5 Cation Column Separation Procedure

For some samples with very low REE/Ba (carbonate shell PA-LO-102714 and produced water M4TFA0518), a mixed REE standard was added prior to column experiments in order to test the separation of Ba more rigorously from the isobaric interferents La and Ce. In all of the experiments reported here, approximately 3 mL of cleaned AG50W 200-400 mesh cation resin suspended in MQW was incrementally added by pipette to the acid cleaned columns until the resin bed was just above the base of the 10 mL column reservoir. The resin bed was acidified with 3 ml of HCl at the normality used for that elution experiment, and the resin adjusted to ensure no air bubbles were left and that the top of the resin bed was aligned with the base of the column reservoir. The resin-filled columns were then cleaned with 5 mL of 6.0 N HCl and equilibrated with 4.5 ml of HCl at the appropriate elution normality, added incrementally.

Prior to loading in the columns, residual organics were removed from the sample by adding 1 mL of 50% H_2O_2 drop wise, followed by evaporation to dryness. The sample was then redissolved in 0.5 mL of HCl at the appropriate elution normality, allowed to equilibrate for a minimum of 2 h, and placed in an ultrasonic bath for 30 min to ensure that it was dissolved to the fullest extent possible. Samples were centrifuged in 2 mL polypropylene centrifuge tubes at 4000 rpm for 10 min to prevent any insoluble precipitates from being loaded onto the cation exchange resin bed. The supernatant was added to the prepared column using a pipette with a 1 mL polypropylene tip. The sample matrix (excluding Ba and the REE) was eluted by adding HCl of the appropriate normality in successive increments, and the eluent was collected for elemental analysis. This was followed by the addition of either HCl or HNO_3, depending on the experiment, and these samples (containing primarily Ba and the REE) were collected for elemental analysis.

2.2.6 Analysis of Column Calibration Cuts

Elemental chemistry of column calibration cuts was determined on a Thermo Element XR® sector field (SF) ICP-MS at the at the National Energy Technology Laboratory (NETL). The SF-ICP-MS sample introduction system used a Glass Expansion Ezylok Micromist nebulizer and Twister spray chamber. The SF-ICP-MS gas flow rates and mass spectrometer voltages were optimized daily in low resolution mode to obtain the maximum signal intensity while minimizing doubly charged and oxide species. Barium, Sr, and REE were analyzed using the low resolution slit ($\Delta m/m = 300$), while second row non-metals and Fe were analyzed using the medium resolution slit ($\Delta m/m = 4000$).

All samples were spiked with 10 µg/L indium as an internal standard prior to analysis to account for matrix differences. Samples which contained high TDS were minimally diluted with 2% HNO_3 prior to analysis to minimize matrix effects affecting the ionization in the plasma. While quantitation was not required to generate the elution curves, limits of detection (LOD) were calculated for all analytes as 3 times the standard deviation of the blank from three consecutive blank runs. These detection limits are listed in Table 1. Data from these experiments are reported in Appendix Table 2, Appendix Table 3, and Appendix Table 4.

Table 1: Limits of Detection (LOD) for all Isotopes Monitored in this Work by SF-ICP-MS

Medium Resolution		**Low Resolution**	
Isotope	**LOD, µg/L**	**Isotope**	**LOD, µg/L**
^{23}Na	0.487	^{88}Sr	0.0004
^{24}Mg	0.341	^{137}Ba	0.0069
^{44}Ca	0.434	^{139}La	0.0001
^{56}Fe	0.0086	^{140}Ce	0.0002

2.2.7 Ba Isotope Mass Spectrometry Method

A subset of samples was analyzed for Ba isotopic composition on a Thermo Neptune Plus® MC-ICPMS at the University of Pittsburgh, part of a joint NETL-University of Pittsburgh facility. For these samples, the separated Ba cut was evaporated to dryness at 90°C, dissolved in 1 mL of concentrated HNO_3, and sonicated for 10 min before again being evaporated to dryness. The sample was redissolved in 2% HNO_3 (2 mL per µg of Ba), sonicated in the sealed container for 60 min, and transferred to an acid cleaned 15 mL centrifuge tube for MC-ICPMS analysis.

We report the isotope ratio of Ba as δ^{138}Ba, which is the permil deviation of the $^{138}Ba/^{134}Ba$ ratio of a sample from that of NIST Standard Reference Material 3104a:

$$\delta^{138}Ba = 10^3 \left[\frac{\left(^{138}Ba/^{134}Ba\right)_{sample}}{\left(^{138}Ba/^{134}Ba\right)_{3104a}} - 1 \right]$$

Samples were introduced into the MC-ICPMS using an ESI Apex® desolvating nebulizer. Barium isotopes (^{134}Ba, ^{135}Ba, ^{136}Ba, ^{137}Ba, ^{138}Ba) were measured simultaneously on five Faraday cups using 10^{11} Ω resistors. Isobaric interferences from Xe, La and Ce were monitored by measurement of ^{131}Xe, ^{139}La and ^{140}Ce on three additional Faraday cups. Xenon, which is present in the atmosphere and have variable concentrations in the argon gas used in MC-ICP-MS analysis, has interfering masses at 134 and 136 (10.44% and 8.87% of total Xe). Cerium is an isobaric interferent of Ba at mass 136 (^{136}Ce = 0.185% of total Ce), and both Ce and La are isobaric interferents at mass 138 (^{138}Ce = 0.251% of total Ce and ^{138}La = 0.09% of total La). Typical ^{138}Ba intensities were 30-40 V for the Apex® desolvating nebulizer (~200 V/ppm Ba). No apparent systematic variation in δ^{138}Ba was observed within this range of signal intensity. Mass fractionation of the sample was corrected for by iterative normalization to the $^{137}Ba/^{135}Ba$ of the double spike using an exponential law [Wasserburg et al., 1981]. The detector configuration and

additional details of the mass spectrometric methods can be found in Supporting Information in Tieman et al. (2020).

2.3 Results and Discussion

2.3.1 Optimal Separation of Barium

Combinations of different normalities of HCl (1.5-2.5 N) and HNO_3 (1-3 N) were tested to optimize the purity of the Ba cut while minimizing the volume and concentration of reagent necessary to elute. Results of selected experiments are reported in Appendix Table 2, Appendix Table 3, Appendix Table 4, Appendix Figure 1, and Appendix Figure 2. Use of 2.5 N HCl up to the beginning of Ba elution resulted in the optimal separation of major matrix elements from Ba (Figure 3). Experiments in which only HCl was used for elution (including of Ba) resulted in either overly large volumes of acid being required to fully capture the Ba (e.g., 2.0 N HCl; Appendix Figure 1a) or significant overlap of Ba with the isobaric interferents La and Ce (e.g., 2.5 N HCl; Appendix Figure 1b). van Zuilen et al. (2016) report using 2.0 N or 6.4 N HCl to elute Ba, but do not report elution curves for La or Ce. The absence of these peaks during the TIMS measurement [van Zuillen et al., 2016] may reflect the lower ionization efficiency of these elements relative to Ba rather than separation from the Ba cut. Previous work demonstrated that a better separation of Ba from the REE could be achieved by eluting with HNO_3 [Nan et al., 2015; Tian et al., 2019; Miyazaki et al., 2014]; therefore, we tested different normalities of HNO_3 for optimal elution of Ba while minimizing overlap of La and Ce. Use of higher normality acid results in a tighter Ba

elution peak but greater overlap of REE with Ba (Appendix Figure 2). The optimal concentration of HNO_3 to elute Ba from the columns used in these experiments was 2.0 N (Figure 3).

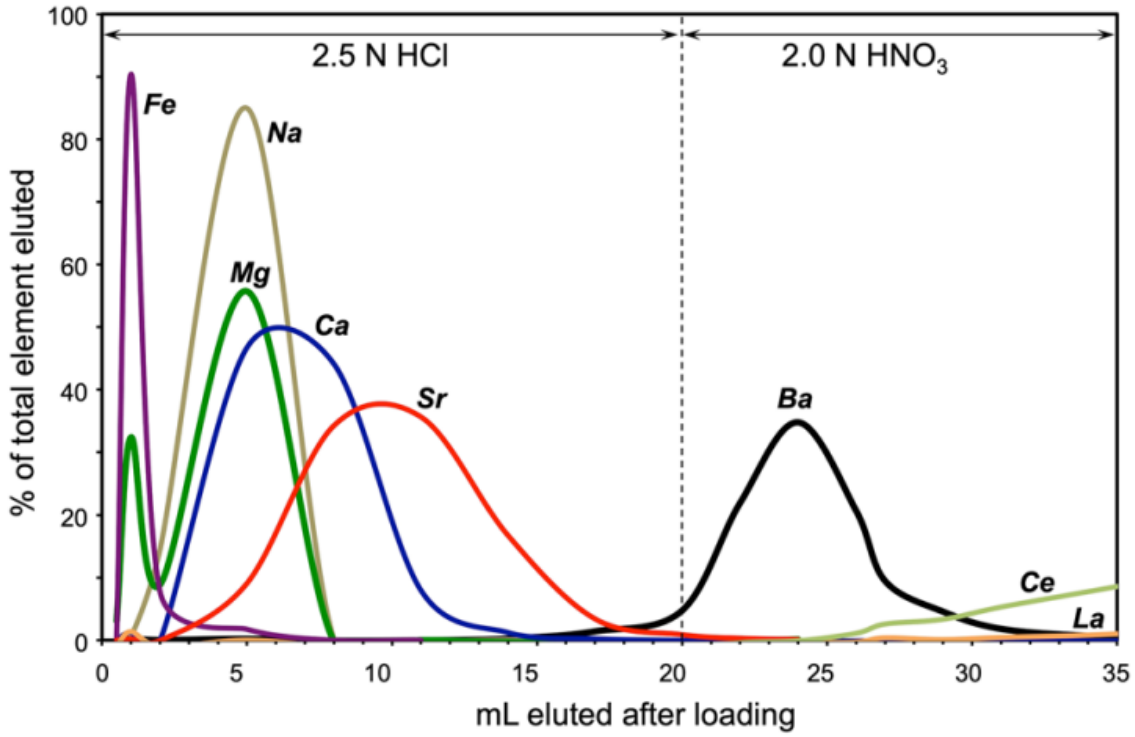

Figure 3: Column Matrix Separation for Major Elements and Ba. Sample was 60 mg $CaCO_3$ (freshwater mussel shell). Cerium and La were not fully recovered even after 60 mL, so their % elution values are likely overestimated.

The separation of Ba from REE isobaric interferents was further tested by analyzing Ba elution curves in detail using a dissolved volcanic rock with La/Ba of ~0.015 and Ce/Ba of ~0.033, and a Marcellus Shale produced water sample in which La and Ce were added to increase La/Ba and Ce/Ba to ~0.67 (Figure 4). Based solely on the measured signal intensities (reported in counts per second) by SF-ICP-MS and the abundance of the measured isotope, the overlap of La with the Ba cut is 0.007% for the volcanic sample and 0.1% for the La-enriched produced water sample. Similarly, the overlap of Ce with the Ba cut is 0.03% and 1.1% for the volcanic sample and Ce-enriched produced water, respectively. In the latter case, such an overlap in Ce would necessitate a correction of ~0.3‰ to the δ^{138}Ba (for the measurement method described here), which can be

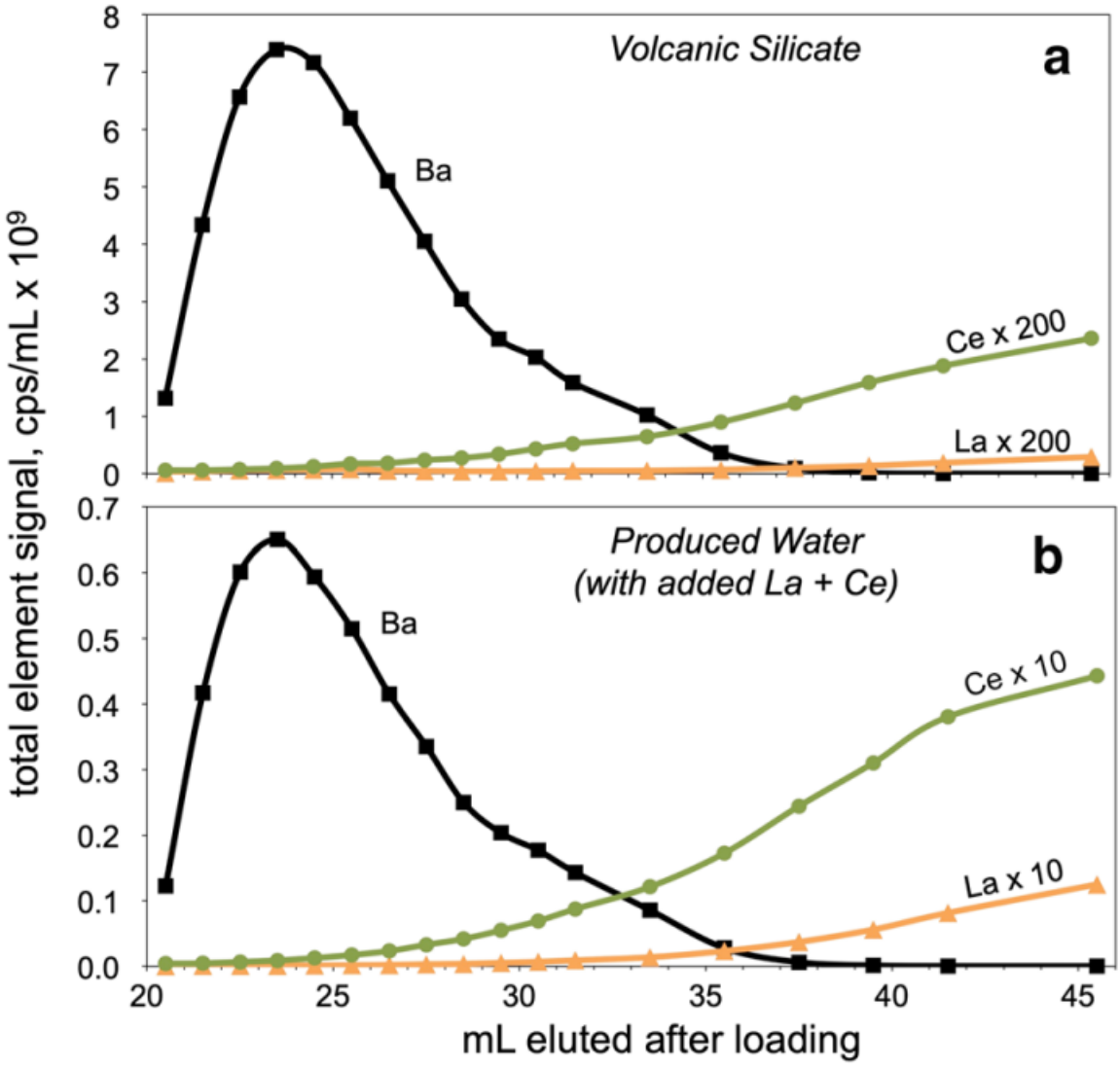

Figure 4: Separation of Ba from Isobaric Interferents La and Ce During Elution of 2N HNO_3. The y-axis is the signal intensity (in counts per second by SF-ICP-MS) per mL of each column cut, recalculate to reflect the total element signal rather than just the measured isotope. The La and Ce signals are multiplied by the factors shown on the curves; if plotted as their actual intensities, the curves would be barely distinguishable above baseline. The La/Ba and Ce/Ba of the volcanic silicate sample (a) prior to loading was ~0.014 and ~0.033, respectively, while La and Ce were added to the produced water sample (b) prior to loading to generate high La/Ba and Ce/Ba ratios of ~0.67.

done accurately. However, most geologic materials have Ce/Ba ratios (Table 2) considerably lower than the artificially Ce-enriched produced water reported here (Ce/Ba ≈ 0.25). Unusual natural

samples with very high Ce/Ba could be run through the same column twice to remove any excess Ce.

In the optimal separation procedure, a total of 20 mL 2.5 N HCl is used to elute the major matrix elements. Barium is eluted using 12 mL of 2.0 N HNO_3 (Figure 3). Major elements were effectively removed prior to the Ba cut; the results were similar for all samples tested (silicate, barite, and fluid samples). The REE isobaric interferents (La and Ce) only begin to elute from the columns after collection of the Ba cut. Additional Ce and La was added to the dissolved aliquot of carbonate (PA-LO-102714) prior to loading in the column to verify separation of Ba from these mass interferents (Figure 3). Because HNO_3 so effectively delays release of La and Ce, these elements were not fully removed from the columns even after adding 40 mL of 2 N HNO3 (following 20 mL of 2.5 N HCl). For all samples, including biogenic carbonate, silicate volcanic rock, organic-rich shales, and high TDS oil and gas produced brine, use of the method resulted in the release of major elements (e.g., Ca, Na, K, Al) from the sample matrix during the HCl elution. Barium was eluted during the nitric acid step, and La and Ce were effectively held on the resin until the bulk of the Ba was eluted. Using gravity flow, the total time from sample loading to removal of the Ba cut is 3-4 h. With a 24-sample column holder, processing 48 samples/day is easily achievable by a single user. The rate-limiting step is preparing the samples for column work (dissolution, evaporation, precipitation of Ba when needed).

The maximum procedural blank for Ba, determined by the limits of detection by SF-ICP-MS, was 2 ng of Ba, leading to a maximum δ^{138}Ba uncertainty of ±0.002‰ for a 2µg sample. This assumes the maximum isotopic difference between the sample and blank of 2‰, equivalent to the entire range of δ^{138}Ba values measured to date [Tieman et al., 2020]. This is well within the in-run uncertainty of ±0.03‰ or better for the MC-ICPMS analysis.

Table 2: La/Ba and Ce/Ba Ranges for Various Geologic and Hydrologic Materials

Material	La/Ba	Ce/Ba	References
Upper Continental Crust	0.056	0.12	McLennan, 2021
Lower Continental Crust	0.071	0.15	McLennan, 2021
Ocean Ridge Basalts	0.3-53	0.045-10	Gale et al., 2013
Peridotite	0.019-0.48	0.0033-2.0	Niu, 2004
Shale	0.023-0.071	0.11-0.15	McLennan, 2001 & Gromet et al., 1984
Marine carbonate	0.00037-0.077	0.00029-0.2	Li et al., 2019 & Geyman et al., 2019
Barite	0.000012-0.00055	0.00006-0.00053	Guichard et al., 1979
Seawater (average)	0.00037	0.000046	Nozaki, 1997
River water (global average)	0.0052	0.011	Gaillardet et al., 2005

2.3.2 Verification from Ba Isotope Analysis

Barium isotope analysis of separated samples further demonstrates effective separation. Two silicate rock standards (BCR-2 basalt and AGV-1 andesite) and an internal produced water standard (M4TFA0518) were analyzed after separations using both our previous method [Tieman et al., 2020] and the new method described here. With the previous method (smaller Teflon columns eluted with 2.0 N HCl, with silicates put through a second time to remove REE interferents), we obtained good agreement of the measured δ^{138}Ba with published standard values for silicates [Tieman et al., 2020]. The results of the current analyses are shown in Table 3. Because the isobaric interferences from ^{136}Ce, ^{138}Ce, and ^{138}La are monitored continuously during the run using ^{139}La and ^{140}Ce, we can calculate the total correction to the δ^{138}Ba from these interferents. As shown in Table 3, the maximum correction required for Ce is 0.002‰, which is an order of

Table 3: Interference Correction and δ^{138}Ba Values for Selected Standards

Standard	Unseparated Sample[a]		Post-separation[b]		‰ correction from[c]		δ^{138}Ba
	La_T/Ba_T	Ce_T/Ba_T	La_T/Ba_T	Ce_T/Ba_T	La	Ce	
BCR-2	0.037	0.078	0.000013	0.00011	-0.00002	0.00211	0.080±0.029
			0.000013	0.00011	-0.00002	0.00209	0.071±0.026
AGV-1	0.032	0.056	0.000011	0.000048	-0.00001	0.00090	0.067±0.030
M4TFA0518[d]	n/a	n/a	0.000018	0.000034	-0.00002	0.00064	0.948±0.034
			0.000018	0.000034	-0.00002	0.00064	0.936±0.037
			0.000018	0.000035	-0.00002	0.00066	0.902±0.033
SRM 3104a	n/a	n/a	0.000005	0.0000016	-0.00001	0.00003	

n/a no data available

[a]Ratio of total La or Ce to Ba in unseparated sample based on values reported by Raczek et. al (2001)

[b]Ratio of total La or Ce to Ba in separated Ba cut based on MC-ICPMS measure intensity of ^{138}Ba, ^{139}La, and ^{140}Ce

[c]Total correction applied to δ^{138}Ba value (‰) from measured ^{139}La and ^{140}Ce during analysis

[d]Internal lab standard – Marcellus Shale gas well produced water

magnitude smaller than the typical in-run uncertainty. The correction required for La is three orders of magnitude smaller than the typical in-run uncertainty. The ratio of total La to total Ba transmitted into the MC-ICPMS after column separation was ~3×10^{-4} of the pre-column ratio, while the Ce/Ba ratio after column separation was 9-14 $\times 10^{-4}$ of the pre-column value. Given that the interfering isotopes only make up 0.09% and 0.49% of the interferent masses measured at ^{139}La and ^{140}Ce, respectively, this amounts to a negligible or reliably correctable signal.

The δ^{138}Ba value of USGS standard BCR-2 (Table 3) that was processed using the methods described in this paper agree well with values reported previously by Nan et al. (2015, 2018), An et al. (2020) and Tieman et al. (2020). The AGV-1 δ^{138}Ba value obtained here agrees with values reported by Nan et al. (2015, 2018), van Zuilen et al. (2016), An et al. (2020), and Tieman et al. (2020).

2.4 Conclusions

We describe a method of Ba separation by cation exchange using readily available, disposable columns suitable for varied sample matrices, including silicates, carbonates, seawater, sulfates, brines, and produced waters. Eluting with 2.5 N HCl ensures the removal of major elements while Ba is still in the column, and the subsequent elution with 2.0 N HNO_3 separates Ba effectively from REE mass interferents. We show that matrix and isobaric interferents can be removed from most sample types in a single step, with no need for an additional cleanup column. In addition, the use of disposable columns prevents possible cross contamination when dealing with complex sample matrices. The moderate column size and elution volumes allow for rapid (3-4 hours) simultaneous separation of multiple samples.

3.0 Experimental Investigation of Barium Sources and Fluid-Rock Interactions in Unconventional Marcellus Shale Wells Using Ba Isotopes

3.1 Introduction

Barium (Ba) is an alkaline earth metal present at levels of ~600 ppm in the earth's upper continental crust [Rudnick & Gao., 2003]. It occurs as a minor or trace element substituting for K^+ in K-feldspars and micas, and, to a lesser extent, for Ca^{2+} in plagioclase feldspar, amphibole, pyroxene, apatite, and calcium carbonate [Johnson et al., 2017]. Barium also occurs as the primary cation constituent of the minerals barite ($BaSO_4$) and witherite ($BaCO_3$). Due to its low solubility constant, Ba readily precipitates as barite in the presence of sulfur; therefore, it has relatively low concentrations in seawater (3-21 μg/L) [Griffith & Paytan, 2012; Bacon & Edmond, 1972]. In contrast, Ba concentrations can be unusually high in some oil and gas produced waters (water that is pumped out of a well along with hydrocarbons during the production stage). Marcellus Shale unconventional produced waters from hydraulically fractured wells have average Ba concentrations of about 2,200 mg/L [Blondes et al., 2018; Bern et al., 2021; Barbot et al., 2013] with some being as high as 14,000 mg/L [Barbot et al., 2013; Chapman et al., 2012; Haluszczak et al., 2013]; in contrast, the Utica/Point Pleasant Shale and conventional Appalachian oil/gas wells average ~1,000 mg/L [Tasker et al., 2020]. Barium isotopes for the Marcellus Shale are isotopically heavy, with δ^{138}Ba ranging from +0.4 to +1.5‰ [Tieman et al., 2020].

One effect of the elevated Ba concentrations during unconventional hydrocarbon production (hydrocarbon trapped in low permeability rock accessed through hydraulic fracturing) is the precipitation of barite scale in the well-bore. This reduces the permeability of the source rock

by crystallizing in fractures and on the well-bore surface and reduces well productivity [Vetter et al., 1976; Wang et al., 1999; Jew et al., 2017]. Another issue is that produced water with elevated Ba concentrations requires additional treatment before it can be disposed of or reused in future hydraulic fracturing [Rassenfoss, 2011]. High Ba concentrations in produced waters can also pose an environmental and health hazard in the event of spills [Vidic et al., 2013; Kravenchenko et al., 2014; Soeder et al., 2014]. Furthermore, disposal of drill cuttings can pose a hazard if Ba and other contaminants are leached into surface water and soils [Stuckman et al., 2019; Chen & Carter, 2017; Xiong et al., 2020; Stewart et al., 2015; Phan et al., 2015].

Barium present as dissolved species in fluids from hydraulically fractured oil and gas wells (e.g., flowback, produced water) can have multiple sources [Chan et al., 2017; Xiong et al., 2020]. Barite, with a specific gravity of 4.5, is added to drilling mud to increase its density, which helps control formation pressure and prevent blowouts. After drilling, an acidizing stage is implemented during which ~2 M hydrochloric acid (HCl) is added to the well to clear fractures and pore spaces [Ferrer & Thurman, 2015]. This acidizing stage has the potential to cause dissolution of drilling mud barite and to leach and dissolve Ba-containing shale minerals [Jew et al., 2019; Renock et al., 2016]. Jew et al. (2019) suggested that a major source of Ba in the formation of barite scale is dissolution of drilling mud. However, Tieman et al. (2020) found that the Ba isotopic composition of Marcellus produced waters was not consistent with Ba solely sourced from drilling mud.

The interaction of hydraulic fracturing fluid with host shale also has the potential to mobilize exchangeable Ba, sulfates, and other chemical constituents [Phan et al., 2015; Harrison et al., 2017; Li et al., 2020].While Ba within the Marcellus Shale is primarily partitioned into the lattices of clay minerals [Phan et al., 2015; Renock et al., 2016], a significant portion could be held in even trace amounts of barite [Bern et al., 2021; Renock et al., 2016; Landis et al., 2018].

Sequential extraction experiments have shown that a relatively high fraction of Ba (up to 75%) is held on shale exchangeable sites (organic matter and surfaces of clay minerals such as illite and smectite) [Phan et al., 2015; Renock et al., 2016]. Upon interaction with high ionic strength fluids such as recycled produced water used for hydraulic fracturing, exchangeable Ba can be mobilized through exchange reactions with Ca and Na. Stewart et al (2015) showed that Ba could be easily extracted from shale mineral surfaces, but that this process could not explain the bulk of the dissolved solids in Marcellus-produced water. Renock et al. (2016) suggested that the combination of exchangeable Ba and shale barite dissolution from low-sulfate injection waters could explain the high Ba in Marcellus-produced waters. Xiong et al. (2020) showed that sulfate has a large impact on the precipitation of barite, and that the reuse of produced water combined with sulfate-bearing surface waters (e.g., Monongahela River water) as hydraulic fracturing fluid (HFF) can result in increased barite precipitation and therefore removal of Ba from the HFF. Another possible source of Ba is *in situ* formation fluids or fluids from adjacent rock units, which can enter the well during and after hydraulic fracturing [Barbot et al., 2013; Tieman et al., 2020; Stewart et al., 2015; Rowen et al., 2015].

To understand the reactions that occur between shale and HFF during the shut-in period of hydraulic fracturing, Paukert Vankeuren et al. (2017) conducted flow-through experiments, where HFF of different compositions was pumped through Marcellus Shale cores that were fractured or channeled. The experiments took place over seven days and occurred at downhole temperature and pressure (the conditions at depth within a well during the shut-in period). The HFF containing reused produced water showed greater barite precipitation within the shale core and a subsequent decrease in fracture volume, while HFF with HCl showed an increase in fracture volume associated with carbonate dissolution.

Modeling of the transport and reaction of Ba within unconventional wells by Li et al. (2020) indicates that the location of barite precipitation is affected and controlled by the pH of HFF and pore fluids. The oxidation and dissolution of pyrite in the shale result in the release of sulfate into the fluid. The addition of HFF and the acidizing stage also increases the dissolution of carbonate and other minerals, as well as affects exchange reactions that can introduced additional Ba into the solution. Together these processes facilitate the precipitation of barite.

Knowing what processes control and affect the release of Ba and the precipitation of barite is key to understanding the interactions of fluids and shale rock under downhole conditions. Moreover, the primary source of Ba in Marcellus produced waters is still not fully understood. To address these unknowns, Ba needs to be tracked through the system from the beginning of drilling to the pumping out of produced water, and experimental studies should incorporate downhole conditions to properly replicate the interactions. This paper presents a series of static and dynamic experiments meant to recreate downhole unconventional well conditions, and combines the tracking of major element concentrations with Ba isotope signatures to: (1) assess the role of the acidizing stage in releasing Ba from drilling mud, (2) quantify and model the interaction of brine with host rock at downhole conditions, (3) model how barite precipitation and shale-exchangeable dissolution control Ba concentrations and Ba isotope values, and (4) constrain potential sources of Ba in Marcellus Shale-produced waters.

3.2 Methods and Experimental

3.2.1 Rocks and Mineral Samples

Marcellus Shale samples used for exchangeable extraction and static autoclave experiments were taken from core collected at the Marcellus Shale Energy and Environment Laboratory (MSEEL) well MIP3H, from gas production depths of 2279.3-2279.6 m. Samples included pieces from either side of the 3.8 cm diameter core used for the flow-through experiments (see below). A sample of the drilling mud used during the drilling of this well was also used for static autoclave and benchtop dissolution experiments. An additional crystalline barite specimen (Wards Barite 349-0505 from Huanzala, Peru; hereafter, referred to as Peru Barite) was subsampled for benchtop dissolution experiments.

3.2.2 Reagents and Fluid Compositions

After drilling, HCl is typically injected (i.e., the acidizing stage) to clean out perforations within the well casing [Soeder et al., 2014; PADEP, 2010]. Benchtop dissolution experiments using ultrapure 2 M HCl, the concentration of acid commonly used for this step [Jew et al., 2018], were carried out to determine the effectiveness of the acidizing stage in dissolving barite from residual drilling mud and from within the shale.

In the flow-through and static autoclave experiments (discussed in detail below), a simulated hydraulic fracturing fluid (HFF) was created and used. The flow-through experiments used a simulated HFF with a composition similar to those used in industry composed of hydraulic fracturing additives [PADEP, 2010, FracFocus] and water from the Monongahela River near

Morgantown, West Virginia (Table 4). Elemental data for the Monongahela River water used in these experiments can be found in Xiong et al. (2021). For the static autoclave experiments, a low-Ba simulated HFF was created using the same hydraulic fracturing additives, except that ultrapure water (Milli-Q 18.2 MΩ) was used instead of Monongahela River water, and barium chloride dihydrate was not added (Table 4).

3.2.3 Flow-Through Experiments

To reproduce the reactions that occur during hydraulic fracturing, Marcellus Shale cores were used to conduct a set of flow-through experiments at the National Energy Technology Lab (NETL) in Morgantown, West Virginia. Two core samples from the MSEEL site collected at a depth of about 2280 m were selected for the experiments. Both cores measured 10.2 cm long and 3.8 cm in diameter, were cut in half laterally, and had two rows of three holes measuring 3 mm deep and 2 mm in diameter drilled into one half of each core (Figure 5a). The first core, referred to as the "milled core" had two grooves milled into the undrilled half, measuring 4 mm wide and 0.5 mm deep. The second core referred to as the "proppant core" had a quartz grain proppant added between the two core halves (see Xiong et al. (2021) for details).

Both cores used built-in heating wraps to maintain the core holder temperature at 66°C and were maintained at a confining pressure of 13.8 MPa using a syringe pump with deionized water as described in Xiong et al. (2021) (Figure 5). The simulated HFF made with Monongahela River water was filtered to 25 μm, purged with N_2 gas to limit O_2, and pumped from a reservoir into both cores simultaneously at a constant flow rate of 0.02 mL/min for a duration of 28 days. Samples were collected from the reservoir as well as from the milled and proppant core effluents throughout

the experiment. Aliquots of these samples were analyzed for elemental concentrations via ICP-MS and ICP-OES and for Ba isotopes using a MC-ICP-MS.

Table 4: Composition of Synthetic Fracturing Fluid for Static Autoclave Experiments

Chemical	Purpose	Weight %
HFF ingredients		
HCl (37%)	perforation inhibitor	0.25
WGA-15L	gelling agent	0.16
WCS-6ILC	clay stabilizer	0.106
WFR-6ILA	friction reducer	0.056
ammonium persulfate	breaker	0.02
glutaraldehyde	biocide	0.019
potassium hydroxide	pH adjuster	0.014
potassium carbonate	pH adjuster	0.014
revert flow	surfactant	0.0079
ethylene glycol	scale inhibitor	0.0045
citric acid	iron control	0.0036
boric acid	cross linker	0.002
ethanolamine	cross linker	0.0014
WAI-25ILC	corrosion inhibitor	0.0013
Synthetic produced water ingredients		
boric acid		0.002
potassium carbonate		0.024
potassium chloride		0.022
strontium chloride		0.14
ammonium chloride		0.016
sodium bromide		0.018
calcium chloride dihydrate		0.75
magnesium chloride		0.19
sodium chloride		1.68
sodium sulfate		0.00008
sodium bicarbonate		0.015

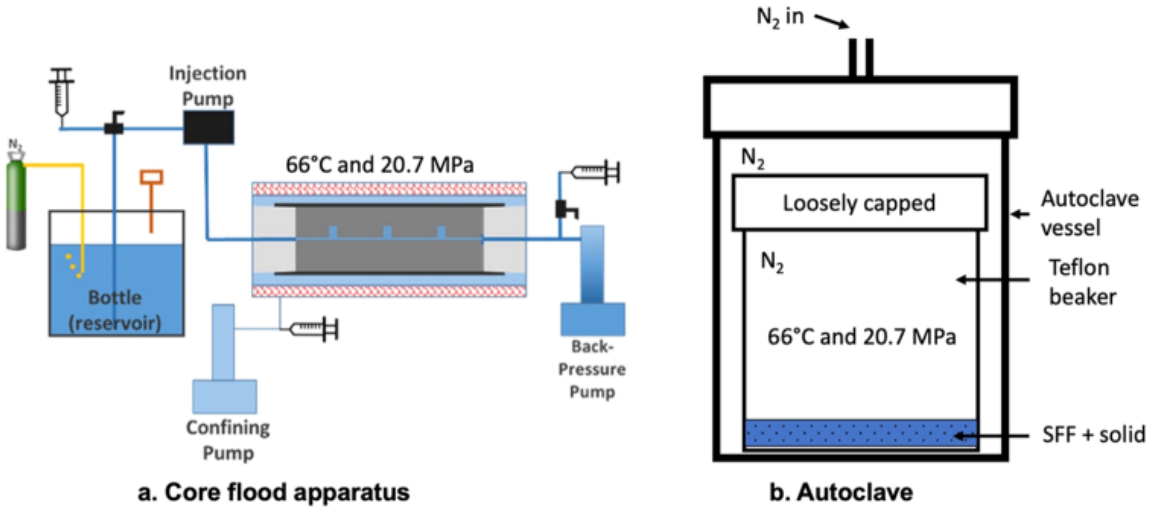

Figure 5: Schematic designs of (a) the flow through experimental setup (modified from Xiong et. al. (2021) Copyright 2021 American Chemical Society) and (b) the static autoclave experiment setup. Sketches are not to scale.

3.2.4 Static Autoclave Experiments

To better understand the downhole interaction between HFF and shale ± drilling mud, a set of static autoclave experiments were conducted at NETL. For these experiments, the low-Ba simulated fracturing fluid (using ultrapure water with no added Ba chloride dehydrate) was used to keep the Ba concentration low.

A composite shale sample was created by pulverizing Marcellus Shale core samples from MSEEL well MIP3H at depths of 2279.26, 2279.39, 2279.45, and 2279.60 m, and combining equal parts of each sample. A sample of pulverized drilling mud from well MIP3H was used as well. Three acid cleaned 340 mL Teflon vials were used: the first contained 200 mL of synthetic low-Ba HFF and 2 g of drilling mud; the second contained 200 mL of synthetic low-Ba HFF and 2 g of composite shale; and the third contained 200 mL of synthetic low-Ba HFF, 1 g of drilling mud,

and 1 g of composite shale. The Teflon vials with lids loosened to allow pressure equalization were placed into 500 mL Teflon beakers and then placed into the autoclave. Samples were brought to downhole temperature and pressure of 66°C and 13.8 MPa in a N_2 atmosphere over one hour and kept there for 6 hours before being brought back to room conditions over one hour (Figure 5b). Samples were decanted into acid cleaned centrifuge tubes and centrifuged at 4000 rpm for 10 minutes before being pipetted into pre-weighed 250 mL acid cleaned polypropylene bottles and moved to the University of Pittsburgh clean lab for chemical separation and isotope analysis.

3.2.5 Benchtop HCl Leaching Experiments

Drilling mud and a natural barite sample were used in benchtop dissolution experiments with 2 M HCl. Three aliquots of ~100 mg of drilling mud, and three aliquots of ~100 mg of barite were added to individual preweighed acid cleaned Teflon vials and weighed, and ~20 mL of ultrapure 2 M HCl was added to each. Caps were tightly attached, and the vials were placed on a stirring hot plate at ~75°C. One of each sample type (drilling mud and barite) was removed after 2, 6, and 48 hours.

As each sample was removed, it was allowed to fully cool before being transferred to acid-cleaned centrifuge tubes and centrifuged for 10 minutes at 4000 rpm. The solution was then pipetted into acid-washed polypropylene bottles and capped tightly. Aliquots of each sample were taken for analysis of Ba concentration and isotope composition.

3.2.6 Determination of Shale Exchangeable Ba

A set of shale core leaching experiments was carried out under benchtop conditions to characterize the concentration and isotope composition of possible contributions from exchangeable Ba. Four MSEEL Marcellus Shale samples from the same location and depth range as the flow-through and autoclave experiments were used. Samples were powdered and an aliquot of approximately 1 g of each was transferred to glass vials for weighing before being transferred to 50 mL polypropylene centrifuge tubes. Ammonium acetate (NH_4CH_3COO) buffered to pH 8 was used to displace exchangeable Ba^{2+}. Approximately 40 mL of 1 M ammonium acetate was added to each tube to reach a fluid:rock ratio of 40:1.

The leaches were agitated for ~4 hours in the Burrell Wrist Action Shaker, then centrifuged at 4000 rpm for 10 minutes. The solution was pipetted from the centrifuge tube, leaving behind the residue, and syringe-filtered through 0.45 μm PVDF filters into 60 mL high density polyethylene (HDPE) bottles. About 10 mL of 18.2 MΩ Milli-Q water (MQW) was added to the centrifuge tubes, and they were again centrifuged at 4000 rpm for 10 minutes. The solution was then pipetted from the centrifuge tube directly into the HDPE bottles containing the earlier solution. Samples were transferred to preweighed 25 mL Teflon vials and evaporated to dryness at 90°C. After being brought back to room temperature, the residues were dissolved in 6 mL of 2 M nitric acid (HNO_3) and then diluted to 2% HNO_3 for Ba concentration and isotope analysis.

3.2.7 Elemental Analysis

Aliquots from the flow-through and static autoclave experiments were analyzed for major and trace elements by ICP-OES and ICP-MS at the NETL Pittsburgh Analytical Laboratory.

Barium concentrations for the HCl dissolution experiments and exchangeable Ba measurements were determined simultaneously with the isotope composition by isotope dilution using a precisely calibrated double spike, which is described in Section 3.2.8.

3.2.8 Ba Separation and Isotope Analysis

To prepare samples for Ba isotope analysis, aliquots containing 2 µg Ba were transferred to 15 mL acid cleaned Teflon vials and spiked with a ^{137}Ba-^{135}Ba double spike to achieve a spike/sample ratio of ~0.7 [Tieman et al., 2020]. These spiked sample aliquots were evaporated to dryness at 90°C before being redissolved in 1 mL of concentrated HCl, evaporated to dryness, dissolved in 0.5 mL of 2.5 M HCl, and sonicated for 30 minutes. Samples were then eluted through cleaned cation exchange columns containing AG-50W, 200-400 mesh cation exchange resin and eluted using a combination of 2.5 M HCl and 2.0 M HNO_3, following the procedure of Matecha et al. (2021). The eluted Ba samples were collected in 15 mL acid cleaned Teflon vials and evaporated to dryness at 90°C. Samples were then dissolved in 1 mL of concentrated HNO_3 and sonicated for 10 minutes before being evaporated to dryness again. Finally, 7 mL of 2% HNO_3 was added to each sample, samples were sonicated for 60 minutes, and then transferred to an acid cleaned 15 mL centrifuge tube for MC-ICP-MS analysis.

Barium isotope ratios are reported here as δ^{138}Ba (‰), defined as:

$$\delta^{138}Ba = 10^3 \left[\frac{\left(^{138}Ba/^{134}Ba\right)_{sample}}{\left(^{138}Ba/^{134}Ba\right)_{standard}} - 1 \right]$$

where the normalizing standard is NIST 3104a Ba carbonate. Isotope ratios were measured on the DOE-NETL Thermo Neptune Plus® MC-ICP-MS at the University of Pittsburgh. Analyses were carried out with eight Faraday collectors in static mode, to measure the abundances of ^{134}Ba, ^{135}Ba,

^{136}Ba, ^{137}Ba and ^{138}Ba, and to measure and correct for isobaric interferences from ^{134}Xe, ^{136}Xe, ^{136}Ce, ^{138}Ce and 138La using reference masses ^{131}Xe, ^{139}La, and ^{140}Ce. Isobaric interference corrections were negligible for all samples. Each measurement comprised 50 cycles integrated for 4.2 s each, and the listed uncertainty is twice the standard error of the 50 cycles.

Mass fractionation from chemical separation and sample introduction into the MC-ICP-MS was corrected for by adding a calibrated ^{135}Ba-^{137}Ba double spike to the sample prior to column chemistry, and then iteratively achieving the calibrated value using the exponential law. Analyses of a solution of NIST 3104a Ba isotope standard spiked with the same ^{135}Ba-^{137}Ba mixture was interspersed with the unknown samples, and the corrected sample values were normalized to the average standard value to account for non-exponential effects, most likely related to plasma conditions. Refer to the supporting information in Tieman et al. (2020) for a complete discussion of analytical procedures and standard analyses.

3.3 Results and Discussion

3.3.1 Frac Fluid Batch Reactions

After reaction of the synthetic fracturing fluid with (1) drilling mud, (2) shale, and (3) a combination of the two, the Ba concentration of the fluid decreased (Table 5). Elemental analysis showed that sulfate increased as Ba decreased, suggesting that sulfate was introduced to the fluid and then reacted with Ba to precipitate barite. Sulfate was introduced in excess of Ba, leading to an increase in sulfate concentration in the fluid (Figure 6a). The fluid that was reacted with only shale showed the greatest increase in sulfate and the lowest Ba concentration, which implies that

oxidative dissolution of pyrite within the shale could be a primary source of sulfate and driver of barite precipitation [Bern et al., 2021; Xiong et al., 2021].

The decrease in Ba concentration across the suite of experiments was accompanied by an increase in δ^{138}Ba (Figure 6b), with the shale-reacted sample showing the greatest change. These

Table 5: Barium Concentration and Isotope Data for Flow-Through and Static Autoclave Experiments

Experiment	Days	δ^{138}Ba	Ba, mg/L	SO_4, mg/L
MSEEL Core Flood – Flow Through				
Influent				
Inf43629	0.08	0.32 ± 0.03	149	45.5
Inf 43630	1	0.32 ± 0.03	141	42.5
Inf 43633	4	0.29 ± 0.03	134	38.8
Inf 43637	8	0.28 ± 0.02	134	39.1
Inf 43647	18	0.35 ± 0.03	118	36.2
Inf 43657	28	0.39 ± 0.03	107	35.3
Effluent milled				
Eff-M 43630	1	0.58 ± 0.03	2.62	84.8
Eff-M 43633	4	0.81 ± 0.03	11.4	75.6
Eff-M 43637	8	1.17 ± 0.03	6.92	58.0
Eff-M 43642	13	1.26 ± 0.03	6.26	51.2
Eff-M 436647	18	1.25 ± 0.03	6.35	53.4
Eff-M 43654	25	1.27 ± 0.03	6.23	48.1
(duplicate run)	25	1.31 ± 0.04		
Eff-M 43657	28	1.22 ± 0.03	7.22	53.5
Effluent proppant				
Eff-P 43630	1	0.44 ± 0.04	2.36	102
(duplicate run)	1	0.45 ± 0.03		
Eff-P 43633	4	0.83 ± 0.02	5.11	83.7
Eff-P 43637	8	1.12 ± 0.03	6.82	67.4
Eff-P 43642	13	1.24 ± 0.02	6.30	56.8
Eff-P 43647	18	1.26 ± 0.03	6.37	55.1
Eff-P 43654	25	1.20 ± 0.03	6.42	52.3
(duplicate run)	25	1.27 ± 0.03		
Eff-P 43657	28	0.90 ± 0.03	8.01	46.4
Autoclave				
SFF[a] + shale		0.55 ± 0.03	1.22	27.3
SFF[a] + DM		0.19 ± 0.03	3.57	23.6
SFF[a] + DM + shale		0.21 ± 0.03	2.93	26.0
SFF[a]		0.06 ± 0.03	3.86	17.6

[a]Synthetic fracturing fluid.

results are consistent with closed-system Rayleigh isotope fractionation of Ba from barite precipitation using published fractionation factors [von Allmen et al., 2010; Hsieh & Henderson, 2017]. As barite precipitates, it preferentially incorporates the lighter Ba isotopes, leaving the remaining fluid enriched in heavy isotopes, thus increasing δ^{138}Ba. Regardless of which solid is

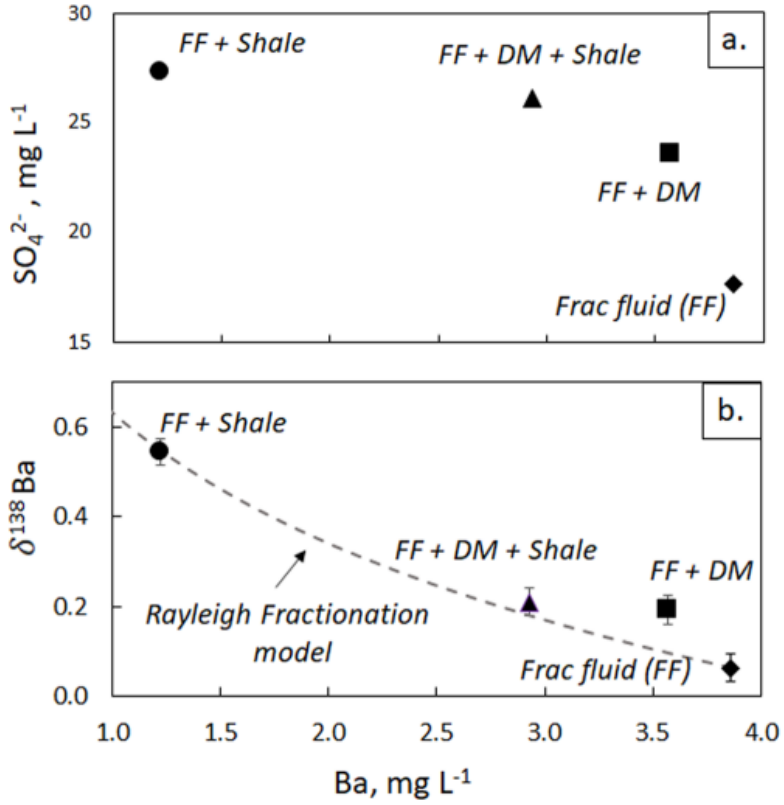

Figure 6: Results of four closed-system static autoclave experiment. FF is frac fluid and DM is drilling mud (containing barite). (a) Ba and sulfate concentrations were inversely correlated for all samples. (b) δ^{138}Ba was inversely correlated with Ba concentration and is consistent with Rayleigh fractionation (dashed line) using a fractionation facotr, α, of 1.0042.

interacting with the synthetic fracturing fluid (shale, drilling mud, or both), at downhole temperature and pressure conditions Ba is removed from the fluid. Elemental and isotopic data strongly suggest that this is due to barite precipitation; thus, barite in the shale or residual drilling mud is unlikely to be a major source of Ba to the fluid.

The benchtop barite dissolution experiments were run in parallel to the autoclave batch experiments. The addition of HCl dissolved <0.01% of the barite in drilling mud and in pure barite (Table 6), suggesting that under these conditions the acidizing stage is unlikely to dissolve enough barite to be the cause of the high Ba concentrations observed in produced waters. While the

Table 6: Barium Concentrations and Isotope Compositions for Benchtop Drilling Mud and Barite Leaching Experiments

Experiment	Hours	δ^{138}Ba	Ba, µg/g[a]
HCl leaches			
drilling mud 1	2	0.17 ± 0.02	13
drilling mud 2	6	0.22 ± 0.03	23
drilling mud 3	24	0.23 ± 0.02	10.5
barite 1	2	0.30 ± 0.04	9.5
barite 2	6	0.34 ± 0.03	20
barite 3	24	0.32 ± 0.04	9.0
MSEEL leachates			
shale MIP3H-7477.9		0.84 ± 0.04	0.474
shale MIP3H-7478.3		0.63 ± 0.03	0.582
shale MIP3H-7478.5		0.54 ± 0.03	0.481
shale MIP3H-7479		0.83 ± 0.03	0.385

[a]µg of Ba extracted per gram of the sample reacted.

isotopic composition of drilling muds may vary, Tieman et al. (2020) compared produced water and drilling mud from the same MSEEL well and showed that their δ^{138}Ba values were significantly offset from each other. Moreover, most marine and terrestrial barite samples measured to date [Crockford et al., 2019] have yielded δ^{138}Ba values well below those of Marcellus produced waters, which range from + 0.4 to +1.5‰. Data from these experiments indicate that there is minimal fractionation of Ba isotopes during dissolution (Table 6), indicating that dissolution of barite in the shale or drilling mud cannot reproduce the observed δ^{138}Ba values of Marcellus produced water.

These experiments suggest that shale is not a major source of Ba in produced waters and that the acidizing stage does not have a major impact on the dissolution of drilling mud barite.

Under the conditions of these experiments, the reaction of fracturing fluid with shale or drilling mud is more likely to remove Ba from the system than to add it. Most Marcellus shale-produced water has δ^{138}Ba values higher than any of the end members (shale or drilling mud) measured in this study and concentrations that are too high to achieve by barite precipitation.

3.3.2 Flow-Through Experiments

Elemental analysis of reservoir aliquots indicates that barium concentrations in the reservoir decrease over the course of the experiment. In addition, reservoir aliquots collected simultaneously for Ba isotopes, acidified to 0.25% HNO_3, stored in HDPE bottles, and analyzed 7-8 months later showed even more precipitous drops in Ba concentrations as well as a small amount of visible precipitate. We attribute this to barite precipitation in the reservoir and in the acidified aliquots.

To better determine the isotope composition of the reservoir at the time of the experiments, the influent isotope aliquots were treated to dissolve barite that precipitate subsequent to sampling, using the barite dissolution method described in Matecha et. al. (2021). The Ba concentrations and isotope compositions following this treatment are reported in Table 4, and they reflect the values at the time of the experiment. No changes in Ba concentrations were observed in the effluent samples from the time of collection to the time of Ba isotope analysis.

Barium concentrations dropped by an order of magnitude between the influent (input) and effluent (output) samples for both cores, indicating the removal of Ba via precipitation within the core (Table 5; Figure 7a). While the Ba concentrations for effluents decreased when compared to influent, there is a noticeable trend for both the milled and proppant core effluents in which Ba concentration increased over the first few days (Table 5), after which it remained relatively steady

for the duration of the experiment. An effluent sample collected from the milled core on the third day showed an anomalously high value of 11.4 mg/L. The final sample concentrations (day 27) were 7.2 mg/L for the milled core and 8.0 for the proppant core.

Unlike the Ba concentrations, the sulfate concentrations increased for all effluent samples in comparison to the influents, suggesting dissolution of shale core minerals such as pyrite and

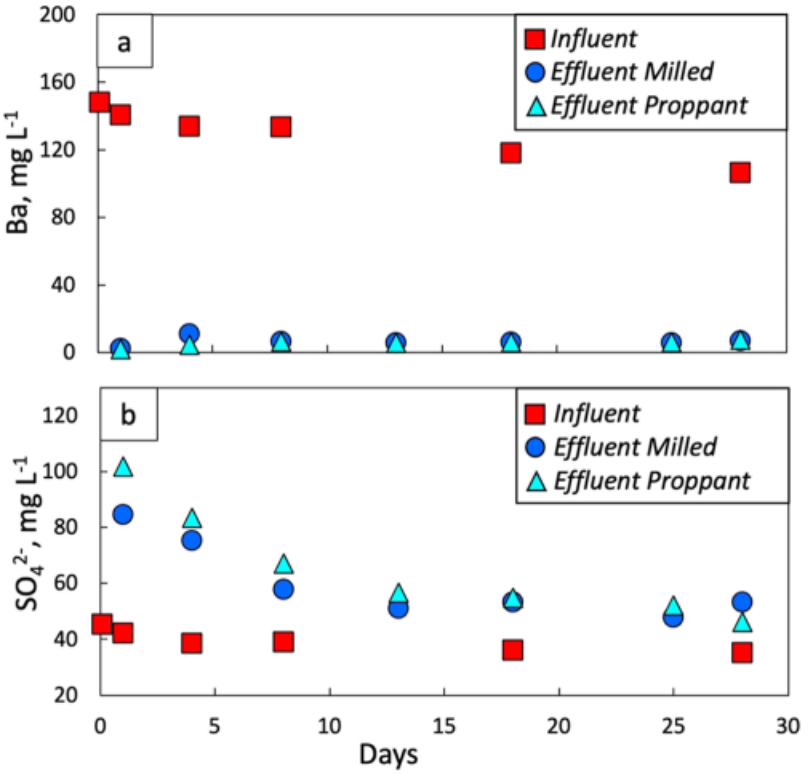

Figure 7: Plots of flow-through results. (a) Barium concentrations of the effluent samples were significantly lower than those of the influent. (b) Sulfate concentrations of the effluent were generally higher than those of the influent, suggesting the addition of sulfate from the shale.

subsequent release of sulfate (Figure 7b). Effluent sulfate concentrations start out about twice as high as the influents (80-100 mg/L), then decrease over the first 10-15 days before stabilizing at ~50 mg/L. At 27 days sulfate concentrations are still higher for the effluents than the influent

despite the influent sulfate concentration having remained relatively stable (from ~45 to ~35 mg/L) during the experiment.

The inverse correlation between Ba and sulfate in the effluent (Figure 8) suggests that sulfate contributed by the shale drove precipitation of barite. This is supported by the SEM observations of barite crystals on core surfaces after completion of the experiment (Figure 9). As sulfate concentrations are at least an order of magnitude greater than Ba concentrations, the overall

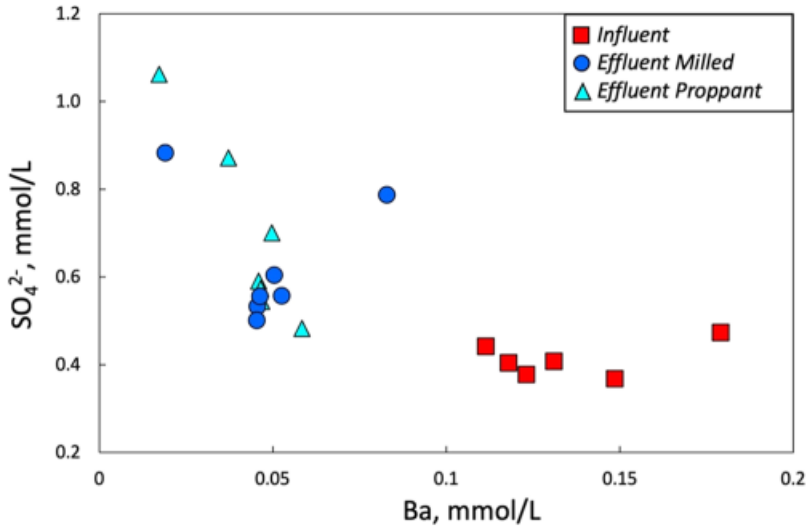

Figure 8: Comparison of molar Ba and sulfate of flow-through influent and effluent samples.

decrease in sulfate over time is not a result of barite precipitation, but of a decrease in the amount of reactive sulfur contributed by the core. Reactive surface area may be greater earlier in the experiment due to the presence of residual powders from milling, or due to exposed surfaces (including pyrite) becoming mantled over time as they react. As sulfate concentrations decrease with the depletion of pyrite throughout the experiment there is less barite precipitation and a higher Ba concentration in the effluents.

In both cores the Ba isotope ratios (δ^{138}Ba) follow the same trends through time. The δ^{138}Ba are higher for the effluents than for the influent in all samples (Figure 10). Over the first 12 days

the $\delta^{138}Ba$ of the milled core effluent samples increased from approximately +0.6‰ before plateauing at +1.3‰. The proppant core effluent samples followed a similar trend over the first 12 days, increasing from +0.4‰ before plateauing at +1.3‰. The initial effluent $\delta^{138}Ba$ is within the same range as shale exchangeable values. However, these values steadily diverge and become higher than the shale exchangeable Ba.

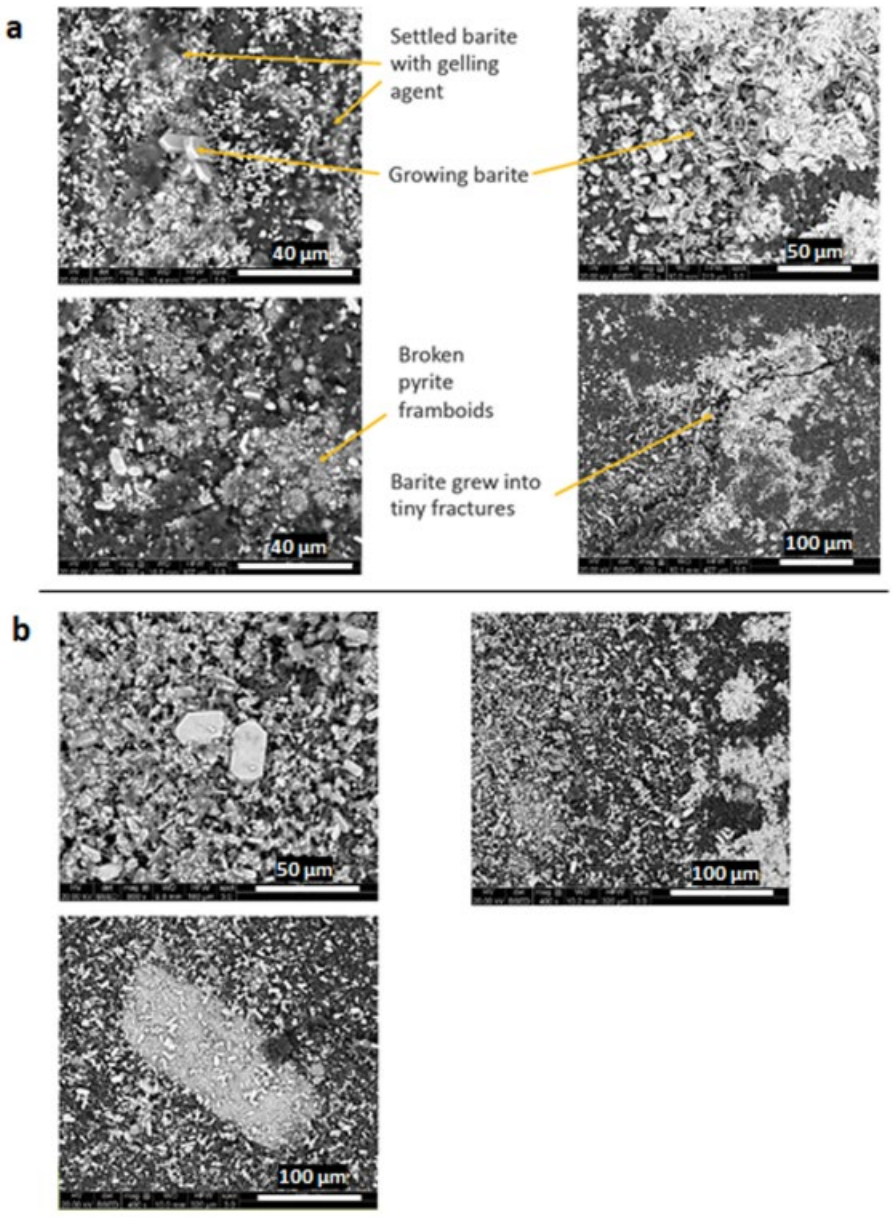

Figure 9: SEM images of post experiment barite pracipitated on (a) milled and (b) proppant cores.

Throughout the experiment, the milled and proppant effluent samples showed similar behavior for both Ba and sulfate concentration, as well as for δ^{138}Ba values. A simple box model was constructed to explain the flow-through results. Barium inputs for the fluid as it moved through the core included the influent SFF and Ba within the shale (most likely on cation exchange sites) [Phan et al., 2015; Renock et al., 2016; Stewart et al., 2015] This component was assigned the

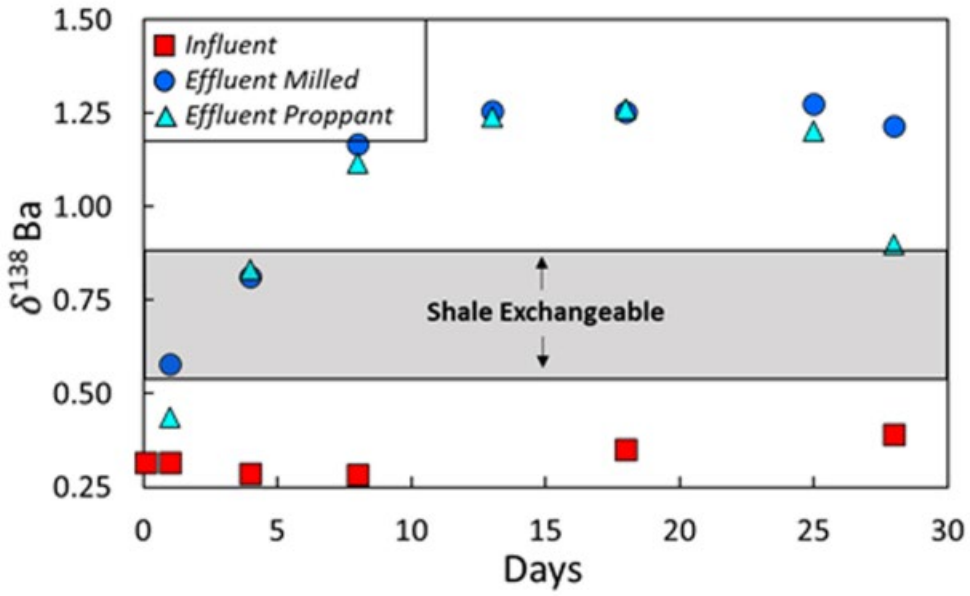

Figure 10: Barium isotope variation of flow-through influent and effluent samples. δ^{138}Ba increased for effluent samples over the first 7 days before remaining relatively constant. The shaded region represents the range of δ^{138}Ba values obtained for shale-exchangeable Ba.

lowest δ^{138}Ba value of exchangeable Ba reported in Table 6, which is comparable to exchangeable Ba determined from the same core by Tieman et. al (2020). The major Ba sink is the precipitation of barite, which leads to isotopic fractionation of Ba. A fractionation factor (α) of 1.0004 was used based on previously published fractionation factors.[von Allmen et al., 2010; Hsieh & Henderson, 2017]. The output was the measured Ba concentrations and isotopes for the effluent fluids. Two models were generated. In the first only influent Ba was considered as an input, and Ba concentrations were modified by barite precipitation. The second model included influent Ba and a flux of exchangeable Ba from the shale as inputs, with barite precipitation acting on these mixed sources. Both were modeled to decay exponentially to replicate the decrease in barite precipitation rate as sulfate decreased. Early in the experiment about 99.7% of influent Ba was precipitating as barite, and by the end, it had decreased to about 96.2%.

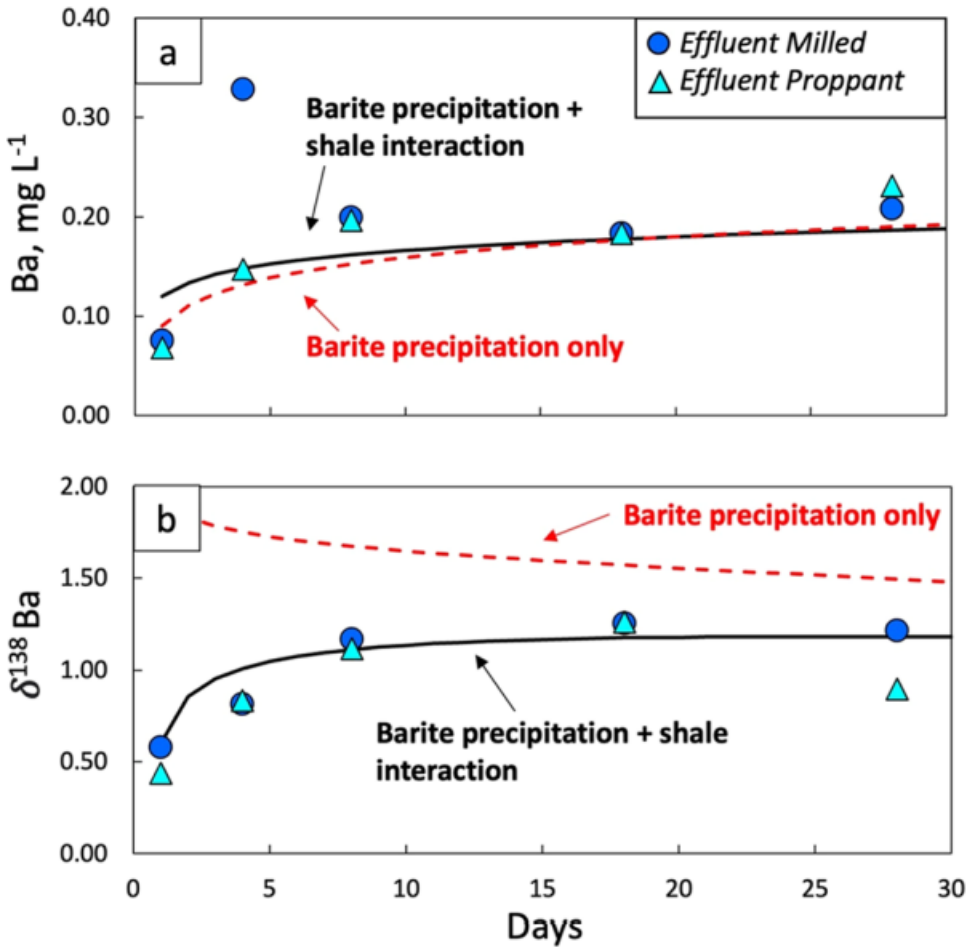

Figure 11: Plots of flow-through effluents with model result overlays. (a) Ba concentrations fit the data well for both models. (b) Modeling for δ^{138}Ba does not match the data when only considering barite precipitation (dashed red line). When the model incorporates shale interaction (solid black line), it shows a reasonable match to the observed data.

A model in which only influent Ba and barite precipitation is considered can explain the observed effluent Ba concentrations (dashed line, Figure 11a), with a greater rate of barite precipitation earlier in the experiment due to excess sulfate. However, barite precipitation alone cannot explain the δ^{138}Ba variation of the effluent samples, because the greater rate of barite precipitation early in the experiment would drive up the δ^{138}Ba of the fluid (dashed line, Figure 11b). To reconcile both the Ba concentrations and the variation in Ba isotope compositions, a shale

exchangeable component with low δ^{138}Ba (Figure 10) is required. By incorporating the release of shale exchangeable Ba (which contributed a flux of Ba equivalent to about 2.7% of the initial influent Ba flux, decreasing to about 2.5% following exponential decay) both the Ba concentrations and δ^{138}Ba values reasonably match the observed effluent values (solid lines, Figure 11b).

Because barite precipitation is greater earlier in the experiment, the fluid during this period has lower Ba concentrations and thus is more susceptible to isotopic modification by the shale-exchangeable component. In addition, the amount of Ba introduced from the shale could be greater at the early stages of the experiment while the shale has greater reactive surface area. While the precise pattern of exchangeable Ba release from the shale is non-unique, a low-δ^{138}Ba component is clearly required in the system to produce the observed data.

3.4 Conclusions

We carried out a series of batch and flow-through fluid-rock interaction experiments at temperature and pressure conditions similar to those at which injected fluid interacts with shale during hydraulic fracturing, with the goal of understanding potential sources of Ba and the behavior of barite under downhole conditions. Stable Ba isotopes of experimental products were analyzed to identify sources and processes affecting Ba in this system. Our major findings include the following:

•Based on benchtop hydrochloric acid-drilling mud/barite interaction experiments at 80°C, the injection of HCl at the start of hydraulic fracturing is unlikely to liberate large amounts of Ba into the fluid.

•Barite-HCl interaction experiments suggest minimal Ba isotope fractionation accompanying partial barite dissolution.

•Experimental interaction of synthetic fracturing fluid with shale and/or drilling mud at downhole conditions resulted in barite precipitation, rather than release of Ba into the fluid.

•Changes in Ba concentration and isotopic composition from flow-through experiments with synthetic fracturing fluid interacting with Marcellus Shale core are best explained by barite precipitation accompanied by a small amount of exchangeable Ba mobilization from shale surfaces. Barite precipitation is driven in part by release of sulfate from the shale, possibly due to oxidative dissolution of pyrite.

•The results of the experiments reported here indicate that the high-Ba concentrations in unconventional Marcellus Shale produced waters are not a result of interaction of injected fluids with shale and/or drilling mud during hydraulic fracturing. Instead they may indicate intrusion of high-Ba, high-δ^{138}Ba formation waters entering the well via subsurface fractures.

These experiments together show the complexities of fluid-rock interactions at downhole conditions for oil and gas wells. By understanding these processes future work can focus on determining the primary source of Ba in produced waters.

4.0 Barium Isotope Characterization of Hanover Shale Carbonate and Barite Nodules and Implications for Post-Depositional Fluid Flow in the Appalachian Basin

4.1 Introduction

Throughout the marine sedimentary record are numerous occurrences of nodule bearing horizons, particularly in marine shales [Brumsack, 2000; Clark, 1987; Lash, 2015; Dubinin & Uspenskaya, 2005]. The term nodule here refers to a mono- or multi- mineralogic mass, often spheroidal to ellipsoidal in shape, that has grown in situ. These can have both radiating rosette and concentric forms, and can form from precipitation on the sea floor or from the in-situ precipitation of minerals in shallow unconsolidated sediments [Clark, 1987; Mullins et al., 1980; Gregory et al., 2019]. After precipitation nodules can continue to be altered [Dubinin & Uspenskaya, 2005]. Because nodules are thought to precipitate from aqueous fluids [Clark, 1987; Gregory et al., 2019], nodule morphology and geochemistry can improve our understanding of fluid flow processes associated with sediment accumulation and diagenesis.

Horizons of barite ($BaSO_4$) nodules, often co-occurring with calcite nodules, are observed in the geologic records of many sedimentary basins [Bréhéret & Brumsack, 2000; Clark et al., 2004, Lash et al., 2015]. The processes that drive barite precipitation and preservation, particularly in the form of nodules, in shallow ocean sediments are still poorly understood [Hernandez-Sanchez et al., 2011; Bates et al., 2017]. Barium has historically been studied as a proxy for biogeochemical cycling in the ocean and has a relatively short residence time (~11 kyr) [Bates et. al. 2017; Von Allmen et. al., 2010, Church and Wolgemuth, 1972; Chan et. al. 1976]. Near the surface, dissolved Ba concentrations are low (~3 μg/L) due to the formation of barite microcrystals associated with

primary productivity. As depth increases the particulate barite dissolves and the concentrations of dissolved Ba increase (to ~200 μg/L) with minimal barite preservation in ocean sediments [Griffith & Paytan, 2012; Bacon & Edmund, 1972; Bates et. al. 2017]. However, the barite nodules observed in marine shales of sedimentary basins suggests that barite can be preserved under specific conditions.

In marine sediment pore fluids, a zone of bacterial sulfate (SO_4) reduction of organic matter tends to migrate downward over time. In cases where methane is produced at depth, a zone of microbially mediated anaerobic oxidation of methane can develop and migrate upward, depending on the methane flux. Where these zones meet, a region of sulfate and methane depletion of varying thickness and depth, known as the sulfate-methane transition zone (SMTZ) can develop [Knittel & Boetius, 2009; Lash, 2015]. Recent studies suggest that the formation of barite nodules and co-occurrence of carbonate nodules could be related to movement of the SMTZ and fluid diffusion from underlying units [Lash, 2015; Zan et al., 2022]. This paper investigates the record of fluid rock interactions in shallow marine sediments, from deposition through diagenesis preserved in carbonate and barite nodules of an Upper Devonian marine shale from the Appalachian Basin through the integration of field relationships, petrographic and chemical analysis, and Ba isotope composition. The application of stable Ba isotopes can provide insight into Ba cycling in the ocean, subsurface water to rock interactions, subsurface fluid flow, and more [Bates et. al., 2017, Horner et. al. 2015; Hsieh & Henderson, 2017; Cao et. al. 2016, Matecha et. al. 2022]. Relationships between the Ba isotope values for the carbonate and barite nodules as well as the physical characteristics and relationship between barite and carbonate will provide insight into the relative timing of precipitation (simultaneous vs. episodic) and the conditions under which precipitation occurred (fluid Ba concentration, fluid Ba source).

4.2 Background

4.2.1 Geologic Setting

The Appalachian Basin is a foreland basin covering a large part of the eastern US, including Pennsylvania and New York, and comprising Paleozoic stratified sedimentary rocks that exhibit repeated depositional cycles of organic rich black shales, clastic silty shales to sandstones, and limestones (Roen, 1983, Tillman & Barnes, 1983, Colton, 1961). Multiple shale and mudstone units within the basin contain horizons of Fe-Mn, barite, and carbonate nodules (Stiles et. al, 2001; Nuelle & Shelton, 1986).

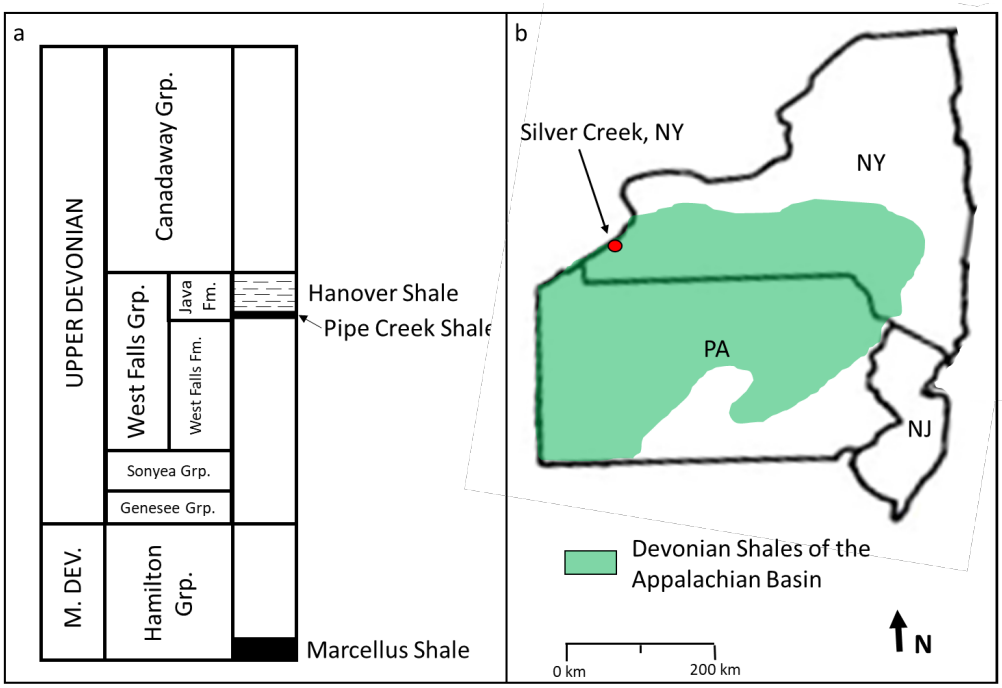

Figure 12: (a) Mid to Upper Devonian Units of the Western NY Appalachian Basin after Lash (2015). The Hanover Shale overlies the Pipe Creek Shale and together they make up the Upper Devonian Java Formation. The Hanover Shale lies approximately 260 m above the Marcellus Shale. (Diagram is not to scale) (b) Map of the extent of Devonian shales in PA and NY. The Hanover Shale outcrop located in Silver Creek, NY is marked in red.

The Middle to Upper Devonian sedimentary strata of western New York are characterized by the repetition of a black shale unit overlain by grey shale units with interbedded thin black shales. Lower strata are composed of marine shale which transitions gradually upward to shallow marine and brackish-water compositions with the succession thickening to the east (Baird and Lash 1990, Over, Jeffrey 1997). The Hanover Shale is an Upper Devonian interbedded black and grey marine shale (27-30 m thick) that overlies the Pipe Creek Shale (0.2-7 m thick), with both being members of the Java Formation (Figure 12) [de Witt, 1960; Lash, 2015]. The Hanover Shale lies approximately 260 m above the Middle Devonian Marcellus Shale. Multiple studies of the Hanover Shale have documented distinct carbonate nodule and barite nodule rich horizons parallel to bedding [de Witt, 1960; Over, 2002; Lash, 2015] and investigated the potential fluid-rock interactions that influenced the formation of these nodules.

4.2.2 Conceptual Model for Nodule Formation

Lash (2015) proposed that the formation and preservation of the barite and carbonate nodules of the Hanover Shale may have been driven by movement of the SMTZ due to changes in the migration of upward diffusing biogenic methane and fluids from the underlying Marcellus Shale or Utica Shale. The co-occurrence of barite and carbonate nodules and the formation of a barite rim on carbonate nodules would be unlikely to occur from a downward diffusing source of Ba with a stable SMTZ depth, as precipitation of barite would occur above the horizon of carbonate nodules rather than within the same horizon and on the carbonate. This suggests that a different fluid or mineralization process occurred. Lash (2015) suggests that if the Marcellus Shale's burial depth became deeper than the depth of maximum biogenic methane production, the SMTZ may have descended which led to precipitation of barite rims on the carbonate nodules and within

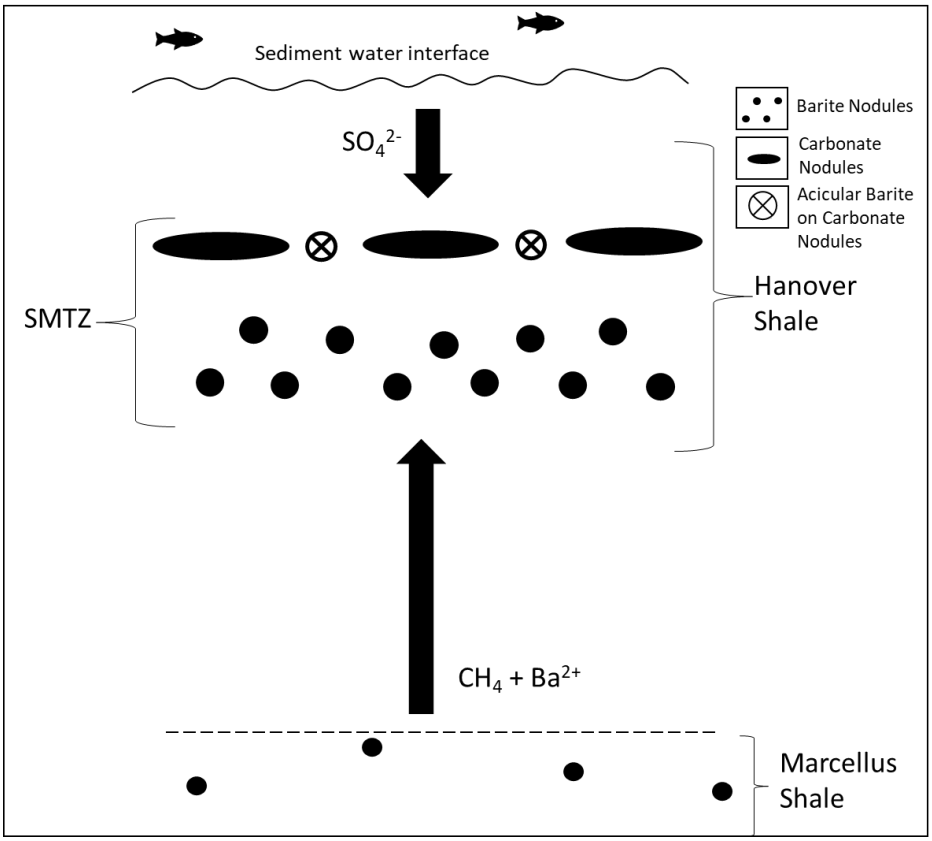

Figure 13: Conceptual model of fluid flow during diagenesis of the Hanover Shale. Modified from Lash (2015).

nearby horizons. In addition to the upward diffusing methane, there may also have been Ba rich fluids which migrated upward to the Hanover Shale and may have been a source of Ba for barite precipitation (Figure 13). Lash used $\delta^{34}S$, $\delta^{18}O$, and $\delta^{13}C$ to support the modeled upward diffusion of methane and movement of the SMTZ. However the source of Ba from which the barite precipitated could not be determined directly.

4.2.3 Application of Ba Isotopes

Barium isotopes are applied as a tool in the study of complex processes such as primary productivity in the ocean, water to rock interactions in ocean sediments, and the precipitation and

preservation of minerals [Bates et. al., 2017; Horner et al., 2015; Cao et al., 2016]. During precipitation of minerals such as barite, Ba undergoes mass-dependent isotope fractionation. In the case of barite, the lighter isotopes are preferentially incorporated into the solid and the fluid becomes isotopically heavier as a result [Von Allmen et al., 2010; Bottcher et al., 2012; Miyazaki et al., 2014]. This allows the ratio of Ba isotopes to be used as a tracer during processes such as fluid flow and fluid rock interactions [Matecha et al., 2022]. By analyzing the Ba isotope ratio of barite and carbonate nodules from the Hanover Shale we can determine the relative timing of the precipitation of carbonate and barite, whether nodules from different horizons precipitated from a fluid with the same composition, and constrain the source of Ba during precipitation by comparing the Ba isotope compositions of the nodules with potential source fluids.

4.3 Methods

4.3.1 Rock and Mineral Samples

The Hanover Shale is exposed in the study area at an outcrop along Walnut Creek in Silver Creek, NY where Walnut Creek is crossed by US-20. The outcrop parallels the river for approximately 200 m allowing for access without vegetation overgrowth. Near US-20 the bottom of the Hanover Shale's contact with the Pipe Creek Shale is at the creek bed. The Hanover Shale

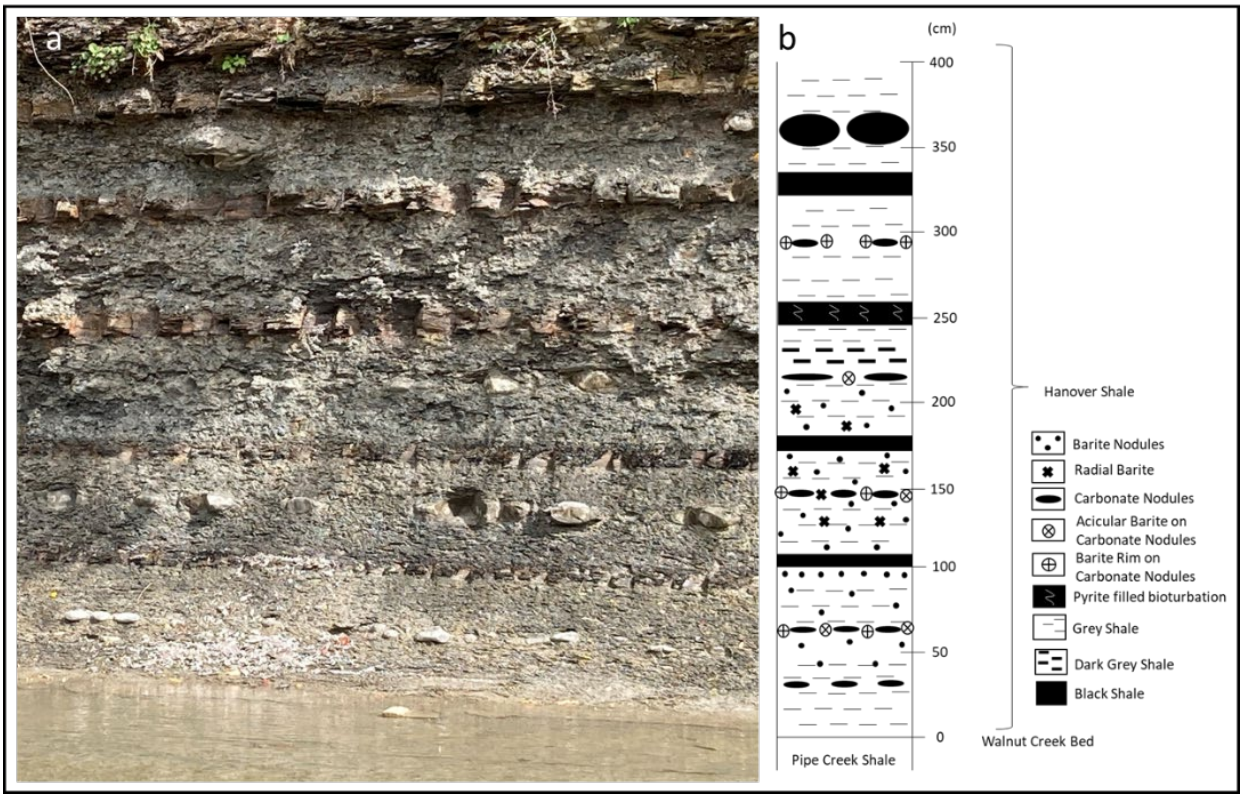

Figure 14: Walnut Creek outcrop of the Hanover Shale. (a) Photograph of the outcrop 40 m along Walnut Creek. The bottom 30cm of the Hanover Shale is underwater at this site. (b) Stratigraphic column for the Hanover Shale section at Walnut Creek in Silver Creek, NY aligned with the outcrop photograph in a.

at this location has a thickness of ~30 m, with the lower ~4 m visible and accessible at this outcrop (Figure 14a). It comprises repeated layers of grey shale with distinct horizons of carbonate and barite nodules, interspersed by 10 – 20 cm thick organic rich, pyrite rich, and often bioturbated black shales (Figure 14b).

Barite nodules and calcium carbonate concretions (some with a barite rim) were collected from various intervals throughout the stratigraphy of the unit and from multiple locations along the outcrop to provide both lateral and vertical continuity. Samples of barite nodules and carbonate nodules were collected from each horizon and were selected to represent the varied morphologies seen in the outcrop (aggregate barite, barite rim, acicular barite, etc.). Samples were additionally

Table 7: Barite and carbonate sampling heights and locations. (Bridge coordinates 42.537720, -79.168471)

Sample Name	Stratigraphic Height (cm)	Sampling Distance Upstream from Bridge	Sample Type
Barite			
WC-235-BAg	235	120 m	Barite Nodule
WC-235-CNBR	235	120 m	Carbonate Nodule Barite Rim
WC-225-CNBR	225	100 m	Carbonate Nodule Barite Rim
WC-E-160-BNC	160	100 m	Barite Nodule Center
WC-E-145-BNC	145	100 m	Barite Nodule Center
WC-B-145-CNBR	145	40 m	Carbonate Nodule Barite Rim
WC-80-CNBR	80	40 m	Carbonate Nodule Barite Rim
WC-50-BNE	50	5 m	Barite Nodule Rim
WC-50-BNC	50	5 m	Barite Nodule Center
Carbonate			
WC-I-290-CN	290	160 m	Carbonate Nodule
WC-225-CN	225	100 m	Carbonate Nodule
WC-C-220-CN	220	40 m	Carbonate Nodule
WC-C-145-CN	145	40 m	Carbonate Nodule
WC-B-145-CN	145	20 m	Carbonate Nodule
WC-A-145-CN	145	5 m	Carbonate Nodule
WC-80-CN	80	40 m	Carbonate Nodule
WC-C-65-CN	65	40 m	Carbonate Nodule
WC-A-30-CN	30	5 m	Carbonate Nodule

taken laterally along the outcrop approximately every 20 m where the outcrop was accessible. A list of stratigraphic heights and locations for samples is shown in Table 7.

4.3.2 Petrography

Two barite nodules and two carbonate nodules with barite rim were mounted as standard petrographic thin sections with a thickness of 30 μm. One barite nodule required light epoxy impregnation due to its more friable texture. The carbonate nodules with barite rim were cut to center the border between the carbonate and barite rim. The thin sections were examined using a

Leica petrographic microscope and photomicrographs were taken under plane polarized and cross polarized light.

4.3.3 Sample Preparation and Dissolution

Each carbonate nodule had a ~2 cm slab cut from the center (with barite rim being removed where necessary) which was pulverized using a mixer mill and a precisely weighed aliquot (generally around 100 mg) of the pulverized sample was added to an acid-cleaned 15 mL centrifuge tube. To remove labile (exchangeable) cations from mineral surfaces, 10 mL of ammonium acetate (buffered to pH 8) was added to each centrifuge tube. Each tube was agitated using a wrist-action shaker for 4 hours and centrifuged for 10 minutes at 4000 rpm. The solution was pipetted out and discarded leaving visible solids, which were then rinsed with ~10 mL of 18.2 MΩ Milli-Q water (MQW), and the solution again pipetted out and discarded.

To dissolve the carbonate, 10 mL of 1M acetic acid was added and the tubes were left loosely capped for 1 hour to allow for the release of CO_2 gas. Each tube was agitated for 8 hours and then centrifuged for 10 minutes at 4000 rpm. The solution was then pipetted out into acid-cleaned 50 mL PMP containers. The remaining solids were rinsed with 10 mL of MQW, centrifuged for 10 minute at 4000 rpm, and the solution pipetted into the same PMP containers, leaving behind any remaining solids. Each sample was evaporated to dryness at 90°C, dissolved in 20 mL of 2% HNO_3, and transferred to acid-cleaned HDPE bottles.

Barite nodules had minimum samples of 50 mg collected from the center and the rim of the barite nodules by breaking them apart using a small hammer steel dental probe. The barite rims on carbonate nodules were removed from the ~2 cm thick carbonate nodule slabs using a hammer and steel dental probe. These samples as well as select whole barite nodules were individually

pulverized using a dedicated Diamonite^{TM} synthetic sapphire mortar and pestle. For each barite sample an aliquot of 20 mg of the pulverized sample was added to acid-cleaned 15 mL centrifuge tubes. To remove any adhering carbonate, 2 mL of acetic acid was added to each centrifuge tube. Each tube was agitated using a wrist-action shaker for 12 hours and centrifuged for 10 minutes at 4000 rpm. The solution was then pipetted out and discarded, the solids rinsed with ~10 mL of MQW, and the solution was again pipetted out and discarded leaving any remaining solids. The remaining barite solids were then converted to witherite via exchange reaction with Na_2CO_3 and dissolved following the barite dissolution procedure of Matecha et. al. (2021). Each sample was evaporated to dryness at 90°C, dissolved in 20 mL of 2% HNO_3, and transferred to acid cleaned HDPE bottles.

4.3.4 Elemental Analysis

An 8 mL aliquot of each dissolved barite solution was diluted with 12 mL of 2% HNO_3, and a 1.6 mL aliquot of each dissolved carbonate solution was diluted with 18.4 mL of 2% HNO_3 to bring expected TDS in each solution below 500 ppm in preparation of elemental analysis. Aliquots from a subset of samples were analyzed for major and trace elements by ICP-OES and ICP-MS by Activation Laboratories Ltd. and the remaining subset was analyzed by ICP-MS at the University of Pittsburgh.

4.3.5 Ba Separation and Isotope Analysis

Preparation for Ba isotope analysis differed for carbonate and barite solutions. Aliquots of both the carbonate and barite solutions containing 2 μg Ba were pipetted into preweighed 15 mL

acid-cleaned Teflon vials and spiked with a calibrated ^{137}Ba-^{135}Ba double spike at a spike/sample ratio of ~0.7 to account for mass fractionation. All samples were evaporated to dryness at 90°C. The carbonate samples were redissolved in 1 mL of concentrated HCl, evaporated to dryness at 90°C, dissolved in 0.5 mL of 2.5 M HCl, and sonicated for 30 minutes. Ba separation was conducted using cation exchange columns following the procedure of Matecha et. al. (2021). Samples were eluted using a combination of 2.5 M HCl and 2.0 N HNO_3 through cleaned cation exchange columns loaded with AG-50W, 200-400 mesh cation exchange resin. The eluent Ba samples were collected in 15 mL acid-cleaned Teflon vials and evaporated to dryness at 90°C. The barite samples did not require further separation due to the high ratio of Ba to all other constituents in the samples.

Both the barite samples and the separated carbonate Ba samples were redissolved in 1 mL of concentrated HNO_3, sonicated for 10 minutes, evaporated to dryness at 90°C, dissolved in 4 mL of 2% HNO_3, and sonicated for 60 minutes before being transferred to acid-cleaned 15 mL centrifuge tubes for Ba isotope analysis.

Barium isotope ratios were measured on the DOE-NETL Thermo Neptune Plus® MC-ICP-MS at the University of Pittsburgh. Eight Faraday collectors were simultaneously used to measure abundances of $_{134}$Ba, ^{135}Ba, ^{136}Ba, ^{137}Ba, and ^{138}Ba. They also measured isobaric interferences from ^{134}Xe, ^{136}Xe, ^{136}Ce, ^{138}Ce, and ^{138}La by using the masses of non-overlapping isotopes ^{131}Xe, ^{139}La, and ^{140}Ce. Barium isotope ratios are reported using δ^{138}Ba notation with units of permil (‰). This is calculated using NIST 3104a as the normalizing standard:

$$\delta^{138}Ba(‰) = 10^3 \left[\frac{\left(^{138}Ba/^{134}Ba\right)_{sample}}{\left(^{138}Ba/^{134}Ba\right)_{standard}} - 1 \right]$$

Interspersed throughout the sample runs on the MC-ICP-MS, the NIST 3104a Ba standard (spiked with the same ^{137}Ba-^{135}Ba double spike) was analyzed and the sample values were

normalized to the average standard value. For additional information about the analyses, see Supporting Information in Tieman et. al. (2020).

4.4 Results

4.4.1 Nodule Morphology

The barite nodules are spheroidal to ellipsoidal in shape with sizes ranging from 1 cm to 15 cm in diameter. Most barite nodules show a distinct center of fine-grained barite crystals surrounded by radiating needle like barite (Figure 15a). Some barite nodules have grown together into aggregate nodules with multiple center points (Figure 15b). The carbonate nodules are ellipsoidal in shape and are fairly consistent in size within their horizon, but differ greatly in size ranging across horizons from a width of ~10cm to ~50cm parallel to layering. Multiple horizons show carbonate nodules with distinct 1-2 cm thick barite rims with the barite showing the same morphology as the barite nodules found separately (Figure 15c).

Occasional carbonate nodules have small surficial acicular barite starbursts (Figure 15d). Highly weathered friable barite can be found in the lenticular edges of many carbonate nodules. For both barite and carbonate nodules the surrounding shale has distinct contacts suggesting the nodules formed in the unconsolidated sediments which then lithified around the nodules. Within some of the grey shale and the majority of the black shale, pyrite and bioturbation are present, including pyritization of trace fossil burrows visible in certain black shale horizons. Lash (2015) notes the presence of mm-scale pyrite nodules and pyritized ammonoids and goniatites.

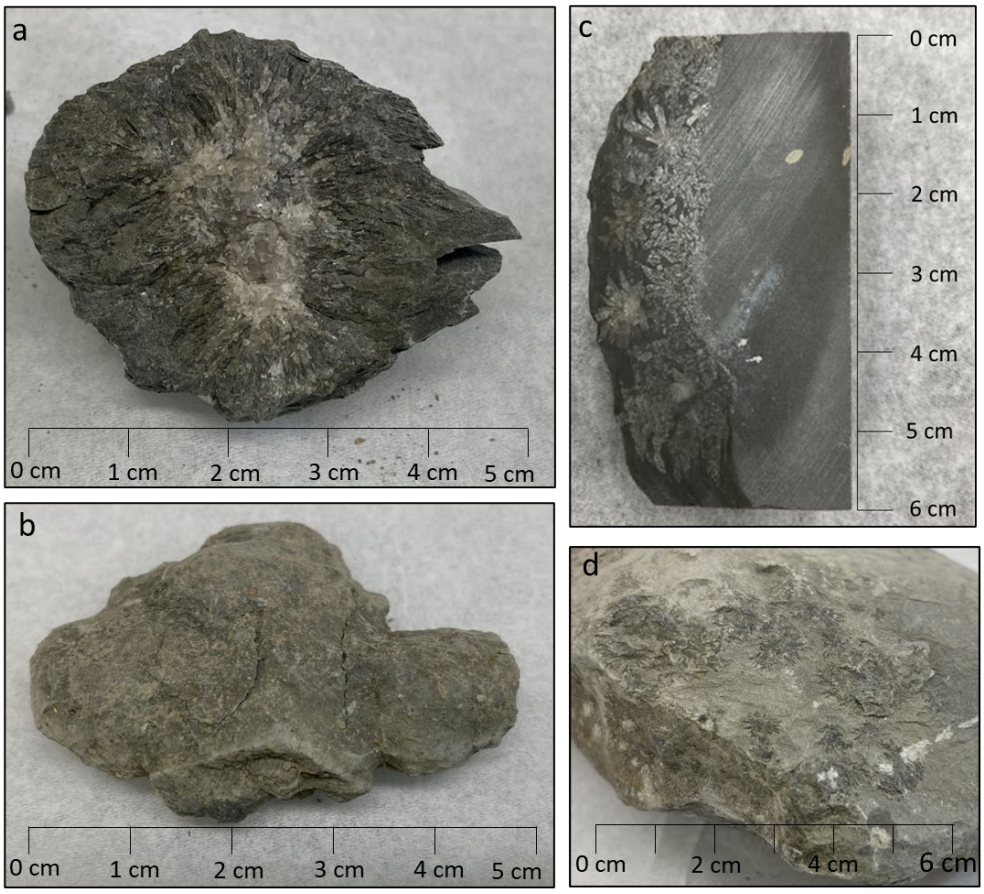

Figure 15: Barite sample morphologies. (a) Radial barite nodule with distinct center surrounded by radiating barite crystals. (b) Aggregate barite nodule with intergrowth of multiple distinct barite centers with radiating barite. (c) Carbonate nodule with cm thick barite rim (left) with distinct radial barite crystals visible. (d) Acicular surficial barite on a carbonate nodule.

4.4.2 Petrographic Analysis

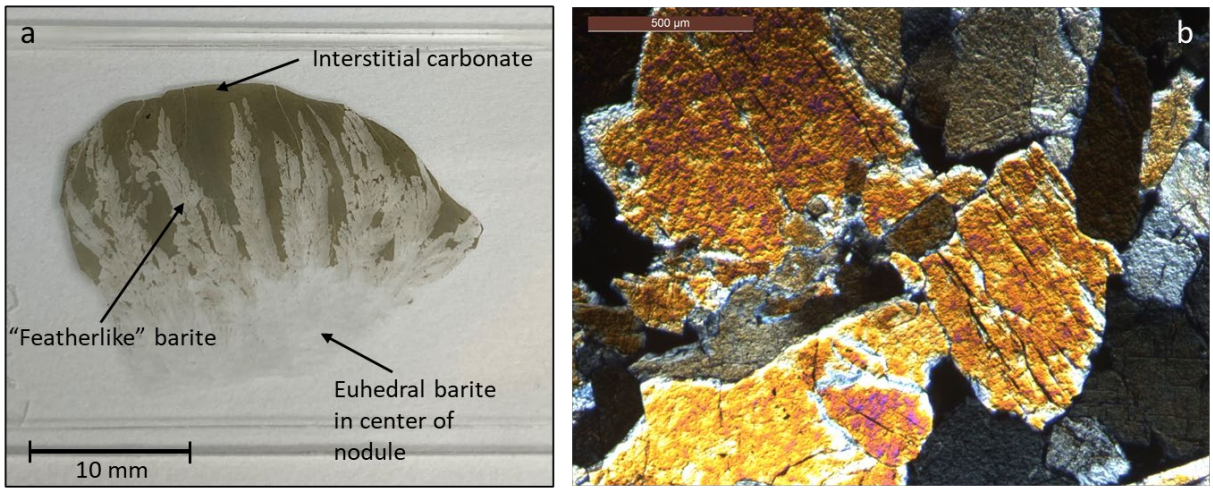

Figure 16: Barite nodule photomicrographs. (a) Thin section of WC-235-BAg. Distinct "featherlike" radial barite is visible with interstitial carbonate near the outside edge. (b) Photomicrograph showing the relatively pure euhedral barite center of the barite nodule.

Petrographic examination showed that barite nodules had centers of euhedral to anhedral intergrown barite crystals (Figure 16). Radiating from these centers were feather-like elongate barite crystals (7-11 mm long "feathers" with ~0.2 mm crystals) with interstitial carbonate becoming more prominent near the edges of the nodule (Figure 16a).

Although some carbonate nodules do not have barite rims, small (~2 mm diameter) radial barite nodules were observed within the carbonate (Figure 17a). In comparison to separate barite nodules, the barite nodules within carbonate nodules were more compact with distinct flower-like radiating barite crystals around a euhedral barite center with prominent interstitial carbonate (Figure 17b). Figure 17c shows a carbonate nodule with barite rim with a distinct boundary between barite and carbonate, although the barite still had interstitial carbonate present. Barite near the boundary of barite and carbonate (~2 mm thick) was similar in morphology to that in the center of barite nodules, with most barite being small (~400 µm) euhedral to anhedral randomly oriented

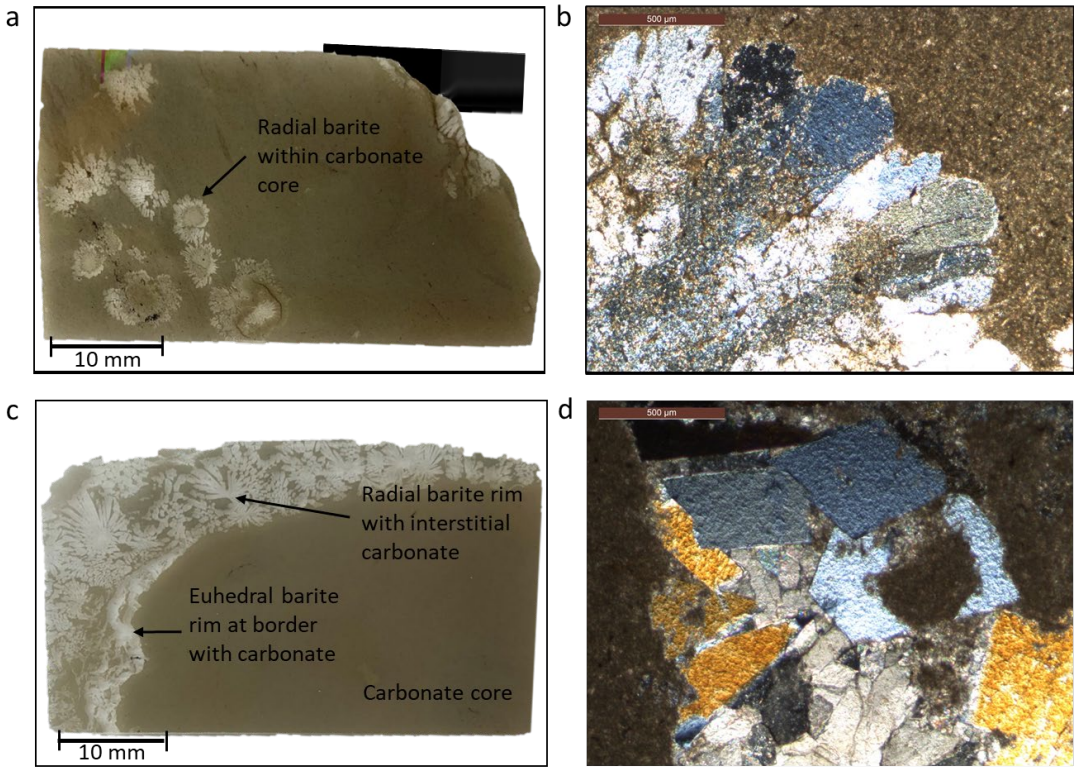

Figure 17: Carbonate nodule photomicrographs. (a) Thin section of WC-80-CN with visible radial barite within the carbonate matrix. (b) Photomicrograph of a under XPL showing contact between radial barite and the carbonate. The radial barite has interstitial carbonate in both the center and edges. (c) Thin section of WC-235-CN and its barite rim WC-235-CNBR. The rim has euhedral barite near the contact boundary transitioning to radial moving outward. (d) Photomicrograph of c under XPL showing the euhedral to anhedral barite occurring at the boundary between the carbonate and barite rim.

crystals (Figure 17d). Outward away from the contact barite morphology transitions to radial nodules as seen within the carbonate and barite nodules.

4.4.3 Barium Isotope Analysis

Isotope data for carbonate nodules, barite nodules, and barite rim, presented as $\delta^{138}Ba$, can be found in Table 8.

Table 8: Barium isotope and concentration data for barite and carbonate nodules. Barium concentrations were not measured in the barite samples, but stoichiometric barite contains 588,420 µg/g Ba.

Sample Name	δ^{138}Ba (‰)	µg Ba/g sample
Carbonate		
WC-I-290-CN	0.368 ± 0.069	171
WC-225-CN	0.426 ± 0.023	1039
WC-C-220-CN	0.423 ± 0.077	562
WC-C-145-CN	0.736 ± 0.059	172
WC-B-145-CN	0.581 ± 0.058	367
WC-A-145-CN	0.473 ± 0.078	626
WC-80-CN	0.324 ± 0.030	428
WC-C-65-CN	0.391 ± 0.067	581
WC-A-30-CN	0.358 ± 0.066	186
Barite		
WC-235-BAg	0.476 ± 0.028	
WC-235-CNBR	0.445 ± 0.042	
WC-225-CNBR	0.439 ± 0.033	
WC-E-160-BNC	0.578 ± 0.050	
WC-E-145-BNC	0.629 ± 0.064	
WC-B-145-CNBR	0.375 ± 0.071	
WC-80-CNBR	0.444 ± 0.029	
WC-50-BNE	0.318 ± 0.032	
WC-50-BNC	0.204 ± 0.043	

4.4.3.1 Carbonate Nodules

The carbonate nodules sampled from various horizon heights and distances along the outcrop displayed a wide range of δ^{138}Ba, from 0.32 to 0.74 ‰ (Figure 18a). Nodules from the horizon at a stratigraphic height of 145 cm were collected at 5m (A), 20 m (B), and 40 m (C) distances along the outcrop and displayed the widest range and heaviest δ^{138}Ba values of the carbonate samples (0.47 to 0.74 ‰). Other horizons of carbonate nodules were isotopically lighter, within the range of 0.32 to 0.43 ‰. No notable trends were observed across vertical sampling, while a slight increasing of δ^{138}Ba was observed moving away from the bridge. There was no notable relationship between Ba concentration and δ^{138}Ba values across samples as a whole (Figure

19). However, when considering the three nodules at the 145 cm horizon (A, B, and C in Figure 19), the Ba concentration showed an inverse correlation with the δ^{138}Ba.

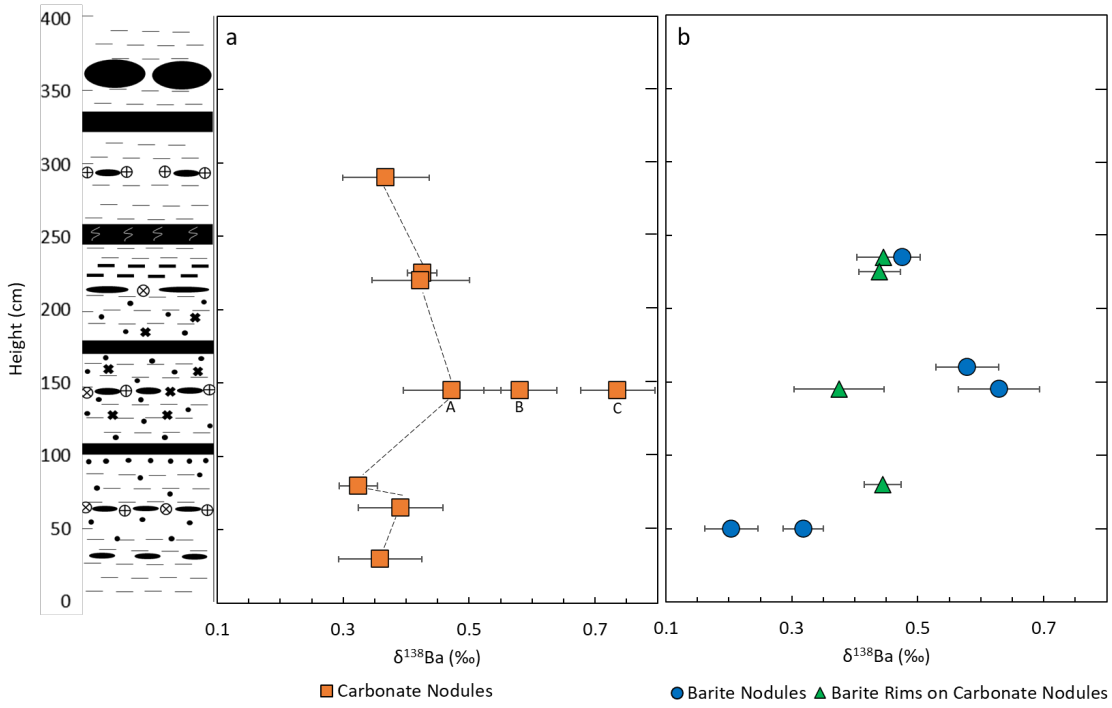

Figure 18: δ^{138}Ba (‰) values for carbonate and barite compared to height of the sampling horizon within the outcrop on the left. (a) δ^{138}Ba (‰) values for carbonate nodules. (b) Comparison of δ^{138}Ba (‰) values for barite nodules and barite rims on carbonate nodules.

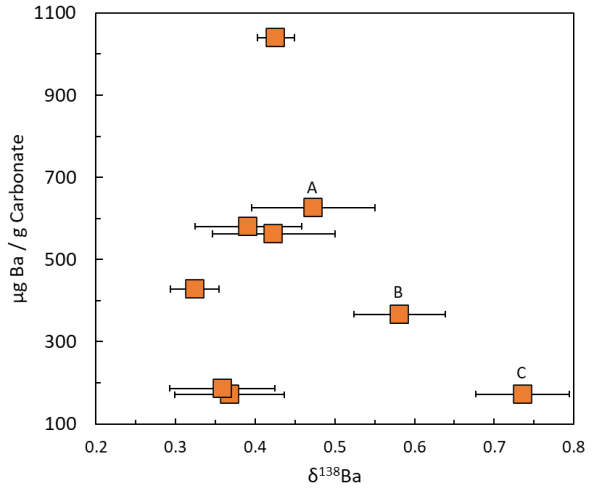

Figure 19: Comparison of δ^{138}Ba (‰) values of carbonate nodules with Ba concentrations (in µg Ba per g of carbonate).

4.4.3.2 Barite Nodules

The barite samples (both barite rim on carbonate nodules and barite nodules) had $\delta^{138}Ba$ values ranging from 0.20 to 0.63 ‰ and showed a general increase in $\delta^{138}Ba$ with stratigraphic height (Figure 18b). In the case of a nodule collected at a stratigraphic height of 50 cm the nodule center was 0.20 ‰ while the rim was 0.32 ‰, a difference outside of measurement uncertainty (Figure 20).

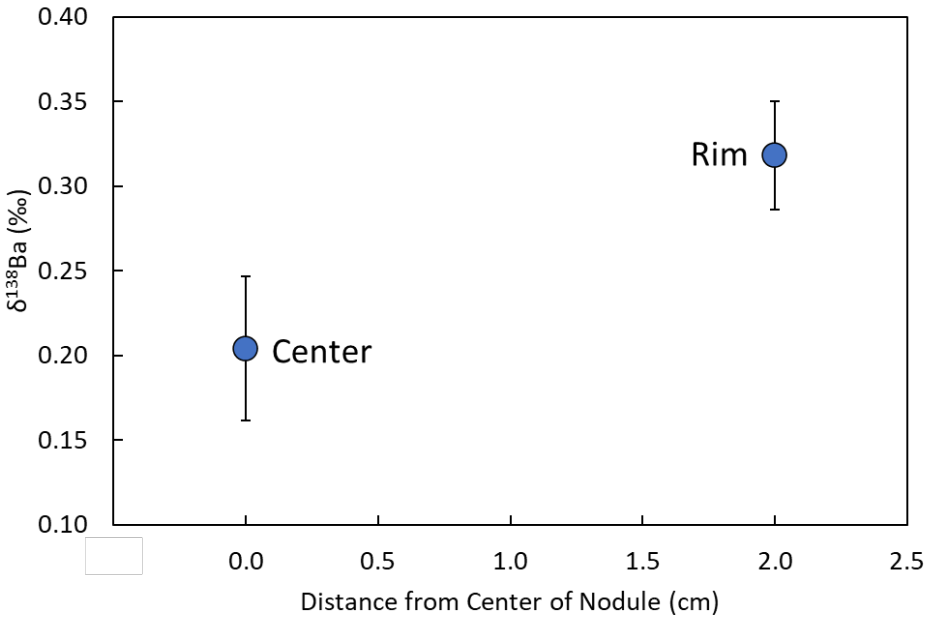

Figure 20: Comparison of $\delta^{138}Ba$ (‰) values for the center and rim of a barite nodule from the 50 cm barite nodule horizon.

4.4.3.3 Barite Rim on Carbonate Nodules

The barite rims on carbonate nodules did not display any systematic trends relative to the carbonate cores (Figure 21). The nodule at 80 cm had a heavier barite rim (0.44 ‰) and a lighter carbonate core (0.32 ‰), while the nodule at 145 cm had a heavier carbonate core (0.58 ‰) and a lighter barite rim (0.37 ‰), and the nodule at 220 cm had a rim and core within measurement uncertainty of each other (0.43 ‰).

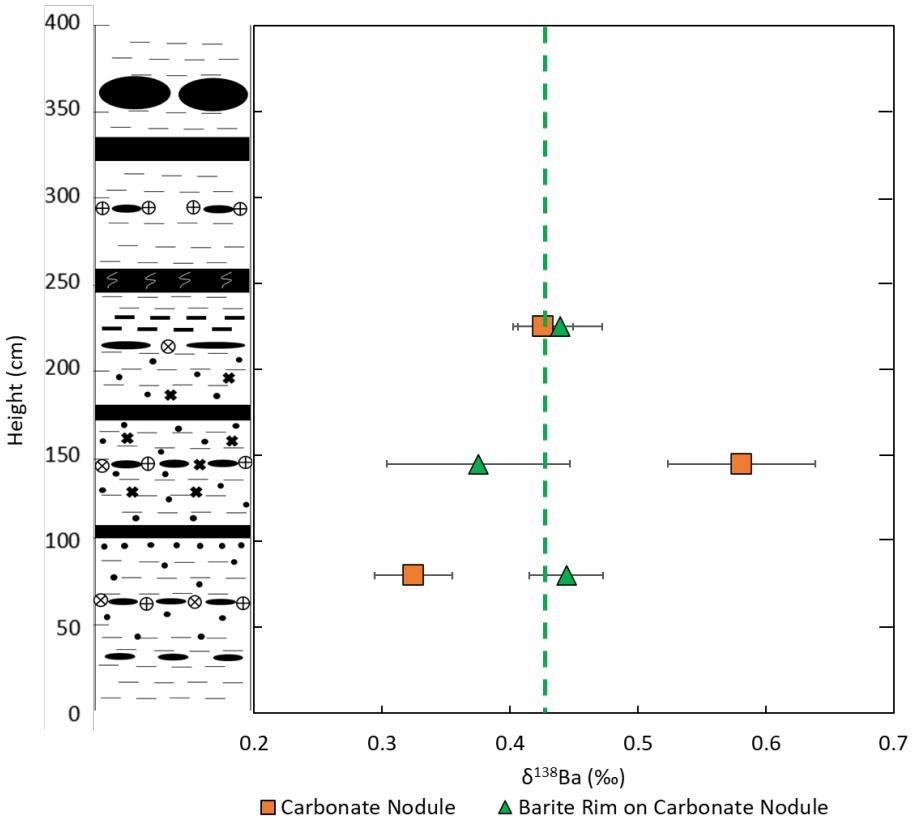

Figure 21: Comparison of carbonate nodules and barite rim on carbonate nodules δ^{138}Ba (‰). Outcrop stratigraphy is shown on the left. Dashed green line shows overlap of barite rim uncertainty.

4.5 Discussion

4.5.1 Changes in Ba Input Reflected in Barite Nodules

The morphological transition from smaller euhedral to anhedral barite crystals in the center of barite nodules and at the contact of barite on carbonate nodules, to larger radiating barite crystals on the outer rim of barite on carbonate nodules and the rim of barite nodules has multiple potential implications. Studies have linked fluids with lesser barite supersaturation precipitating smaller

euhedral to anhedral barite crystals and fluids with greater barite supersaturation precipitating radiating barite crystals [Shikazono, 1994; Castellini et. al., 2006]. If the concentration of Ba was the controlling factor on fluid barite supersaturation then the barite crystal morphology may reflect an increase in the Ba concentration of the fluid. However, this is the opposite of what would be expected with continuous barite precipitation, as Ba would be depleted from the fluid over time due to incorporation in barite. If the concentration of sulfate was the controlling factor then it is possible that an increase in sulfate in an otherwise Ba-rich fluid led to the change in barite crystal morphology.

When comparing the δ^{138}Ba values for center and rim of the barite nodules, the center is isotopically lighter while the rim in isotopically heavier, which would be consistent with mass fractionation of a source fluid due to barite precipitation. This could also be explained if the barite nodule forming horizons followed a trend of initial lesser barite supersaturation fluid followed by introduction of an isotopically heavier, greater barite supersaturation fluid. Upward migrating fluids from lower units may have been isotopically heavier, as suggested by the high δ^{138}Ba of Marcellus Shale formation waters [Tieman et al., 2020].

Another possibility is that the transition from lesser to greater supersaturation of barite reflects a change in sulfate content. Downward movement of the SMTZ associated with changes in methane flux would allow for more sulfate rich fluids to diffuse downward into the barite precipitating horizon and increase barite supersaturation. It is possible that both upward diffusing isotopically heavier Ba rich fluids and downward diffusing sulfate interacted and together caused an increase in barite supersaturation and associated transition to radial barite morphology.

4.5.2 Relationship Between Barite and Carbonate Nodules

The lack of $\delta^{138}Ba$ trend in the relationship between barite rim and carbonate core suggests that the barite did not precipitate onto the carbonate nodules at the same relative times for each sample. The variability of $\delta^{138}Ba$ for the carbonate cores (Figure 21) suggests that the source that contributed Ba may have changed between the formation of each carbonate horizon. In contrast, the $\delta^{138}Ba$ for the barite rims overlapped with measurement uncertainty (Figure 21, dashed green line) which may reflect precipitation from Ba rich fluids with similar $\delta^{138}Ba$ compositions, possibly from the same source. Observed distinct boundaries between the carbonate nodule and barite rims in thin section, as well as the differences in $\delta^{138}Ba$ between the barite and carbonate, suggest the precipitation of barite onto the carbonate nodule at a later time and likely with a different source of Ba.

A conceptual model for the formation of carbonate and barite nodules is presented in Figure 22. The presence of the barite on carbonate nodules suggests that after the carbonate nodules had precipitated (Figure 22a), the SMTZ shifted downward exposing the carbonate nodules to the sulfate reduction zone where barite precipitation occurred (Figure 22b). Similar to the barite nodules, a euhedral barite precipitated first on the carbonate nodules and transitioned to more radial crystal habits (Figure 22c), which may reflect the same pattern of precipitation from initially moderate Ba concentration fluids in a variable, rock dominated system, followed by a late pulse of high Ba concentration fluids to precipitate the rims. Finally, the sediment around the barite rimmed carbonate nodule lithified forming shale (Figure 22d). These trends are consistent with the observations of Lash (2015) for the timing of barite precipitation.

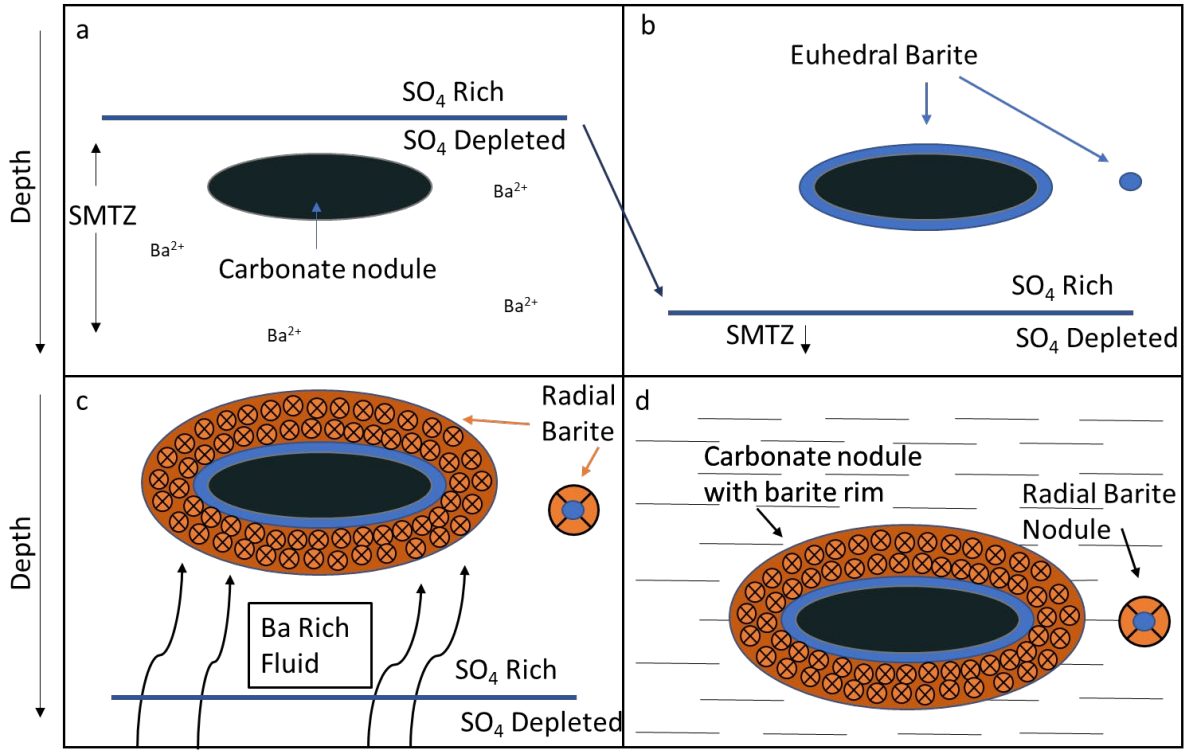

Figure 22: Diagram of the cross section view of the precipitation of the barite rim on carbonate nodules in shallow sediments at the SMTZ. (a) Carbonate nodule formation in the sulfate depleted zone. (b) SMTZ shifts downward due to a change in methane flux. Sulfate reacts with available Ba to form euhedral barite rim on carbonate nodule. (c) Diffusion upwards of Ba rich fluids. Precipitation of radial barite layer on rim of carbonate nodule. (d) Continued burial of the nodule and lithification of surrounding sediment to form shale.

4.5.3 Fluid (Ba) Sources During Diagenesis:

When the range of δ^{138}Ba values of the Hanover Shale barite and carbonates (0.20 – 0.74 ‰) is compared with the range of seawater (0.1 – 0.6 ‰) and Marcellus formation fluid values (0.35 – 1.5 ‰) [Tieman et al., 2020; Matecha et al., 2022] most of the sample δ^{138}Ba values overlap with one or both of these (Figure 23). The fluid from which the barite nodules precipitated was likely isotopically heavier than the barite nodules themselves, while the isotopic offset between

carbonate and fluid is less clear [von Allmen, 2010; Wang et al., 2021]. Given that, the fluids that precipitated the highest- δ^{138}Ba barite nodules would have been heavier than modern seawater yet still well within the range of Marcellus Shale formation waters. It is possible that isotopically heavier Ba rich fluids migrated upward from the Marcellus Shale or deeper units along with methane and were the source of Ba from which barite precipitated during the diagenesis of the Hanover Shale.

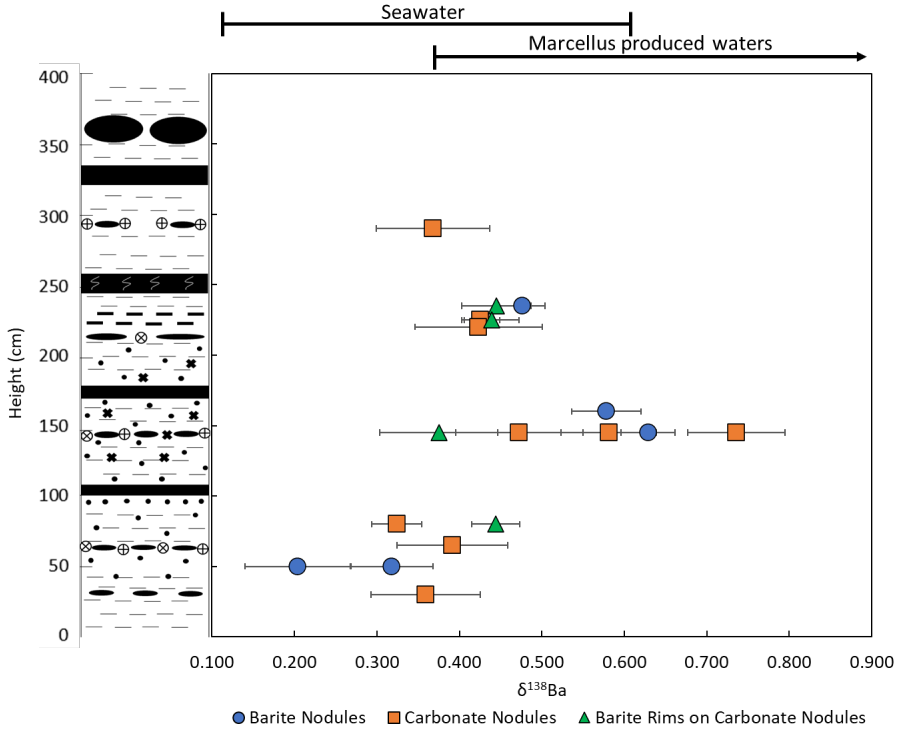

Figure 23: δ138Ba (‰) values for carbonate and barite compared to height of the sampling horizon within the outcrop on the left. δ138Ba (‰) ranges for seawater and Marcellus waters is shown above the plot.

4.6 Conclusions:

Barite and calcium carbonate nodules from the Upper Devonian Hanover Shale were analyzed using Ba isotopes and thin section petrography to determine the formation conditions and

relative timing of nodule precipitation, and to constrain the possible sources that contributed Ba-rich fluids from which nodules precipitated. Variability of $\delta^{138}Ba$ values across carbonate and barite samples suggests that precipitation occurred in a sediment-dominated system at the depth of the SMTZ. Differences in $\delta^{138}Ba$ from the center to the edge of barite nodules and the change in barite crystal morphology may have been caused by mass fractionation of the fluid and a sudden increase in fluid barite supersaturation due to upward diffusion of an isotopically heavier Ba-rich fluid and/or downward diffusion of sulfate. The distinct $\delta^{138}Ba$ values for carbonate nodules from different horizons suggests that the $\delta^{138}Ba$ composition of the fluid changed between precipitation of different carbonate horizons, either due to local fluid-rock interaction or to changes in the source of Ba. This may support the episodic introduction of upward diffusing Ba rich fluids alongside upward diffusing methane which led to the movement of the SMTZ.

The distinct barite and carbonate horizons of the Upper Devonian Hanover Shale are consistent with the proposed conceptual model of Lash (2015) where movement of the SMTZ related to changes in the upward diffusion of methane led to barite precipitation on carbonate nodules and preservation of barite nodules. Accounting for fractionation during barite and carbonate precipitation, the $\delta^{138}Ba$ for the nodules within the Hanover Shale falls into the range of Marcellus formation fluids. It is possible that upward diffusing fluids from the Marcellus Shale could have been the source of isotopically heavier Ba to the Hanover Shale during diagenesis. Alternative sources of upward diffusing fluids include the Utica Shale, and other mid Devonian to Ordovician shales. It is also possible that the barite nodules within the Hanover Shale also contain a significant seawater Ba component. Future work may include sampling of barite from underlying units and comparison of $\delta^{138}Ba$ and $^{87}Sr/^{86}Sr$ from those units with that of the Hanover Shale carbonate and barite samples.

Appendix A: Supplemental Materials for Chapter 2

Appendix Table 1: Thermo Element® ICP-MS signal intensity (in counts per second) for a column calibration using 2.0 N HCl for the entire elution of a dissolved silicate volcanic rock. All column cuts were diluted to 15 mL prior to analysis. The data (recalculated as fraction of total eluted) are plotted in Appendix Figure 1 (top).

mL added to column	Cumulative volume	Na23(MR)[a] cps[c]	Mg24(MR) cps	Ca46(MR) cps	Fe56(MR) cps	Sr88(LR)[b] cps	Ba137(LR) cps	La139(LR) cps	Ce140(LR) cps
0.5	0.5	1345851	31152	79	14956	21449	1874	951	1865
0.5	1	2143399	1172966	833256	66505	76611	37784	2330	3673
0.5	1.5	3298254	2010265	2703534	4550209	116555	54060	3222	4343
0.5	2	2299369	432109	94416	34331941	22454	6390	664	1326
2	4	102604622	13477017	92887	164870323	34102	8974	803	1326
5	9	29013226	58298212	53751	62935406	86154	8246	506	1103
5	14	1182372	158898	10401	176996	5891739	7061	433	889
5	19	920620	25719	1125	23286	20384998	5873	489	981
5	24	1291038	12356	322	13850	5031319	5094	392	925
5	29	955782	14252	132	22001	1376019	15593	686	1195
5	34	937024	12539	123	70376	266045	138942	811	1429
5	39	935974	19311	161	47358	58117	612423	884	1579
5	44	859736	9399	146	38899	14227	1048728	934	1179
5	49	1111384	15348	83	104323	7614	896031	942	3222
5	54	891796	9413	108	55600	4482	564025	964	12143
5	59	960798	13612	96	161226	5598	288738	1840	51083
5	64	1017963	10699	102	115298	5052	116921	6168	156128
5	69	1097870	16680	118	40191	8972	46852	19459	351238
5	74	978701	12088	104	24152	4446	18894	48853	606227
5	79	962035	10026	103	21188	3818	7770	105846	809252
5	84	998579	11650	86	17391	6120	3551	183511	855501
5	89	963740	10525	121	20352	3181	1757	263467	776097
5	94	1004586	12021	101	46590	4249	1103	312101	596161
5	99	1075873	23521	154	24493	4135	1106	342744	413320
5	104	1314092	19579	159	32156	3626	2694	303603	265305

[a](MR) = medium resolution data acquisition
[b](LR) = low resolution data acquisition
[c]Intensities of all measured elements are adjusted by the addition of In (10 µg/L) as an internal standard.

Appendix Table 2: Thermo Element® ICP-MS signal intensity (in counts per second) for a column calibration using 2.5 N HCl for the entire elution of a dissolved silicate volcanic rock. All column cuts were diluted to 15 mL prior to analysis. The data (recalculated as fraction of total eluted) are plotted in Appendix Figure 1 (bottom).

mL added to column	Cumulative volume	Na23(MR)[a] cps[c]	Mg24(MR) cps	Ca46(MR) cps	Fe56(MR) cps	Sr88(LR)[b] cps	Ba137(LR) cps	La139(LR) cps	Ce140(LR) cps
0.5	0.5	867209	7225	88	81653	6365	695	533	728
0.5	1	1870432	771774	579577	83810	56004	26533	1654	2391
0.5	1.5	2679033	1421703	2380064	12896816	87592	43599	2227	3178
0.5	2	1785031	407321	88847	52180080	18594	5865	475	695
2	4	92642584	43613830	92384	143970784	34823	7773	453	945
5	9	8837988	15475645	24601	3430386	2008859	8863	622	1028
5	14	1637760	204852	8066	530745	59409591	23356	1754	3334
5	19	1216770	10043	219	66994	3645621	5642	433	939
5	24	1220977	9520	106	55951	578035	42805	422	834
5	29	1174250	7216	96	69159	126380	649453	859	5890
5	34	1223211	7504	82	76929	21327	1389533	3534	85139
5	39	1143903	5927	93	557277	5117	747635	27193	461911
5	44	1300410	6818	104	558539	3829	247749	125093	1116573
5	49	1175395	8540	74	67402	3053	76215	329648	1271331
5	54	1182103	7064	70	75023	3220	21524	487679	893200
5	59	1233130	6529	81	109244	3317	6034	466172	472026
5	64	1135639	9212	74	112123	6343	1946	330360	208386
5	69	1200881	7804	56	158991	3823	1053	191848	78792
5	74	1154308	6951	72	163273	3342	611	96409	30308
5	79	1163780	7965	72	65732	4644	556	41041	11818
5	84	1073772	7124	44	74200	3409	497	18198	5025
5	89	1040628	6698	91	80397	3420	470	8257	2605
5	94	1074826	6325	64	53268	3437	422	4201	1329
5	99	1177035	6997	86	57038	3259	467	2046	747
5	104	1226613	8433	63	22646	5890	595	1565	736

[a](MR) = medium resolution data acquisition
[b](LR) = low resolution data acquisition
[c]Intensities of all measured elements are adjusted by the addition of In (10 µg/L) as an internal standard.

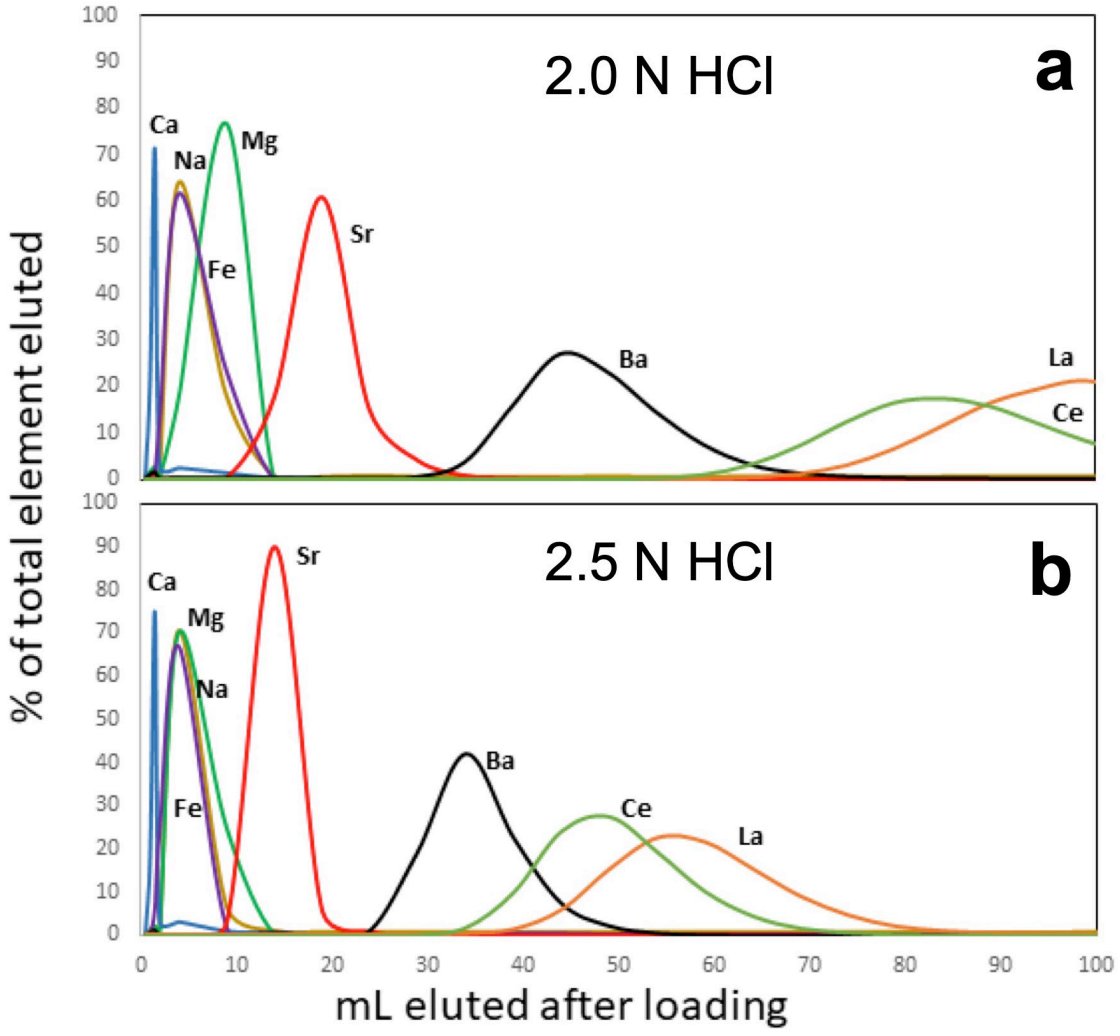

Appendix Figure 1: Examples of column matrix separation for major elements, Ba, and isobaric interferents La and Ce for a volcanic silicate sample using the BIO-RAD Poly-Prep® gravity flow ion exchange columns described in the manuscript. In both cases, the full elution was carried out with a single normality of hydrochloric acid (HCl). Eluting with 2.0 N HCl (a) leads to an effective separation of Ba from both major matrix elements and La and Ce, but requires relatively large volumes of acid. For example, nearly 30 mL of 2.0 N HCl is required to recover the Ba, in a column with a reservoir of only 10 mL. Cerium and La were not fully recovered when using 2.0 N HCl, so their % elution values are estimated. Use of 2.5 N HCl (b) leads to a tighter Ba elution curve and effective removal of matrix elements, but a less effective separation of Ba from La and Ce. Raw data used for these plots are provided in Appendix Tables 1 and 2.

Appendix Table 3: Thermo Element® ICP-MS signal intensities (in counts per second) for a column calibration using 2.5 N HCl for the first 20 mL, and 3.0 N HNO_3 for the remaining elution of a produced water sample with 0.5 µg of La and Ce added. All column cuts were diluted to 15 mL prior to analysis. The data are plotted in modified form in Appendix Figure 2 (top)

mL added to column	Cumulative volume	Acid added	Na23(MR)[a] cps[d]	Mg24(MR) cps	Al27(MR) cps	Si28(MR) cps	S34(MR) cps	K39(HR)[b] cps	Ca46(MR) cps	Fe56(MR) cps	Sr88(LR)[c] cps	Y89(LR) cps	Ba137(LR) cps	La139(LR) cps	Ce140(LR) cps
0.5	0.5	2.5 N HCl	1492043	45945	357877	785913	1850	165388	311	20067	44310	1151	8105	1330	4722
0.5	1	2.5 N HCl	742757	32799	437742	907572	2063	23385	1196	78056	35872	1368	4947	2356	3704
0.5	1.5	2.5 N HCl	767392	87434	461557	980422	3316	50142	357	28563967	43328	1726	9466	2686	3149
0.5	2	2.5 N HCl	13770512	1569543	462240	843766	2266	54457	344	66812001	28528	1530	5685	1397	2669
2	4	2.5 N HCl	18039462798	295885620	374705	762777	2275	708933	315	85008992	32425	1747	10271	1593	3378
4	8	2.5 N HCl	565707847	34066760	453139	836128	2284	102517143	205402	821468	3119922261	253571	25863	3470	6699
4	12	2.5 N HCl	2272217	62679	504953	991926	2488	457974	52380	48840	29337597781	2293405	23161	773896	1232437
4	16	2.5 N HCl	1884345	46761	543271	869805	2510	182274	1322	40682	9435879424	746155	39390	4943	5080
2	18	2.5 N HCl	966444	50935	426542	800985	1749	45632	424	60106	519531445	37794	179017	4534	2944
1	19	2.5 N HCl	1175030	53198	507444	759669	233862	27369	3858	45081	57584124	8109	306351	1609	3249
1	20	2.5 N HCl	1333316	32744	511000	779674	1678	119882	264	24906	37546196	5873	821483	2135	3791
3	23	3.0 N HNO_3	1181782	37651	445704	853311	3360	52326	369	27484	55222856	31038	596356064	222262	67543
3	26	3.0 N HNO_3	2392347	40307	695960	819588	3299	84323	306	38468	1686395	3487	44929506	203934	1384128
1	27	3.0 N HNO_3	1032505	47620	322902	727392	2010	39402	668	14768	86556	1389	100313	269022	1317992
1	28	3.0 N HNO_3	713521	31694	345333	666968	1947	35224	265	9381	68481	1076	34773	513177	1855077
1	29	3.0 N HNO_3	900980	28848	457254	767579	1856	102383	261	68440	52668	842	22673	826053	2135208
1	30	3.0 N HNO_3	1387276	36861	321981	689030	2007	39912	321	30873	49042	813	17216	1232275	2293941
2	32	3.0 N HNO_3	693647	30267	312130	629267	2039	14625	318	16608	48340	667	16694	3500133	3921648
2	34	3.0 N HNO_3	1139737	34266	566392	768164	2335	26796	303	33638	165926	1459	10029	3860203	2416789
6	40	3.0 N HNO_3	6376279	133000	828991	1024284	3161	58544	501	44775	7848544	2402	116114	6334504	1645992

[a](MR) = medium resolution data acquisition
[b](HR) = high resolution data acquisition
[c](LR) = low resolution data acquisition
[d]Intensities of all measured elements are adjusted by the addition of In (10 µg/L) as an internal standard.

Appendix Table 4: Thermo Element® ICP-MS signal intensities (in counts per second) for a column calibration using 2.5 N HCl for the first 20 mL, and 2.0 N HNO_3 for the remaining elution of dissolved freshwater mussel shell calcium carbonate. Approximately 4 µg of Ba and 0.1 µg of La and Ce were added. All column cuts were diluted to 15 mL prior to analysis. The data are plotted in modified form in Appendix Figure 2 (bottom).

mL added to column	Cumulative volume	Acid added	Sr88(LR)[a] cps[b]	Y89(LR) cps	Ba137(LR) cps	La139(LR) cps	Ce140(LR) cps
0.5	0.5	2.5 N HCl	22583	1119	9666	1128	2690
0.5	1	2.5 N HCl	173789	13578	27275	15874	30621
1	2	2.5 N HCl	18429	1203	21445	1582	3902
3	5	2.5 N HCl	33707372	216248	149708	265769	420508
3	8	2.5 N HCl	126533559	475247	17819	2748	5545
3	11	2.5 N HCl	131640311	726303	37059	3126	7625
3	14	2.5 N HCl	61936028	935375	163439	4509	12737
3	17	2.5 N HCl	12827786	924775	678477	8892	25433
3	20	2.5 N HCl	3543712	611454	2153771	15431	47373
2	22	2.0 N HNO_3	967084	167621	6504348	16657	47949
2	24	2.0 N HNO_3	432597	69251	10298462	18604	52097
2	26	2.0 N HNO_3	208285	55374	6137866	20990	68167
2	28	2.0 N HNO_3	82843	24408	1413859	18969	43994
2	30	2.0 N HNO_3	215657	40001	1381888	30727	98209
2	32	2.0 N HNO_3	83876	32250	572540	39631	124554
2	34	2.0 N HNO_3	32373	34802	355294	74117	236415
4	38	2.0 N HNO_3	16677	30004	54131	145403	402060
4	42	2.0 N HNO_3	33023	19679	8051	207276	481636
8	50	2.0 N HNO_3	24583	21694	5562	692876	1077373
8	58	2.0 N HNO_3	27713	10352	6171	911024	849891
2	60	2.0 N HNO_3	17696	2390	4012	231068	149825

[a](LR) = low resolution data acquisition

[b]Intensities of all measured elements are adjusted by the addition of In (10 µg/L) as an internal standard.

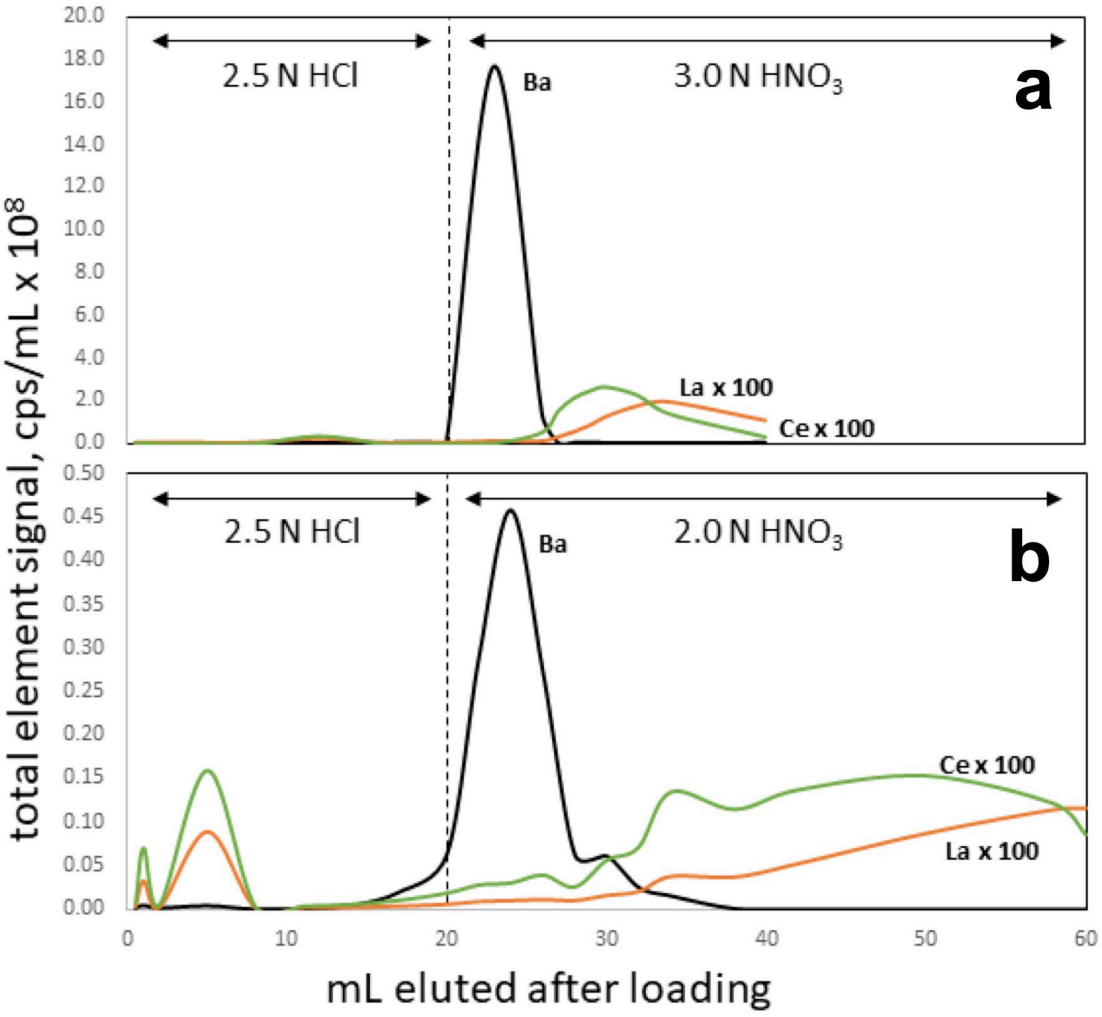

Appendix Figure 2: Examples of column matrix separation of Ba from isobaric interferents La and Ce for a produced water sample (a) and calcium carbonate sample (b) using the BIO-RAD Poly-Prep® gravity flow ion exchange columns described in the manuscript. In both cases, major cations (not shown) were eluted with 2.5 N HCl for the first 20 mL; afterward, either 2.0 N or 3.0 N HNO_3 was used to elute the remaining elements. The y-axis is the signal intensity (in counts per second by SF-ICP-MS) per mL of each column cut, recalculated to reflect the total element signature rather than just the measured isotope. Additional La and Ce was added to both samples prior to putting them through the column to provide enough of these elements to evaluate their separation from Ba. The La and Ce signals are multiplied by the factors shown in order to be clearly distinguishable on this diagram. Raw data used for these plots are provided in Appendix Tables 3 and 4.

Bibliography

An, Y. J.; Li, X.; Zhang, Z. F. Barium Isotopic Compositions in Thirty-Four Geological Reference Materials Analyzed by MC-ICP-MS. *Geostand Geoanalyt Res* **2020,** 44, 183-199.

Andreasen, R.; Sharma, M. Mixing and Homogenization in the Early Solar System: Clues from Sr, Ba, Nd, and Sm Isotopes in Meteorites. *Astrophysics J.* **2007,** 665, 874-883.

Bacon, M. P.; Edmond, J. M. Barium at Geosec III in the Southwest Pacific. *Earth Planet Sci Lett* **1972**, 16, 66-74.

Baird, G. C.; Lash, G. G. Devonian Strata and Environments: Chautauqua County Region: New York State. In *62nd Annual Meeting Guidebook; NY State Geological Association* **1990**, A1-A46.

Barbot, E.; Vidic, N. S.; Gregory, K. B.; Vidic, R. D. Spatial and Temporal Correlation of Water Quality Parameters of Produced Waters from Devonian-Age Shale Following Hydraulic Fracturing. *Environ Sci Technol* **2013**, 47(6), 2562-2569.

Banner, J. L.; Hanson, G. N. Calculation of Simultaneous Isotopic and Trace Element Variations During Water-Rock Interaction with Applications to Carbonate Diagenesis. *Geochim. Cosmochim. Acta.* **1990,** 54(11), 3123-3137.

Barling, J.; Weis, D. Influence of Non-Spectral Matrix Effects on the Accuracy of Pb isotope Ratio Measurement by MC-ICP-MS: Implications for the External Normalization Method of Instrumental Mass Bias Correction. *J. Anal. Atom. Spectrom.* **2008,** 23, 1017.

Bates, S. L.; Hendry, K. R.; Pryer, H. V.; Kinsley, C. W.; Pyle, K. M.; Woodward, E. M. S.; Horner, T. J. Barium Isotopes Reveal Role of Ocean Circulation on Barium Cycling in the Atlantic. *Geochim Cosmochim Acta*. **2017,** 204, 286-299.

Bérhéret, J-G.; Brumsack, H-J. Barite Concretions as Evidence of Pauses in Sedimentation in the Marnes Bleus Formation of the Vocontian Basin (SE France). *Sed. Geol.* **2000,** 130, 205-228.

Bern, C. R.; Birdwell, J. E.; Jubb, A. M. Water-Rock Interaction and the concentrations of Major, Trace, and Rare Earth Elements in Hydrocarbon-Associated Produced Waters of the United States. *Environ. Sci. Processes Impacts.* **2021,** 23, 1198-1219.

Blondes, M. S.; Gans, K. D.; Engle, M. A.; Kharaka, Y. K.; Reidy, M. E.; Saraswathula, V.; Thordsen, J. J.; Rowan, E. L.; Morrissey, E. A. et. al. U.S. Geological Survey National Produced Waters Geochemical Database (ver. 2.3). *U.S. Geological Survey Data Release.* **2018.**

Böttcher, M. E.; Geprägs, P.; Neubert, N.; von Allmen, K.; Pretet, C.; Samankassou, E.; Nägler, T. F. Barium Isotope Fractionation During Experimental Formation of the Double Carbonate $Ba_{mn}[CO_3]_2$ at Ambient Temperature. *Isotopes Env Health Stud* **2012**, 48, 457-463.

Breit, G. N.; Simmons, E. C.; Goldhaber, M. B. Dissolution of Barite for the Analysis of Strontium Isotopes and Other Chemical and Isotopic Variations Using Aqueous Sodium Carbonate. *Chem Geol (Isotope Geosc Sect).* **1985,** 52, 333-336.

Bridgestock, L.; Hsieh, Y-T.; Porcelli, D.; Homoky, W. B.; Bryan, A.; Henderson, G. M. Controls on the Barium Isotope Compositions of Marine Sediments. *Earth Planet Sci Lett*. **2018,** 481, 101-110.

Bullen, T.; Chadwick, O. Ca, Sr and Ba Stable Isotopes Reveal the Fate of Soil Nutrients Along a Tropical Climosequence in Hawaii. *Chem Geol* **2016,** 422, 25-45.

Cao, Z.; Siebert, C.; Hathorne, E. C.; Dai, M.; Frank, M. Constraining the Oceanic Barium Cycle with Stable Barium Isotopes. *Earth Planet Sci Lett* **2016,** 434, 1-9.

Carter, S.C.; Paytan, A.; Griffith, E. M. Toward an Improved Understanding of the Marine Barium Cycle and the Application of Marine Barite as a Paleoproductivity Proxy. *Minerals.* **2020,** 10, 421.

Castellini, D. G.; Dickens, G. R.; Snyder, G. T.; Ruppel, C. D. Barium Cycling in Shallow Sediment Above Active Mud Volcanoes in the Gulf of Mexico. *Chem. Geol.* **2006,** 226, 1-30.

Chan, L. H.; Edmond, J. M.; Stallard, R. F.; Broecker, W. S.; Chung, Y. C.; Weiss, R. F.; Ku, T. L. Radium and Barium at GEOSECS Stations in the Atlantic and Pacific. *Earth Planet Sci. Lett.* **1976,** 32, 258-267.

Chapman, E. C.; Capo, R. C.; Stewart, B. W.; Kirby, C. S.; Hammack, R. W.; Schroeder, K. T.; Edenborn, H. M. Geochemical and Strontium Isotope Characterization of Produced Waters from Marcellus Shale Natural Gas Extraction. *Environ Sci Technol.* **2012,** 46(6), 3545-53.

Chen, H.; Carter, K. E. Characterization of the Chemicals Used in Hydraulic Fracturing Fluids for Wells Located in the Marcellus Shale Play. *J. Environ. Manage.* **2017,** 200, 312-324.

Church, T. M.; Wolgemuth. Marine Barite Saturation. *Earth Planet Sci. Lett*.**1972,** 15, 35-44.

Clark, S. H. B. Formation of Barite Nodules in Dysaerobic and Anaerobic Zones of Stratified Basins. *AAPG Bulletin.* **1987,** 71(5), 1-27.

Clark, S. H. B.; Poole, F. G.; Wang, Z. Comparison of Some Sediment-Hosted, Stratiform Barite Deposits in China, the United States, and India. *Ore Geol. Rev.* **2004,** 24(1-2), 85-101.

Cole, R. B.; Stewart, B. W. (2009) Continental Margin Volcanism at Sites of Spreading Ridge Subduction: Examples from Southern Alaska and Western California. *Tectonophysics* **2009,** 464, 118-136.

Colton, G. W. Geologic Summary of the Appalachian Basin, with Reference to the Subsurface Disposal of Radioactive Waste Solutions. *US Dep. Of the Int. Geological Survey.* **1961,** Report TEI-791.

Crockford, P. W.; Wing, B. A.; Paytan, A.; Hodgskiss, M. S. W.; Mayfield, K. K.; Hayles, J. A.; Middleton, J. E.; Ahm, A-S. C.; Johnston, D. T.; Caxito, F.; Uhlein, G.; Halverson, G. P.; Eickmann, B.; Torres, M.; Horner, T. J. Barium-Isotopic Constraints on the Origin of Post-Marinoan Barites. *Earth Planet. Sci. Lett.* **2019,** 519, 234-244.

De Witt, W. Java Formation of Late Devonian Age in Western and Central New York: Geological Notes. *AAPG Bulletin* **1960**, 44(12), 1933-1936.

Dubinin, A. V.; Uspenskaya, T. Y. Geochemistry and Specific Features of Manganese Ore Formation in Sediments of Oceanic Bioproductive Zones. *Lith. & Min. Resources.* **2006,** 1, 1-14.

Ferrer, I.; Thurman, E. M. Chemical Constituents and Analytical Approaches for Hydraulic Fracturing Waters. *Trends Environ. Anal. Chem.* **2015,** 5, 18-25.

Foster, D. A.; Staubwasser, M.; Henderson, G. M. 226Ra and Ba Concentrations in the Ross Sea Measured with Multicollector ICP Mass Spectrometry. *Mar. Chem***. 2004,** 87, 59-71.

FracFocus. What Is Fracturing Fluid Made Of? **2020** https://www.fracfocus.org/index.php?p=learn/what-is-fracturing-fluid-made-of.

Gaillardet, J.; Viers, J.; Dupré, B. In Drever JI (ed), *Treatise on Geochemistry*, **2005,** 5, 225-272.

Gale, A.; Dalton, C. A.; Langmuir, C. H.; Su. Y.; Schilling, J-G. The Mean Composition of Ocean Ridge Basalts. *Geochem. Geophy. Geosyst*. **2013,** 14, 489-518.

Ganor, J.; Reznik, I. J.; Rosenberg, Y. O Organics in Water-Rock Interactions. *Rev. Min. & Geochem.* **2009,** 70(1), 259-369.

Geyman, B. M.; Ptacek, J. L.; LaVigne, M.; Horner, T. J. Barium in Deep-Sea Bamboo Corals: Phase Associations, Barium Stable Isotopes, & Prospects for Paleoceanography. *Earth Planet. Sci. Lett*. **2019,** 525, 115751.

Gong, Y.; Zeng, Z.; Cheng, W.; Lu, Y.; Zhang, L.; Yu, H.; Huang, F. Barium Isotopic Fractionation During Strong Weathering of Basalt in a Tropical Climate. *Environ. Int.* **2020,** 143, 115990.

Gou, L-F.; Jin, Z.; Galy, A.; Gong, Y-Z.; Nan, X-Y.; Jin, C.; Wang, X-D.; Bouchez, J.; Cai, H-M.; Chen, J-B.; Yu, H-M.; Huang, F. Seasonal Riverine Barium Isotopic Variation in the Middle Yellow River: Sources and Fractionation. *Earth Planet Sci. Lett*. **2020,** 531, 115990

Gregory, D.; Mukherjee, I.; Olson, S. L.; Large, R. R.; Danyushevsky, L. V.; Stepanov, A. S.; et al. The Formation Mechanisms of Sedimentary Pyrite Nodules Determined by Trace Element Sulfur Isotope Microanalysis. *Geochim. Cosmochim. Acta.* **2019,** 259, 53-68.

Griffith, E. M.; Paytan, A. Barite in the Ocean - Occurrence, Geochemistry and Palaeoceanographic Applications. *Sedimentol.* **2012,** 59(6), 1817-1835.

Gromet, L. P.; Dymek, R. F.; Haskin, L. A.; Korotev, R. L. The "North American Shale Composite": Its Compilation, Major and Trace Element Characteristics. *Geochim Cosmochim Acta* **1984,** 48, 2469-2482.

Guichard, F.; Church, T. M.; Treuil, M.; Jaffrezic, H. Rare Earths in Barites: Distribution and Effects on Aqueous Partitioning. *Geochim Cosmochim Acta* **1979,** 43, 983-997.

Haluszczak, L. O.; Rose, A. W.; Kump, L. R. Geochemical Evaluation of Flowback Brine from Marcellus Gas Wells in Pennsylvania, USA. *Appl Geochem* **2013,** 28, 55-61.

Harrison, A. L.; Jew, A. D.; Dustin, M. K.; Thomas, D. L.; Joe-Wong, C. M.; Bargar, J. R.; Johnson, N.; Brown, G. E.; Maher, K. Element Release and Reaction-Induced Porosity Alteration During Shale-Hydraulic Fracturing Fluid Interactions. *Appl. Geochem.* **2017,** 82, 47-62.

Hendry, K. R.; Pyle, K. M.; Butler, G. B.; Cooper, A.; Fransson, A.; Chierici, M.; Leng, M. J.; Meyer, A.; Dodd, P. A. Spatiotemporal Variability of Barium in Arctic Sea-Ice and Seawater. *J. Geophys. Res. Oceans* **2018,** 123, 3507-3522.

Hernandez-Sanchez, M. T.; Mills, R. A.; Planquette, H.; Pancost, R. D.; Hepburn, L.; Salter, I.; FitzGeorge-Balfour, T. Quantifying Export Production in the Southern Ocean: Implications for the Ba_{xs} Proxy. *Paleoceanography* **2011,** 26(4)

Horner, T. J.; Kinsley, C. W.; Nielsen, S. G. Barium-Isotopic Fractionation in Seawater Mediated by Barite Cycling and Oceanic Circulation. *Earth Planet. Sci. Lett.* **2015,** 430, 511-522.

Horner, T. J.; Pryer, H. V.; Nielsen, S. G.; Crockford, P. W.; Gauglitz, J. M.; Wing, B. A.; Ricketts, R. D. Pelagic Barite Precipitation at Micromolar Ambient Sulfate. *Nat. Commun.* **2017,** 8, 1342.

Hsieh, Y-T.; Henderson, G. M. Barium Stable Isotopes in the Global Ocean: Tracer of Ba Inputs and Utilization. *Earth Planet. Sci. Lett.* **2017,** 473, 269-278.

Jew, A. D.; Dustin, M. K.; Harrison, A. L.; Joe-Wong, C. M.; Thomas, D. L.; Maher, K.; Brown, G. E.; Bargar, J. R. Impact of Organics and Carbonates on the Oxidation and Precipitation of Iron During Hydraulic Fracturing of Shale. *Energy & Fuels* **2017**, 31(4), 3643-3658.

Jew, A. D.; Li, Q.; Cercone, D.; Maher, K.; Brown, G. E.; Bargar, J. R. Barium Sources in Hydraulic Fracturing Systems and Chemical Controls on Its Release into Solution. *Unconventional Resources Technology Conference*, **2018;** Conference Paper 2899671.

Jew, A. D.; Li, Q.; Cercone, D.; Gordon E. Brown, J.; Bargar, J. R. A New Approach to Controlling Barite Scaling in Unconventional Systems. *Unconventional Resources Technology Conference, AAPG.* **2019,** Conference Paper URTEC-2019-512-MS.

Johnson, C. A.; Piatak, N. M.; Miller, M. M. Barite (Barium) Chap. D6; *U.S. Geological Survey: U.S. Geological Survey Professional Paper 1802,* **2017,** D1-D18.

Knittel, K.; Boetius, A. Anaerobic Oxidation of Methane: Progress with an Unknown Process. *Annu. Rev. Microbiol.* **2009,** 63, 311-334.

Kravchenko, J.; Darrah, T. H.; Miller, R. K.; Lyerly, H. K.; Vengosh, A. A Review of the Health Impacts of Barium from Natural and Anthropogenic Exposure. *Environ. Geochem. Health* **2014,** 36(4), 797-814.

Landis, J. D.; Sharma, M.; Renock, D.; Niu, D. Rapid Desorption of Radium Isotopes from Black Shale During Hydraulic Fracturing. 1. Source Phases that Control the Release of Ra from Marcellus Shale. *Chem. Geol.* **2018,** 496, 1-13.

Lash, G. G. Authigenic Barite Nodules and Carbonate Concretions in the Upper Devonian Shale Succession of Western New York – A Record of Variable Methane Flux During Burial. *Marine and Petroleum Geology* **2015,** 59, 305-319.

Li, F.; Webb, G. E.; Algeo, T. J.; Kershaw, S.; Lu, C.; Oehlert, A. M.; Gong, Q.; Pourmand, A.; Tan, X. Modern Carbonate Ooids Preserve Ambient Aqueous REE Signatures. *Chem. Geol.* **2019,** 509, 163-177.

Li, Q.; Jew, A. D.; Brown, G. E.; Bargar, J. R.; Maher, K. Reactive Transport Modeling of Shale–Fluid Interactions after Imbibition of Fracturing Fluids. *Energy & Fuels* **2020**, 34(5), 5511-5523.

Lin, Y-B.; Wei, H-Z.; Jiang, S-Y.; Hohl, S.; Lei, H-L.; Liu, X.; Dong, G. Accurate Determination of Barium Isotopic Compositions in Sequentially Leached Phases from Carbonates by Double Spike-Thermal Ionization Mass Spectrometry (DS-TIMS). *Anal. Chem.* **2020,** 92, 2417-2424.

Martínez-Carreño, N; García-Gil, S.; Cartelle, V.; de Blas, E.; Ramírez-Pérez, A. M.; Insua, T. L. Geochemical and Geological Factors Controlling the Spatial Distribution of Sulfate-Methane Transition Zone in the Río de Vigo (NW Spain). *Cont. Shelf Research*. **2017,** 140, 47-59.

Martini, A. M.; Walter, L. M.; Lyons, T. W.; Hover, V. C.; Hansen, J. Significance of Early-Diagenetic Water-Rock Interactions in a Modern Marine Siliciclastic/Evaporite Environment: Salina Ometepec, Baja California. *GSA Bull.* **2002,** 114(9), 1055-1069.

Matecha, R. M.; Capo, R. C.; Stewart, B. W.; Thompson, R. L.; Hakala, J. A. A Single Column Separation Method for Barium Isotope Analysis of Geologic and Hydrologic Materials with Complex Matrices. *Geochem Trans* **2021**, 22(4), 9.

Matecha, R. M.; Xiong, W.; Heck, W. F.; Stewart, B. W.; Capo, R. C.; Hakala, J. A. Experimental Investigation of Barium Sources and Fluid-Rock Interaction in Unconventional Marcellus Shale Wells Using Ba Isotopes. *Energy and Fuels* **2022,** 36(8) 4470-4478.

Mavromatis, V.; van Zuilen, K.; Purgstaller, B.; Baldermann, A.; Nägler, T. F.; Dietzel, M. Barium Isotope Fractionation During Witherite (BaCO3) Dissolution, Precipitation and at Equilibrium. *Geochim. Cosmochim. Acta.* **2016,** 190, 72-84.

McLennan, S. M. Relationship Between the Trace Element Composition of Sedimentary Rocks and Upper Continental Crust. *Geochem. Geophy. Geosyst.* **2001,** 2:2000GC000109.

Merschel, G.; Bau, M. Rare Earth Elements in the Aragonitic Shell of Freshwater Mussel Corbicula Fluminea and the Bioavailability of Anthropogenic Lanthanum, Samarium and Gadolinium in River Water. *Sci. Total Environ.* **2015,** 533, 91-101.

Miyazaki, T.; Kimura, J-I.; Chang, Q. Analysis of Stable Isotope Ratios of Ba by Double-Spike Standard-Sample Bracketing Using Multiple-Collector Inductively Coupled Plasma Mass Spectrometry. *J. Anal. Atom. Spectrom.* **2014,** 29, 483.

Mullins, H. T.; Neumann, A. C.; Wilber, R. J.; Boardman, M. R. Nodular Carbonate Sediment on Bahamian Slopes; Possible Precursors to Nodular Limestones. *J. Sed. Research*, **1980**, 50(1), 117-131.

Nan, X.; Wu, F.; Zhang, Z.; Hou, Z.; Huang, F.; Yu, H. High-Precision Barium Isotope Measurements by MC-ICP-MS. *J. Anal. Atom. Spectrom.* **2015,** 30, 2307-2315.

Nan, X-Y.; Yu, H-M.; Rudnick, R. L.; Gaschnig, R. M.; Xu, J.; Li, W-Y.; Zhang, Q.; Jin, Z-D.; Li, X-H.; Huang, F. Barium Isotopic Composition of the Upper Continental Crust. *Geochim. Cosmochim. Acta.* **2018,** 233, 33-49.

Niu, Y. Bulk-Rock Major and Trace Element Compositions of Abyssal Peridotites: Implications for Mantle Melting, Melt Extraction and Post-Melting Processes Beneath Mid-Ocean Ridges. *J. Petrol.* **2004,** 45, 2423-2458.

Nozaki, Y. A Fresh Look at Element Distribution in the North Pacific Ocean. *Eos.* **1997,** 78, 221-223.

Nuelle, L. M.; Shelton, K. L. Geologic and Geochemical Evidence of Possible Bedded Barite Deposits in Devonian Rocks of the Valley and Ridge Province, Appalachian Mountains. *Economic Geology.* **1986,** 81, 1408-1430.

Ouyang, B.; Akob, D. M.; Dunlap, D.; Renock, D. Microbially Mediated Barite Dissolution in Anoxic Brines. *Appl. Geochem.* **2017,** 76, 51-59.

Over, D. J. Conodont Biostratigraphy of the Java Formation (Upper Devonian) and the Frasnian-Famennian Boundary in Western New York State. *Geological Society of America: Special Paper* **1997,** 321, 161-177.

PADEP. Chemicals Used by Hydraulic Fracturing Companies in Pennsylvania for Surface and Hydraulic Fracturing Activities. Pennsylvania Dep Environ Protection, **2010,** http://files.dep.state.pa.us/OilGas/BOGM/BOGMPortalFiles/MarcellusShale/Frac%20list%206-30-2010.pdf

Paukert Vankeuren, A. N.; Hakala, J. A.; Jarvis, K.; Moore, J. E. Mineral Reactions in Shale Gas Reservoirs: Barite Scale Formation from Reusing Produced Water as Hydraulic Fracturing Fluid. *Environ. Sci. Technol.* **2017,** 51(16), 9391-9402.

Phan, T. T.; Capo, R. C.; Stewart, B. W.; Graney, J. R.; Johnson, J. D.; Sharma, S.; Toro, J. Trace Metal Distribution and Mobility in Drill Cuttings and Produced Waters from Marcellus Shale Gas Extraction: Uranium, Arsenic, Barium. *Appl. Geochem.* **2015,** 60, 89-103.

Phan, T. T., Paukert Vankeuren, A. N.; Hakala, J. A. Role of Water-Rock Interaction in the Geochemical Evolution of Marcellus Shale Produced Waters. *Int. J. Coal Min.* **2018,** 191, 95-111.

Pretet, C.; van Zuilen, K.; Nägler, T. F.; Reynaud, S.; Böttcher, M. E.; Samankassou, E. Constraints on Barium Isotope Fractionation During Aragonite Precipitation by Corals. *Deposit Rec***. 2016,** 1, 118-129.

Raczek, I.; Stoll, B.; Hofmann, A. W.; Jochum, K. P. High-Precision Trace Element Data for the USGS Reference Materials BCR-1, BCR-2, BHVO-1, BHVO-2, AGV-1, AGV-2, DTS-1, DTS-2, GSP-1, and GSP-2 by ID-TIMS and MIC-SSMS. *Geostand Newslett.* **2001,** 25, 77-86.

Rassenfoss, S. From Flowback to Fracturing: Water Recycling Grows in the Marcellus Shale. *J. Petrol. Technol.* **2011,** 63(7), 48-51.

Renock, D.; Landis, J. D.; Sharma, M. Reductive Weathering of Black Shale and Release of Barium During Hydraulic Fracturing. *Appl. Geochem.* **2016**, 65, 73-86.

Roen, J. B. Geology of the Devonian Black Shales of the Appalachian Basin. *Org. Goechem.* **1983,** 5(4), 241-254.

Rowen, E. L.; Engle, M. A.; Kraemer, T. F.; Schroeder, K. T.; Hammack, R. W.; Doughten, M. W. Geochemical and Isotopic Evolution of Water Produced from Middle Devonian Marcellus Shale Gas Wells, Appalachian Basin, Pennsylvania. *AAPG Bull.* **2015,** 99(2), 181-206.

Rudge, J. F.; Reynolds, B. C.; Bourdon, B. The Double Spike Toolbox. *Chem. Geol.* **2009,** 265, 420-431.

Rudnick, R. L.; Gao, S. Composition of the Continental Crust. In *Treaties on Geochemistry, Holland, H. D., Turekian, K. K. , Ed. Elsevier-Pergamon: Oxford, UK*, **2003,** 3, 1-64.

Shikazono, N. Precipitation Mechanisms of Barite in Sulfate-Sulfide Deposits in Back-Arc Basins. *Geochim. Cosmochim. Acta* **1994,** 58, 2203-2213.

Soeder, D. J.; Sharma, S.; Pekney, N.; Hopkinson, L.; Dilmore, R.; Kutchko, B.; Stewart, B.; Carter, K.; Hakala, A.; Capo, R. An Approach for Assessing Engineering Risk from Shale Gas Wells in the United States. *Int. J. Coal Geol.* **2014,** 126, 4-19.

Stewart, B. W.; Chapman, E. C.; Capo, R. C.; Johnson, J. D.; Graney, J. R.; Kirby, C. S.; Schroeder, K. T. Origin of Brines, Salts and Carbonate from Shales of the Marcellus Formation: Evidence from Geochemical and Sr Isotope Study of Sequentially Extracted Fluids. *Appl. Geochem.* **2015,** 60, 78-88.

Stiles, C. A.; Mora, C. I.; Driese, S.G. Pedogenic Iron-Manganese Nodules in Vertisols: A New Proxy for Paleoprecipitation? *Geology.* **2001,** 29(10), 943-946.

Stuckman, M. Y.; Lopano, C. L.; Berry, S. M.; Hakala, J. A. Geochemical Solid Characterization of Drill Cuttings, Core, and Drilling Mud from Marcellus Shale Energy Development. *J. Nat. Gas Sci.* **2019,** 68, 102922.

Tasker, T. L.; Warner, N. R.; Burgos, W. D. Geochemical and Isotope Analysis of Produced Water from the Utica/Point Pleasant Shale, Appalachian Basin. *Environ. Sci. Process. Impacts* **2020,** 22(5), 1224-1232.

Tian, L-L.; Zeng, Z.; Nan, X-Y.; Yu, H-M.; Huang, F. Determining Ba Isotopes of Barite Using the Na_2CO_3 Exchange Reaction and Double-Spike Method by MC-ICP-MS. *J. Anal. Atom. Spectrom.* **2019,** 34, 1459-1467.

Tian, L-L.; Gong, Y-Z.; Wei, W.; Kang, J-T.; Yu, H-M.; Huang, F. Rapid Determination of Ba Isotope Compositions for Barites Using a H_2O-Extraction Method and MC-ICP-MS. *J. Anal. Atom. Spectrom.* **2020,**

Tieman, Z. G.; Stewart, B. W.; Capo, R. W.; Phan, T. T.; Lopano, C. L.; Hakala, J. A. Barium Isotopes Track the Source of Dissolved Solids in Produced Water from the Unconventional Marcellus Shale Gas Play. *Environ. Sci. Technol.* **2020,** 54, 4275-4285.

Tillman, J. E.; Barnes, H. L. Deciphering Fracturing and Fluid Migration Histories in Northern Appalachian Basin. *AAPG Bulletin.* **1983,** 67(4), 692-705.

van Zuilen, K.; Nägler, T. F.; Bullen, T. D. Barium Isotopic Compositions of Geological Reference Materials. *Geostand. Geoanalyt. Res.* **2016,** 40, 543-558.

van Zuilen, K.; Müller, T.; Nägler, T. F.; Dietzel, M.; Küsters, T. Experimental Determination of Barium Isotope Fractionation During Diffusion and Adsorption Processes at Low Temperatures. *Geochim. Cosmochim. Acta.* **2016,** 186, 226-241.

Vetter, O. J. Oilfield Scale---Can We Handle It? *J. Petrol. Technol.* **1976,** 28, 1402-1408.

Vidic, R. D.; Brantley, S. L.; Vandenbossche, J. M.; Yoxtheimer, D.; Abad, J. D. Impact of Shale Gas Development on Regional Water Quality. *Science*. **2013,** 340, 6134.

von Allmen, K.; Böttcher, M. E.; Samankassou, E.; Nägler, T. F. Barium Isotope Fractionation in the Global Barium Cycle: First Evidence from Barium Minerals and Precipitation Experiments. *Chem. Geol.* **2010,** 277(1-2), 70-77.

Wang, K.-S.; Resch, R.; Dunn, K.; Shuler, P.; Tang, Y.; Koel, B. E.; Yen, T. F. Dissolution of the Barite (001) Surface by the Chelating Agent Dtpa as Studied with Non-Contact Atomic Force Microscopy. Colloids Surfaces A *Physiochem. Eng, Aspects* **1999,** 160, 217-227.

Wang, W.; Wu, Z.; Huang, F. Equilibrium Barium Isotope Fractionation Between Minerals and Aqueous Solution from First-Principles Calculations. *Geochim. Cosmochim. Acta.* **2021,** 292, 64-77.

Wasserburg, G. J.; Jacobsen, S. B.; DePaolo, D. J.; McCulloch, M. T.; Wen, T. Precise Determination of Sm/Nd Ratios, Sm and Nd Isotopic Abundances in Standard Solutions. *Geochim. Cosmochim. Acta***. 1981,** 45, 2311-2323.

Xiong, W.; Gill, M.; Moore, J.; Crandall, D.; Hakala, J. A.; Lopano, C. Influence of Reactive Flow Conditions on Barite Scaling in Marcellus Shale During Stimulation and Shut-in Periods of Hydraulic Fracturing. *Energy & Fuels.* **2020,** 34(11), 13625-13635.

Xiong, W.; Lopano, C.; Hakala, A.; Carney, B. Investigation of Barite Scaling During Reaction between Pre-Treated Hydraulic Fracturing Fluid from the Field and Marcellus Shale. *Unconventional Resources Technology Conference, Austin, Texas*, **2020,** Conference Paper URTEC-2020-2734-MS.

Xiong, W.; Deng, H.; Moore, J.; Crandall, D.; Hakala, J. A.; Lopano, C. Influence of Flow Pathway Geometry on Barite Scale Deposition in Marcellus Shale During Hydraulic Fracturing. *Energy & Fuels.* **2021,** 35(15), 11947-11957.

Yu, Y.; Siebert, C.; Fietzke, J.; Goepfert, T.; Hathorne, E.; Cao, Z.; Frank, M. The Impact of MC-ICP-MS Plasma Conditions on the Accuracy and Precision of Stable Isotope Measurements Evaluated for Barium Isotopes. *Chem. Geol.* **2020,** 549, 119697.

Zan, B.; Mou, C.; Lash, G. G.; Yan, J.; Hou, Q. Diagenetic Barite-Calcite-Pyrite Nodules in the Silurian Longmaxi Formation of the Yangtze Block, South China: A Plausible Record of Sulfate-Methane Transition Zone Movements in Ancient Marine Sediments. *Chem. Geol.* **2022,** 595, 120789.

Zeng, Z.; Li, X.; Liu, Y.; Huang, F.; Yu, H. M. High-Precision Barium Isotope Measurements of Carbonates by MC-ICP-MS. *Geostand. Geoanalyt. Res.* **2019,** 43, 291-300.